

Electronic Thesis and Dissertation Repository

5-15-2011 12:00 AM

Assessing and Improving 4D-CT Imaging for Radiotherapy Applications

Greg Pierce, *The University of Western Ontario*

Supervisor: Dr. Ting-Yim Lee, *The University of Western Ontario*

Joint Supervisor: Dr. Jerry Battista, *The University of Western Ontario*

A thesis submitted in partial fulfillment of the requirements for the Doctor of Philosophy degree in Medical Biophysics

© Greg Pierce 2011

Follow this and additional works at: <https://ir.lib.uwo.ca/etd>



Part of the [Medical Biophysics Commons](#)

Recommended Citation

Pierce, Greg, "Assessing and Improving 4D-CT Imaging for Radiotherapy Applications" (2011). *Electronic Thesis and Dissertation Repository*. 197.

<https://ir.lib.uwo.ca/etd/197>

This Dissertation/Thesis is brought to you for free and open access by Scholarship@Western. It has been accepted for inclusion in Electronic Thesis and Dissertation Repository by an authorized administrator of Scholarship@Western. For more information, please contact wlsadmin@uwo.ca.

ASSESSING AND IMPROVING 4D-CT IMAGING FOR RADIOTHERAPY
APPLICATIONS

(Spine title: Assessing and Improving 4D-CT Imaging)

(Thesis format: Integrated Article)

by

Greg Pierce

Graduate Program in Medical Biophysics

A thesis submitted in partial fulfillment
of the requirements for the degree of
Doctor of Philosophy

The School of Graduate and Postdoctoral Studies
The University of Western Ontario
London, Ontario, Canada

© Greg Pierce 2011

THE UNIVERSITY OF WESTERN ONTARIO
School of Graduate and Postdoctoral Studies

CERTIFICATE OF EXAMINATION

Joint-Supervisors

Examiners

Dr. Ting-Yim Lee

Dr. Jeff Chen

Dr. Jerry J. Battista

Dr. Michael Lock

Dr. Eugene Wong

Dr. Kristy Brock

The thesis by

Gregory David Pierce

entitled:

**Assessing and Improving 4D-CT Imaging for Radiotherapy
Applications**

is accepted in partial fulfillment of the
requirements for the degree of
DOCTOR OF PHILOSOPHY

Date

Chair of the Thesis Examination Board

Abstract

Lung cancer has both a high incidence and death rate. A contributing factor to these high rates comes from the difficulty of treating lung cancers due to the inherent mobility of the lung tissue and the tumour. 4D-CT imaging has been developed to image lung tumours as they move during respiration. Most 4D-CT imaging methods rely on data from an external respiratory surrogate to sort the images according to respiratory phase. However, it has been shown that respiratory surrogate 4D-CT methods can suffer from imaging artifacts that degrade the image quality of the 4D-CT volumes that are used to plan a patient's radiation therapy.

In Chapter 2 of this thesis a method to investigate the correlation between an external respiratory surrogate and the internal anatomy was developed. The studies were performed on ventilated pigs with an induced inconsistent amplitude of breathing. The effect of inconsistent breathing on the correlation between the external marker and the internal anatomy was tested using a linear regression. It was found in 10 of the 12 studies performed that there were significant changes in the slope of the regression line as a result of inconsistent breathing. From this study we conclude that the relationship between an external marker and the internal anatomy is not stable and can be perturbed by inconsistent breathing amplitudes.

Chapter 3 describes the development of a image based 4D-CT imaging algorithm based on the concept of normalized cross correlation (NCC) between images. The volumes produced by the image based algorithm were compared to volumes produced

using a clinical external marker 4D-CT algorithm. The image based method produced 4D-CT volumes that had a reduced number of imaging artifacts when compared to the external marker produced volumes. It was shown that an image based 4D-CT method could be developed and perform as well or better than external marker methods that are currently in clinical use.

In Chapter 4 a method was developed to assess the uncertainties of the locations of anatomical structures in the volumes produced by the image based 4D-CT algorithm developed in Chapter 3. The uncertainties introduced by using NCC to match a pair of images according to respiratory phase were modeled and experimentally determined. Additionally, the assumption that two subvolumes could be matched in respiratory phase using a single pair of 2D overlapping images was experimentally validated. It was shown that when the image based 4D-CT algorithm developed in Chapter 3 was applied to data acquired from a ventilated pig with induced inconsistent breathing the displacement uncertainties were on the order of 1.0 millimeter.

The results of this thesis show that there exists the possibility of a miscorrelation between the motion of a respiratory surrogate (marker) and the internal anatomy under inconsistent breathing amplitude. Additionally, it was shown that an image based 4D-CT method that operates without the need of one or more external respiratory surrogate(s) could produce artifact free volumes synchronous with respiratory phase. The spatial uncertainties of the volumes produced by the image based 4D-CT method were quantified and shown to be small ($\sim 1\text{mm}$) which is an acceptable accuracy for radiation treatment planning. The elimination of the external respiratory surrogates simplifies the implementation and increases the throughput of the image based 4D-CT method as well.

Keywords

4D-CT, computed tomography, gated radiotherapy, respiratory surrogate, normalized cross correlation, inconsistent breathing amplitude, error analysis

Co-Authorship

The following thesis contains material from manuscripts previously published in *Physics in Medicine and Biology* and *Medical Physics*. The copyright agreement from these two journals are provided in Appendices B & C.

Chapter 2 has been published as an article entitled "The effect of an inconsistent breathing amplitude on the relationship between an external marker and internal lung deformation in a porcine model," in *Medical Physics* vol. 37 (11): pp. 5951-5960 (2010) by Pierce G, Wang K, Gaede S, Battista J and Lee TY. Kevin Wang developed and optimized the nonlinear registration code used in this experiment. Stewart Gaede and Jerry Battista provided advice about the design of the experiments and interpretation of the results. I collected the data, designed the main experiments, wrote the computer code to produce and analyze the results, interpreted the results and wrote the manuscript under the supervision of Ting-Yim Lee.

Chapter 3 has been published as an article entitled "A fully automated non-external marker 4D-CT sorting algorithm using a serial cine scanning protocol," in *Physics in Medicine and Biology* by Carnes G, Gaede S, Yu E, Van Dyk J, Battista J, Lee TY. Edward Yu provided patient recruitment. Stewart Gaede aided in data collection and interpretation of the results. Jake Van Dyk and Jerry Battista provided advice about the algorithm. I aided in the collection of the patient data, conceived and wrote the algorithms to produce and analyze the results and wrote the manuscript under the supervision of Ting-Yim Lee.

Chapter 4 has been submitted to *Physics in Medicine and Biology* as an article entitled "Applying an animal model to quantify the uncertainties of an image based 4D-CT algorithm," by Pierce G, Wang K, Battista J, and Lee TY. Kevin Wang wrote and optimized the nonlinear registration code used in this study. Jerry Battista provided insight into the interpretation of the results. I designed the experiments and wrote the code required to produce and analyze the results, interpreted the final results and wrote the manuscript under the supervision of Ting-Yim Lee.

Epigraph

"No man should escape our universities without knowing how little he knows"

- J. Robert Oppenheimer

"Evil is whatever distracts"

-Franz Kafka

Dedication

*To my wife Martha, who often questioned when ...
but never questioned why.*

Acknowledgments

I first want to acknowledge the help, support and guidance of my supervisors, Dr. Ting-Yim Lee and Dr. Jerry Battista. Dr. Lee was a constant source of knowledge and inspiration. His unbridled work ethic and passion for science set a level to which I will constantly strive to attain throughout my career. Dr. Battista also shared with me a passion for science and taught me that everything that you know, learn and understand needs to be communicated to world. It is only through this communication that scientific discoveries are realized. I could not have had two better mentors during my PhD.

Science is a collaborative field and the work presented in this thesis is no exception. I need to acknowledge Dr. Stewart Gaede for being the originator of this project and for his insight and help during my continuation of the project. Dr. Kevin Wang developed the deformable registration code used in this thesis and was invaluable to my understanding the uses and limitation of his program. Jennifer Hadway provided countless hours and experience during our animal experiments. This work could not have been done without her. Throughout the years I was able to work with a number of students and scientists in the UWO Medical Biophysics program who have helped me in immeasurable ways. I thank all of them as a group, to ensure that not one is left out.

Finally, I need to acknowledge my family and friends. I was fortunate to be involved in a number of extracurricular activities during my degree. While these times were not always the most directly productive towards my PhD work, they provided many enjoyable experiences to continually realize why I was doing the work I was doing and to

appreciate life and everything it has to offer. Special mention goes to Mick Hassell and the UWO Ultimate Frisbee team for reminding me to always make time to play. Additionally, I need to extend a thanks that cannot be summed up with mere words to Dr. Barbara Decker-Pierce and Dr. Blair Pierce for taking me in as a son and being completely and utterly supportive in everything I have done. They have been teachers, parents and friends to me for which I am eternally grateful. I want to thank my mother Pat, for always believing in my abilities. Yes mom, I finally am done school!

Last and most important, I thank my wife Martha. Without her love and support I could not have made it through this degree. She makes me a better person and teaches me something new every day.

Table of Contents

CERTIFICATE OF EXAMINATION	ii
Abstract.....	iii
Co-Authorship.....	vi
Epigraph.....	vii
Dedication.....	viii
Acknowledgments.....	ix
Table of Contents.....	xi
List of Tables	xvi
List of Figures.....	xvii
List of Abbreviations	xix
List of Abbreviations	xix
Chapter 1 INTRODUCTION.....	1
1.1 Lung Cancer.....	1
1.2 Treatments.....	3
1.2.1 Surgery.....	3
1.2.2 Chemotherapy.....	3
1.2.3 Radiation Therapy.....	4
1.3 Respiratory Motion Effects.....	7
1.3.1 The Mechanics of Breathing.....	7
1.3.2 The Motion of a Tumour within the Lung.....	9
1.3.3 CT Imaging of a Moving Lung Tumour	11
1.3.4 Treatment Planning and Delivery Issues	14

1.4	Motion Compensation Methods.....	15
1.4.1	Slow Rotation CT Scanning.....	15
1.4.2	Breath-Hold CT Scanning.....	16
1.4.3	Four-Dimensional (4D) CT Scanning.....	17
1.4.4	Treatment Planning and Delivery with 4D-CT.....	20
1.5	Limitations of Current 4D-CT Imaging and Treatment Methods.....	23
1.5.1	4D-CT Artifacts	23
1.5.2	Respiratory Surrogate Correlation Issues	25
1.5.3	Improvements to 4D-CT Methods	26
1.6	Image Similarity Metrics for Matching Respiratory States	28
1.7	Research Objectives.....	30
1.8	Thesis Outline	30
1.8.1	The relationship between an external marker and the internal lung displacement in a porcine model (Chapter 2).	30
1.8.2	The development of an automated image based 4D-CT sorting algorithm (Chapter 3).....	31
1.8.3	Applying an animal model to quantify the uncertainties of an image based 4D-CT algorithm (Chapter 4)	31
1.8.4	Conclusions (Chapter 5)	32
1.9	References.....	33
Chapter 2	The relationship between an external marker and the internal anatomic lung displacement in a porcine model.....	41
2.1	Introduction.....	41
2.2	Methods.....	43
2.2.1	Image Acquisition.....	43
2.2.2	Categorization of Breathing Patterns	44
2.2.3	Choosing a Reference Scan (RS).....	46

2.2.4	4D-CT Sorting Algorithm.....	47
2.2.5	Subsampling of Ciné Scans	48
2.2.6	Nonlinear Registration Algorithm	48
2.2.7	Experiments and Analysis.....	51
2.3	Results.....	54
2.3.1	RPM Prediction Accuracy Experiment.....	55
2.3.2	Linear Correlation Experiment	56
2.4	Discussion.....	60
2.5	References.....	64
Chapter 3	The development of an automated image based 4D-CT sorting algorithm	68
3.1	Introduction.....	68
3.2	Methods.....	70
3.2.1	Image Data Acquisition	71
3.2.2	4D-CT Methods	74
3.2.3	Comparison and Analysis	87
3.3	Results.....	89
3.4	Discussion.....	94
3.5	References.....	100
Chapter 4	Applying an animal model to quantify the uncertainties of an image based 4D-CT algorithm.....	103
4.1	Introduction.....	103
4.2	Methods.....	105
4.2.1	4D-CT Algorithm and Associated Errors	105
4.2.2	Scanning Protocol	110
4.2.3	Nonlinear Registration Algorithm	111
4.2.4	Uncertainty Analysis Experiments	112

4.3 Results.....	117
4.3.1 Uncertainty due to NCC Matching.....	117
4.3.2 Reference Image Invariance Assumption.....	119
4.4 Discussion.....	122
4.5 References.....	128
Chapter 5 Conclusion.....	130
5.1 Summary.....	130
5.2 The relationship between external marker and internal anatomic lung displacement in a porcine model.....	131
5.3 The development of an automated image based 4D-CT sorting algorithm.....	131
5.4 Applying an animal model to quantify the uncertainties of an image based 4D-CT algorithm.....	134
5.5 Clinical Relevance.....	135
5.5.1 Relevance of a Porcine Model for Testing Lung Motions.....	135
5.5.2 Clinical Relevance of Image Based 4D-CT method.....	135
5.5.3 Limitations of the Image Based 4D-CT Algorithm.....	136
5.6 Future Considerations.....	137
5.7 Future Work.....	139
5.7.1 4D-CT Algorithm for Treatment Planning.....	139
5.7.2 Dose Reduction in 4D-CT.....	142
5.7.3 Vendor-Supplied 4D-CT Comparison.....	143
5.7.4 Programmable Ventilator for Pig Model.....	144
5.7.5 Improved Image Matching Algorithm.....	144
5.8 Conclusions.....	146
5.9 References.....	148
Appendix A Uncertainty Analysis of NCC Formula for CT images.....	150

Appendix B Transfer of Copywrite from <i>Physics in Medicine and Biology</i>	155
Appendix C Transfer of Copywrite from <i>Medical Physics</i>	156
Appendix D Animal Ethics Approval.....	157
Appendix E Human Ethics Approval	158
Curriculum Vitae	160

List of Tables

Table 1-1: Lung cancer staging.....	2
Table 1-2: Summary of tumour motion studies	10
Table 2-1: Results of nonlinear registration analysis.....	54
Table 2-2: Summary of deformation binning results	56
Table 2-3: Results of the linear correlation experiment.....	57
Table 2-4: Summary of Pearson correlation coefficients	58
Table 4-1: Results of fitting the NCC uncertainty equation.	119
Table 4-2: Results from the reference image invariance experiment	122

List of Figures

Figure 1-1: Additive dose in radiotherapy	5
Figure 1-2: Definitions of treatment volumes for radiation therapy.....	6
Figure 1-3: Diagram illustrating the anatomy and functionality of breathing	8
Figure 1-4: Pressure/Volume curve for the lungs	9
Figure 1-5: Geometry of a CT scanner	12
Figure 1-6: Relative motion of x-ray tube to the the patient during helical scanning	12
Figure 1-7: Example of inter-scan artifacts	14
Figure 1-8: Definition of 4D-CT derived treatment margins.....	21
Figure 1-9: Classification of 4D-CT artifacts	24
Figure 2-1: Histogram of patient RPM curve plotted with the a cumulative histogram...	45
Figure 2-2: Categorization of patient breathing cycles.....	46
Figure 2-3: Example of respiratory sorting bins	47
Figure 2-4: Nonlinear registration example.....	51
Figure 2-5: Location of ROIs on axial image of a pig.....	52
Figure 2-6: Results of the linear regression between the RPM motion and the internal motion of the pig.....	59

Figure 3-1: Definition of the image parameters used for image based 4D-CT sorting	73
Figure 3-2: Chest height derived respiratory cycle curve.....	77
Figure 3-3: Determination of breathing cycle length using NCC.....	78
Figure 3-4: Breathing cycle curve truncated to one period.....	79
Figure 3-5: Example of the chest height determined from an axial CT image.....	80
Figure 3-6: Flow chart outlining the image based 4D-CT algorithm	86
Figure 3-7: Patient RPM curve with an irregular breathing section	89
Figure 3-8: Expanded irregular breathing section from figure 3-7.....	90
Figure 3-9: Coronal image from the 4D-CT method comparison	91
Figure 3-10: Results from the figure of merit analysis.....	92
Figure 3-11: RPM frequency histogram: amplitude sorting vs. NCC	93
Figure 3-12: RPM frequency histogram: phase angle sorting vs. NCC	94
Figure 4-1: A diagram describing the 4D-CT scanning protocol	106
Figure 4-2: Illustration of NCC matching uncertainty experiment.....	113
Figure 4-3: Location of ROIs on an axial image of a pig.....	114
Figure 4-4: Illustration of the reference image invariance assumption experiment	116
Figure 4-5: Plot of the NCC uncertainty versus number of NCC image matches.....	118
Figure 4-6: Plot of $\sigma_B(10,B)$ and $\sigma_B(54,B)$ for the left lung ROI.....	120
Figure 4-7: Plot of $\Delta\sigma_B(10,B)$ and $\Delta\sigma_B(54,B)$ for the left lung ROI	121

List of Abbreviations

4D-CT	Four Dimensional Computed Tomography
AFOV	Axial Field of View
Amp	Amplitude Value of RPM Curve
ASIR	Adaptive Statistical Iterative Reconstruction
b	Phase Bin Index Value
c	Nonlinear Registration Constant
CAS	Consistent Amplitude Scan
CAS ₁₂	Subsampled Consistent Amplitude Scan
CC	Cranial-Caudal
CCD	Charged Coupled Device
CH	Chest Height
CT	Computed Tomography
CTV	Clinical Target Volume
CW	Chest Wall
d	Length of Nonlinear Registration Vector
d _{max}	Maximum Allowed Length for Registration Vector
DV	Dorsal-Ventral
Fluoro	Fluoroscopy

GEE	Generalized Estimating Equation
Gy	Gray
HU	Hounsfield Unit
IAS	Inconsistent Amplitude Scan
IAS ₁₂	Subsampled Inconsistent Amplitude Scan
ITV	Internal Target Volume
K	Total Number of Pixels in a 2D Image
LL	Left Lung
m	4D-CT Phase Index Value
M	Total Number of 3D Volumes in a 4D-CT Set
MIP	Maximum Intensity Projection
ML	Medial-Lateral
n	Scan Position Index Value
N	Total Number of Scan Positions
NCC	Normalized Cross Correlation
n _R	Scan Position Index of the Reference Scan
NSCLC	Non Small Cell Lung Cancer
PhA	Phase Angle of RPM Curve
PTV	Planning Target Volume
$ r $	Length of the Nonlinear Resulting Registration Vectors

RL	Right Lung
RMSD	Root Mean Square Deviation
ROI	Region of Interest
RPM	Realtime Position Management
RPM_{ref}	RPM Curve minus RPM Value of the Reference Image
RS	Reference Scan
RS_{12}	Subsampled Reference Scan
s	Image Index Value
S	Total Number of Images in a Scan
SCLC	Small Cell Lung Cancer
SI	Superior-Inferior
σ_0	Minimum Measurable Displacement Uncertainty
σ_{NCC}	Displacement Uncertainty due to a NCC Matching
$\sigma_{total}(n)$	Total Displacement Uncertainty
t	Ciné Time Series Time Index Value
T	Total Number of Images in a Ciné Time of Images
T_{BC}	Number of Images in 1 Breathing Cycle
$\tau(m, n)$	Matrix of Time Index Values of Sorted 4D-CT Scan
TTL	Transistor Transistor Logic

US	Ultrasound
w_1, w_2	Weighting Factors for Linearly Interpreted Image
$\bar{x}, \bar{y}, \bar{z}$	Orthogonal Vector from Nonlinear Registration

Chapter 1

INTRODUCTION

1.1 Lung Cancer

With an estimated 23,200 new cases diagnosed in 2010, lung cancer is the 3rd most diagnosed cancer in Canada, following prostate and breast cancer. Lung cancer is the most potent killer amongst all types of cancers with an estimated 20,600 deaths due to the disease in 2010, which is greater than the total of the next three most prevalent cancer types combined. The overall 5 year survival rate for lung cancer is low, at 15%.¹ Cancers of the lung are grouped into two main categories based on the cell type: small cell lung cancer (SCLC), which makes up 25% of the lung cancer cases, and non-small cell lung cancer (NSCLC), which accounts for the other 75% and constitutes a variety of cell types. Once lung cancer has been diagnosed, the cancer is staged according to the size of the tumour and the degree of spread of the disease. NSCLC is divided into 7 stages that are described using the TNM system, denoting tumour, node and metastasis (table 1-1). The size of tumour and spread of disease increases with stage and 5 year survival rate decreases with stage. SCLCs are faster growing than NSCLCs and are divided into only two stages, limited (30% of patients) and extensive (70% of patients). Depending on the type and stage of tumour at time of diagnosis a physician will prescribe one or a combination of surgery, chemotherapy and radiation therapy.² The treatment types are described in the next section.

Table 1-1: Lung cancer staging. Table adapted from *Falk et al.*²

Stage	TNM	5 Year Survival
IA	T1N0M0	75%
IB	T2N0M0	55%
IIA	T1N1M0	40%
IIB	T2N1M0 or T3N0M0	40%
IIIA	T1-2N2M0 or T3N1-2M0	10-35%
IIIB	T4 any N M0 or any T N3M0	5%
IV	Any T any N M1	< 5%

T denotes Tumour Size

- 1: Tumour less than 3cm in greatest direction, surrounded by lung and without invasion into main bronchus
- 2: Tumour with any of: more than 3cm in any direction; invasion into main bronchus, more than 2cm from carina; or obstructive pneumonitis, but not involving the entire lung
- 3: Tumour with any of: invasion into the chest wall, diaphragm, mediastinal pleura or parietal pericardium; invasion into main bronchus within 2cm of carina, but not invading it; or obstructive pneumonitis of the entire lung
- 4: Tumour with any of: invasion into mediastinum, heart, large vessels, trachea, oesophagus, vertebra, or carina; Separate tumour nodules in the same lobe; or malignant pleural effusion

N denotes extent of regional Lymph Node spread

- 0: No spread
1-3: Increasing spread to nodes

M denotes distant Metastases

- 0: No metastatic disease
1: Distant metastases found
(including pleural or pericardial effusion)

1.2 Treatments

1.2.1 Surgery

Surgery is considered the best curative option for patients presenting with locally contained NSCLC (stages IA - IIIA). Surgeons will remove a portion (wedge resection, lobectomy) or the entirety (pneumonectomy) of the lung to ensure removal of the whole tumour. While the physical removal of the tumour is ideal there are a limited number of lung cancer patients suitable for this highly invasive procedure. The decision to operate is made on the basis of tumour size, position of the tumour within the lung, extent of tumour progression and general health of the patient. A large portion of patients presenting with lung cancer are often life-long smokers with a variety of health issues. As a consequence the number of patients that are eligible surgical candidates is only 10% of those diagnosed with NSCLC. The outcome of these patients ranges from a 75% five-year survival rate for stage IA tumours to a 10% five-year survival for stage IIIA tumours. Patients with SCLC are rarely surgical candidates owing to the rate at which the disease grows and spreads. Less than 1% of patients with limited disease will receive an operation followed by chemotherapy, with a 5 year survival of approximately 50%.²

1.2.2 Chemotherapy

Chemotherapy is the administration of drugs, usually through injection into the blood stream, which act systemically throughout the body to kill cancerous cells. The use of these drugs plays an important role in the overall treatment of lung cancer. Chemotherapy is used in conjunction with both surgery and radiotherapy to treat NSCLC.

Drugs may be given before (neo-adjuvant) or after (adjuvant) surgery or radiotherapy. Neo-adjuvant therapies can be used to downstage the NSCLC tumour by slowing or reversing its growth, allowing for the patient to then receive surgery with radiotherapy. In contrast, the primary treatment for SCLC is chemotherapy. Approximately 80% of patients with limited disease and 60% of patients with extensive disease will respond to the treatment. Due to the systemic nature of this therapy, severe side effects may occur during treatment. Adjuvant radiotherapy may be given to the patient's chest or head to limit the chance of reoccurrence or metastasis (transference of disease to another site). The prognosis of SCLC is quite grim with an average survival with chemotherapy treatment of 18 and 9 months for limited and extensive diseases, respectively. The overall 5-year survival rate for SCLC is only 10%.²

1.2.3 Radiation Therapy

Radiation therapy attempts to kill tumour cells by targeting high energy x-ray radiation at the tumour within the patient's body. As the radiation passes through tissue, it deposits energy, referred to as dose, along its path. By using multiple radiation beams from several directions around the body a superposition of dose can be created at the target volume where the tumour resides, while keeping the dose to other parts of the body low (figure 1-1). Keeping the dose to the healthy structures within the body low is important in order to prevent unwanted side effects from the radiation treatment. The total dose prescribed to the patient is given in a series of fractions delivered 5 days a week for up to 6 weeks. Modern radiotherapy uses 3 or 4 dimensional computed tomography (CT) images of the patient's body to locate and target the tumour. The

tumour is outlined on the patient's CT image by a physician (the GTV or gross tumour volume). Margins are added to the GTV to account for microscopic spread of the disease that cannot be visualized on the CT scan (yielding the CTV or clinical target volume). An additional margin is added to account for the geometric uncertainty in depositing the prescribed dose (the PTV or planning target volume) due to setup errors and movement. A composite of all the different target volumes is shown in figure 1-2.^{3,4}

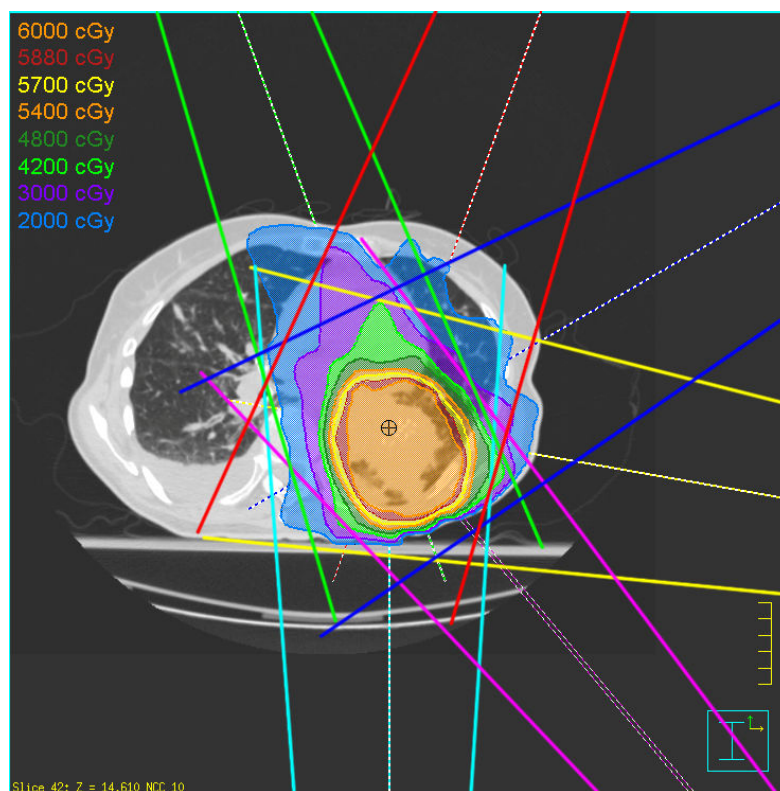


Figure 1-1: Dose addition from multiple radiation beam in radiotherapy. The individual radiation beams are shown as coloured lines. Isodose lines are indicated at the centre of the beams' intersection.

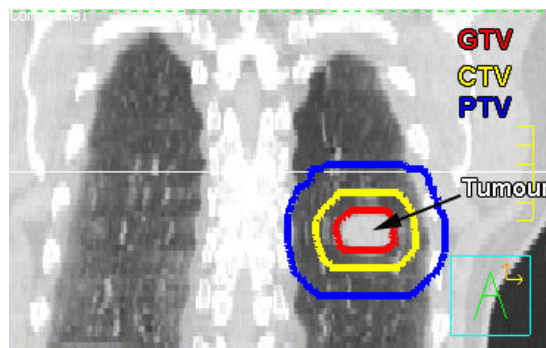


Figure 1-2: Definitions of treatment volumes for radiation therapy

Approximately one half of patients presenting with lung cancer will receive radiation therapy as part of their treatment. Radiotherapy is provided as the primary method of treatment for inoperable stage IA to IIB tumours and bulky stage IIIA & IIIB NSCLCs tumours contained within the thorax that are treated with intent to cure. The administration of radiation is known to relieve a number of respiratory symptoms associated with lung cancer and therefore it is also given as palliative care for terminally ill patients. High radiation doses are delivered to the entire PTV to ensure that the entire tumour (GTV) receives the prescribed dose of radiation. This method of treatment may result in undesired high doses of radiation deposited in adjacent healthy tissue to the tumour. The radiation dose deposited to the adjacent tissue is known to cause adverse side effects that include esophagitis, pneumonitis or damage to the ribs and/or spinal cord. As such, radiation dose levels prescribed to lung tumours during conventional radiation therapy are kept comparatively low (between 60-66 Gy) due to the concern of normal tissue complications. The 4 year survival rate for patients receiving radiation treatments at this dose level is 21%, with a medial survival of 17 months.⁵

Work by *Martel et al.*⁶ has predicted that an increase in dose to the tumour is required if an increase in local control of the tumour, and thus patient survival, is to be achieved. Higher radiation doses for lung cancer treatment should be achievable as it has been shown that normal tissue complications, such as radiation pneumonitis, do not correlate with the local dose prescribed to the tumour. Instead, these adverse events are correlated with factors such as mean dose to the entire healthy lung (lung volume minus the PTV) and the volume of lung receiving dose over 20 Gy (V_{20}).^{7, 8} Current dose escalation studies have confirmed that an increase in survival is correlated with an increase in dose delivered to the tumour.^{9, 10} Therefore, it is imperative that uncertainties in target delineation (GTV, CTV) and target localization (PTV) be reduced to as low a value as possible to allow for the highest doses possible to be prescribed and delivered to the PTV. The next section reviews the complications that a moving target, such as a lung tumour, poses to the radiotherapy process.

1.3 Respiratory Motion Effects

1.3.1 The Mechanics of Breathing

The lungs reside within the thoracic cavity and are surrounded by a liquid filled intra-pleural space. During quiet breathing, the volume of the lungs is increased through the action of two sets of muscles, the diaphragm and the inter-costal muscles. The diaphragm is the most important muscle during respiration. It contracts and pulls the inferior portion of the lungs down and forward and moves approximately 1 cm during quiet respiration. The inter-costal muscles, which are attached to the rib cage, aid during the inhalation phase of breathing. When these muscles contract they pull the ribs

superiorly and laterally, increasing the volume of the thoracic cavity. As the thoracic cavity expands it pulls the pleural membrane outwards creating a negative pressure in the pleural cavity. This negative pressure then pulls the lung outward. This resultant increase in lung volume decreases the air pressure in the lungs and draws air, at atmospheric pressure, into the lungs. Exhalation is a passive process caused by the elastic properties of the lungs returning them to their equilibrium position and in the process expelling the excess air accumulated during inhalation. (figure 1-3) Alveolar pressure is decreased during inspiration and increased during expiration relative to atmospheric pressure. The intra-pleural pressure is always negative with respect to atmospheric pressure. During inhalation, the intra-pleural pressure becomes more negative, causing the lungs to expand, and then returns to its original value during exhalation. The trans-pulmonary pressure is the difference between alveolar pressure in the lungs and intra-pleural pressure. The elasticity of the lungs leads to a unique relationship between the volume of air in the lungs and the trans-pulmonary pressure. The volume of air within the lungs is greater during expiration than inspiration for a given trans-pulmonary pressure (figure 1-4). This phenomena is known as hysteresis.¹¹

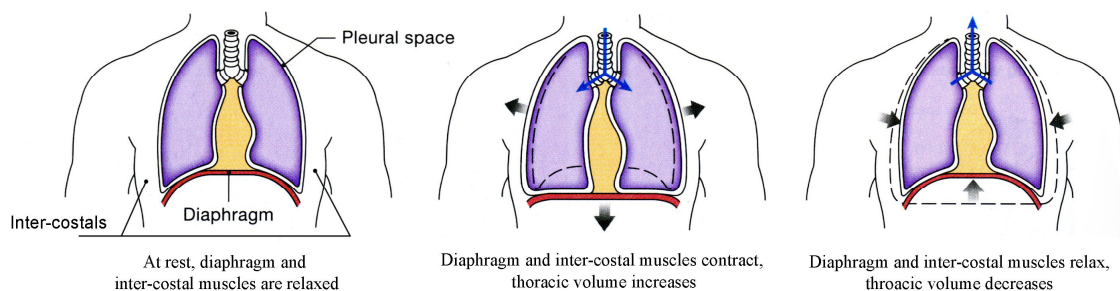


Figure 1-3: Diagram illustrating the anatomy and functionality of breathing.

Adapted from *Silverthorn*.¹²

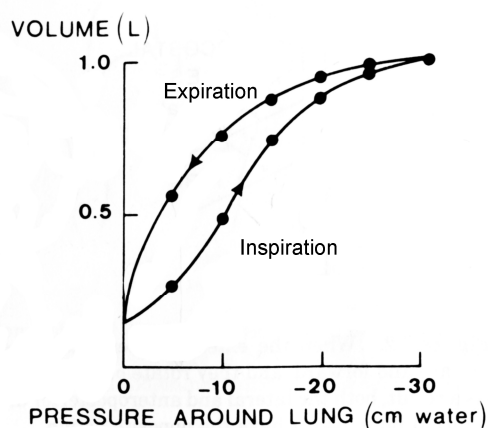


Figure 1-4: Pressure/Volume curve for the lungs.

Adapted from *Silverthorn*.¹²

1.3.2 The Motion of a Tumour within the Lung

A tumour that resides within the lung tissue will be set into motion as a result of respiration. Fluoroscopic imaging is the most common imaging modality used to examine the respiratory induced motion of the tumour. Tumour motion is observed directly or inferred from measurements of the motion of a lung tumour surrogate (e.g. diaphragm).¹³⁻²⁰ The consensus of these studies that have observed the motion of lung tumours is that the dominate component of the tumour motion is in the cranial-caudal (superior-inferior) direction, which is also the dominant component of the diaphragmatic motion. Despite general trends, a vast spectrum of 3-dimensional motions between individual patients and groups of patients have been found (table 1-2). *Seppenwoolde et al.*¹⁸ has published the most extensive studies on lung tumour motion. In their study, gold markers were implanted in or near the tumour and tracked with fluoroscopy over multiple

breathing cycles. From a study of 21 patients it was found that the average amplitude of motion was greatest in the superior-inferior direction (12 ± 2 mm), with much smaller displacements in the medial and dorsal directions (2 ± 1 mm). The most interesting finding of this study was a hysteresis effect between the inspiration path and expiration path of the tumour in 10 of the 21 patients. The hysteresis resulted in up to a 5 mm displacement between the inhalation and exhalation motion trajectories of the gold markers. Additionally, they reported that tumours situated near the heart may have a significant component of motion from the cardiac motion. Overall, the motion of lung tumour is extremely complex and highly patient dependent with the most common feature being a large motion in the superior-inferior direction.

Table 1-2: Summary of tumour motion studies. Adapted from *Keall et al.*²¹

Investigator	Site of Measurement	Direction of Movement	Average Extent of Movement	Minimum	Maximum	Modality
			Value \pm SD (mm)			
<i>Davies et al.</i> ¹⁵	Diaphragm	CC	12 ± 7	7	28	US
<i>Kubo et al.</i> ¹⁷	Diaphragm	CC			20	Fluoro
<i>Mageras et al.</i> ¹⁸	Diaphragm	CC	14	7	21	Fluoro
<i>Ekberg et al.</i> ¹⁶	Tumour	ML	2.4 ± 1.4		5.0	Fluoro
		DV	2.4 ± 1.3		5.0	
		CC	3.9 ± 2.6		12.0	
<i>Barnes et al.</i> ¹⁴	Tumour	CC	12.9 ± 9.5	2.0	31.9	Fluoro
<i>Sixel et al.</i> ²⁰ *	Tumour	ML	1.2 ± 0.9	0.0	3.2	Fluoro
		DV	2.4 ± 1.6	0.0	4.4	
		CC	6.0 ± 3.8	0.0	12.8	
<i>Seppenwoolde et al.</i> ¹⁹	Gold Marker	ML	1.4 ± 1.1	0.2	2.8	Fluoro
		DV	2.2 ± 1.9	0.6	8.2	
		CC	5.5 ± 6.0	0.2	24.6	
<i>Stevens et al.</i> ²¹ #	Tumour	CC	4.5 ± 5.0	0.0	22.0	Radiograph
		CC (moving)	8.3 ± 2.7	3.0	22.0	

* means estimated from individual values of bar graphs
SI moving includes only the patients exhibiting tumour motion in the SI direction
ML: Medio-lateral; DV: Dorso-ventral; CC: Cranio-caudal (superior-inferior); US: Ultrasound; Fluoro: Fluoroscopy

1.3.3 CT Imaging of a Moving Lung Tumour

Computed Tomography (CT) is a high contrast imaging modality that uses x-ray radiation to measure the distribution of linear attenuation coefficients of an object and display them as 2D images. Modern CT scanners have an x-ray detector array and x-ray source mounted on a gantry that rotates around a patient in order to collect x-ray projections from a full 360° around the patient (figure 1-5). A set of 2D axial slice images of the patient are generated by back-projecting the x-ray transmission projections collected through the specified anatomical slice. Gantry rotation periods can range from 1.0 second to 0.4 seconds; however scanners are often capable of rotating at slower speeds, if such a scan mode is desired. The axial field of view (AFOV) dictates the axial length of the patient that can be imaged simultaneously with a single gantry rotation and ranges from 4.0 cm to 16.0 cm. The x-ray detector consists of multiple detector rows in the axial direction allowing multiple slices to be reconstructed within the AFOV. Two separate methods are available to scan large objects. Helical (spiral) CT scanning acquires projection data while the patient is moved through the AFOV. Projections acquired from separate detector rows, but from the same physical location of the patient, are used to reconstruct the individual images (figure 1-6). Serial or Sequential CT acquires projections from a stationary scan position and then translates the patient to the next adjacent position before another scan is taken. This is repeated until the entire volume has been scanned. Images from separate scan positions are concatenated to produce 3D volumes.²²

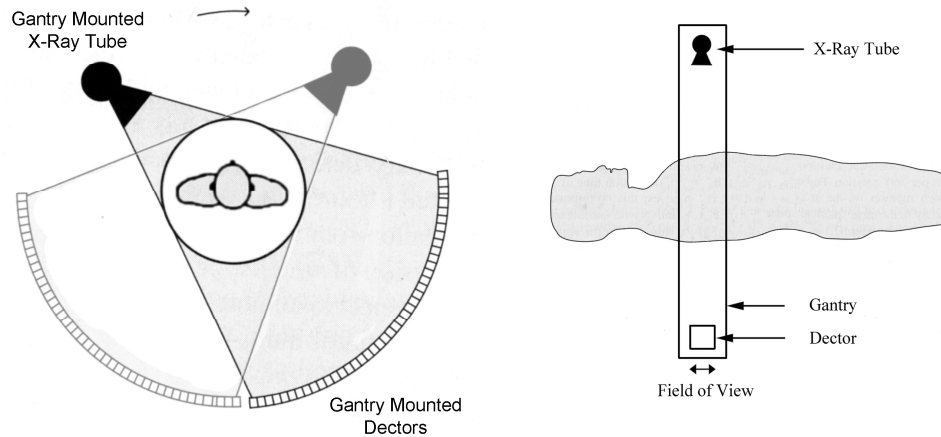


Figure 1-5: Geometry of a CT scanner. Shown are the in-plane and cross section of the scanner. Adapted from *Kalander*.²²

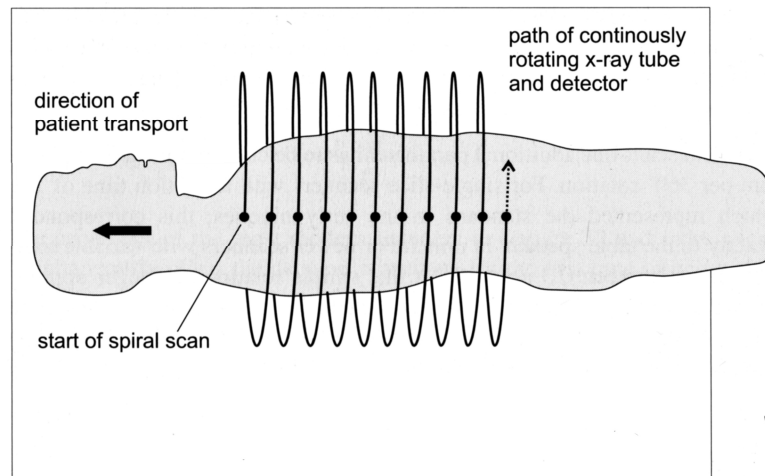


Figure 1-6: Relative motion of x-ray tube to the patient during helical (spiral) scanning. Adapted from *Kalander*.²²

Imaging for the diagnosis and treatment of lung cancer requires volume imaging of the entire thorax (25-30cm in length) which necessitates the use of helical or sequential CT. However, imaging the thorax during respiration violates a central assumption of the

CT image reconstruction process that the object being scanned is *stationary* during the collection of the 360° set of projection data. Movement due to respiration during volume acquisition will result in two types of imaging errors (artifacts).²³⁻²⁷ The first type of artifact occurs within an image slice (intra-slice) due to x-ray projections used to reconstruct the image being acquired at different respiratory phases. *Gagne et al.*²⁵ has extensively studied these image artifacts and found severe intra-slice object distortions that are dependent on the ratio of the gantry rotation time to the period of motion, amplitude of motion, direction of motion and object size. The ratio of the gantry rotation time to the period of motion was the most important variable to control in order to suppress these motion artifacts. Faster acquisition times (increased gantry speed) would decrease these artifacts and provide a snapshot of the object during its motion. In contrast, an extremely slow scan (gantry speed) yields time-averaged images.

The second type of artifact results from the limited AFOV of a CT scanner and the requirement to concatenate images from subvolumes acquired using either separate scans with table incrementation after each scan or helical scans (inter-scan artifacts) to build up a complete volume of an extended organ, for example, the lung. In the likely event that the separate images (subvolumes) are acquired during different respiratory phases the final volume will have inter-scan artifacts. As such, the resulting volume can contain discontinuities marking the individual image (or subvolume) acquisitions (figure 1-7).^{23, 28} *Chen et al.*²⁴ imaged moving spherical objects using helical CT and found that the apparent length of the object could be shortened or lengthened up to two times the amplitude of motion, depending on the scan parameters chosen. *Shimizu et al.*²⁷ studied

the motion of lung tumours with sequential CT and found that the tumour could actually disappear from the axial image in up to 21% of the images.

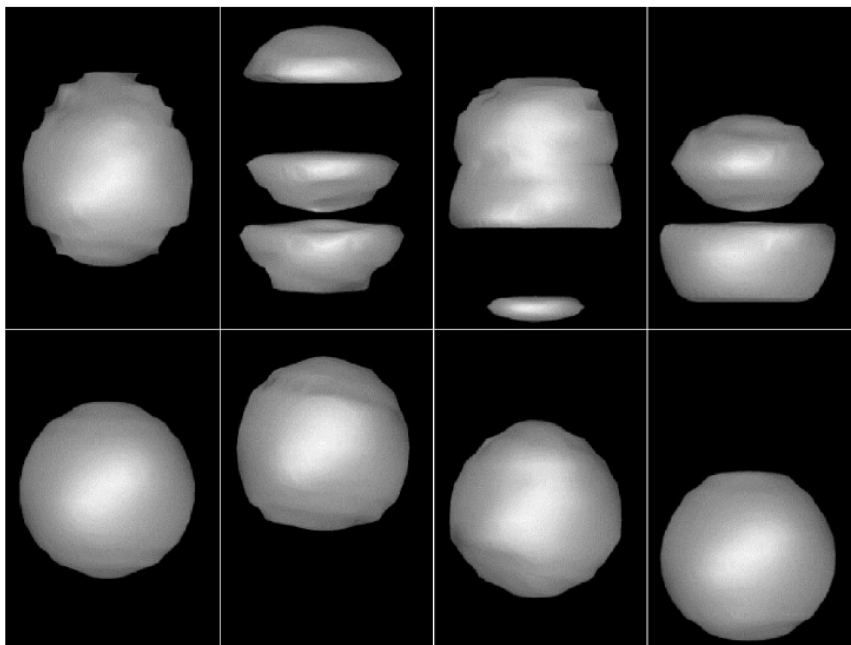


Figure 1-7: Example of inter-scan artifacts from scanning a sphere moving up and down in the vertical direction. Bottom row: true geometry of the sphere as it moved. Top row: Artifacts of the moving sphere when scanned with a helical scanning protocol. Adapted from *Rietzel et al.*²⁹

1.3.4 Treatment Planning and Delivery Issues

From the discussion in section 1.3.3, contouring a lung tumour GTV on CT scans that contain motion related imaging artifacts will be problematic. To overcome the inaccuracies of outlining the tumour on images affected by motion artifact, larger PTV margins are added to the GTV. However, this is a suboptimal solution as the larger irradiated area will increase the dose to the healthy surrounding tissue during treatment

and likely result in more complications. The alternative is to leave the treatment margins small, which will result in poor local control of the tumour due to target 'misses' and inadequate dose deposition to the tumour. Appropriate treatment margins are difficult to determine in the presence of imaging artifacts that result from tumour motion.³⁰ The first step to adequate dose delivery to the tumour is proper imaging of the whole tumour. Methods to overcome the respiratory motion artifacts that occur when CT scanning a lung tumour are presented in the next section.

1.4 Motion Compensation Methods

1.4.1 Slow Rotation CT Scanning

A simple method to minimize artifacts from object motion in CT scanning is to decrease the gantry speed - slow rotation CT scanning.³¹⁻³⁵ The principle of the method is to increase the CT gantry rotation time well above the period of respiration. The result is that each image will be reconstructed using projection data collected over a period longer than a breathing cycle. In the reconstructed volume, the tumour motion is blurred over the entire breathing cycle resulting in a smeared volume image with no discontinuities. The tumour volume (GTV) is contoured around the extent of the motion blur. It is important to note that this contour only encompasses the motion of the tumour during the breathing cycles over which the tumour was scanned. Tumour motion variability during subsequent breathing cycles must be anticipated and additional margins must be added to ensure the entire tumour received the prescribed dose.³² The slow CT scan approach provides time-averaged images, which represent the spatial probability distribution of the tumor and surrounding healthy tissue and can be used to perform dose

calculations. A disadvantage of slow CT scanning is the loss of spatial resolution to the tumour boundaries from motion blurring. This loss of resolution may lead to tumor contouring variations between radiation oncologists resulting in under-dosing to the tumour and overdosing to the surrounding healthy tissue.³⁴

1.4.2 Breath-Hold CT Scanning

The image artifacts that occur as a result of respiratory motion can be minimized by breath hold for the duration of a volume CT scan. Two such scans must be performed, one at the maximum inhalation and one at the maximum exhalation, to obtain the full range of motion of the tumour.³⁶⁻³⁸ This procedure is contingent on the patient's ability to successfully hold their breath over the entirety of the image acquisition, which is less than 10 seconds for modern scanners.²² The two volume CT scans can then be fused and a maximum intensity projection (MIP) volume can be created. Each pixel of a MIP volume is determined by taking the maximum pixel value from the two fused volumes for each pixel location and thus the image shows the tumour at both the inhalation and exhalation positions simultaneously. The advantage of this procedure over the slow CT scan is the reduction of motion blur artifacts (as a result of scanning both lungs while they are stationary). However, this procedure does have some limitations. Patients with compromised lung function may find it difficult to hold their breathing for the duration of the scan. Additionally, if the patient is to be treated while free breathing the range of motion of the tumour calculated from the MIP may not accurately represent the range of motion during treatment because different muscles are used during forced inhalation and exhalation than during free breathing.¹¹ As a result, the tumour may be under or

overdosed, depending on the difference between the free breathing and breath-hold tumor locations.

1.4.3 Four-Dimensional (4D) CT Scanning

A method that has been developed to provide artifact-free 3D volumes of a patient's entire thorax during respiration is four-dimensional CT (4D-CT) scanning. 4D-CT is a generic name for a scanning protocol that produces a times series of 3D images of an object (in this case a patient's thorax) with an axial extent wider than the AFOV of the CT scanner. The basic principle has been implemented using both helical³⁹⁻⁴³ and ciné CT.^{29, 44, 45} When implemented using helical CT a very low pitch (ratio of scan table translation to the AFOV of the scanner) is used in order to collect images over an entire breathing cycle at each slice location. Ciné CT is a form of sequential CT that acquires a time series of images over an entire breathing cycle at one fixed scan position by continuously rotating the scanner gantry and acquiring images. The implementation of both methods requires information provided by a respiratory surrogate marker. The surrogate provides a respiratory trace during image acquisition which is used to tag each individually acquired image with a surrogate respiratory phase value. After the scanning is complete the surrogate data collected is used to create respiratory phase bins (usually between 8 and 12 per breathing cycle). Images are assigned to each bin according to their phase tags. It is assumed that the images within each bin were acquired at the same respiratory phase and are combined to form a 3D volume at that phase. This is done for each of the bins resulting in 8 to 12 3D volumes. This method of 4D-CT, collecting the images first then sorting them after the scanning has been completed, has come into the

widest use and is called retrospective 4D-CT. *Pan et al.*⁴⁶ has published the most comprehensive comparison between helical and ciné retrospective 4D-CT. They concluded that helical 4D-CT is generally faster than ciné 4D-CT, but it is a higher dose procedure and would be slower if rescans are required due to irregular breathing. Prospective 4D-CT^{47, 48} has been developed and consists of triggering (or gating) the CT scanner to acquire an image when the patient is in the desired respiratory phase. This method has yielded similar results to retrospective 4D-CT, however, due to the long acquisition times it has been eclipsed by retrospective 4D-CT.⁴⁹

Many different types of respiratory surrogates have been used to produce 4D-CT volumes. The most common of these surrogates is an external marker that measures the 1-dimensional relative position of a single point on the patient's chest. A charged coupled device (CCD) camera tracks the movement from respiration of two infrared reflective dots on a small plastic box which is placed at a single location on the patient's chest, usually near the xiphoid process, to obtain a respiratory signal.^{29, 39, 45} The commercial version of this system is produced by Varian Medical Systems under the name Real-time Position Monitoring (RPM) device (Palo Alto, CA). Additional methods to measure abdominal displacement from respiration employ either a strain gauge⁴¹ or a pneumatic bellows system.⁴³ All three of these respiratory surrogates work under the assumption that the signal they acquire is highly correlated to the 3-dimensional (3D) motion of the diaphragm, which is the driving force of quiet respiration. Finally, there are two other methods that use the air inhaled and exhaled by the patient during respiration to produce a respiratory surrogate. Spirometry measures the rate of airflow into and out of the patient's mouth during respiration to obtain a breathing surrogate. A

limitation of spirometry is that the device must be periodically adjusted for signal drift.⁴⁴ Alternatively, a thermocouple has been used to measure the temperature of the air in the patient's mouth to obtain a respiratory surrogate curve. The principle behind the thermocouple method is that air exhaled will be increasingly warmer while the air inhaled will be increasingly cooler.⁴² These last two methods assume that the 3D motion of the lung is directly correlated to the flow of air in and out of the lung. It has been shown that spirometry does correlate to the internal air content of the CT images, which can be used as a surrogate for internal motion, better than the amplitude of an external marker.⁵⁰

All of the respiratory curves from surrogates are semi-sinusoidal and periodic with respiration, having an inspiration and expiration phase. The amplitude of the curve can be used to generate a respiratory phase curve that cycles between 0 and 2π radians of phase. The respiratory phase angle is akin to the angle of a sinusoidal curve and describes the position within the respiratory cycle. Algorithms to generate these phase angle curves generally take into account the amplitude of the surrogate curve, the peak at maximum inspiration and the instantaneous period of the respiratory cycle.⁴⁷ For each respiratory surrogate there are two possible methods that can be used to sort the asynchronously acquired images – the amplitude or phase of the surrogate curve. While phase angle sorting was first to be developed, amplitude sorting has been shown to be superior through its ability to handle non-periodic breathing patterns.^{41, 51}

As discussed, a popular method to obtain a respiratory surrogate curve for 4D-CT is to use a marker external to the subject being scanned. In addition to an external marker 4D-CT method, *Pan et al.*⁴⁵ also obtained a respiratory surrogate curve for each acquired cine scan by drawing regions of interest (ROI) over specific anatomical structures within

the images and recording the average values within the ROIs as a function of time. They demonstrated this technique by collecting ciné scans that covered the lower thorax of a ventilated dog. The ROIs were drawn to include a portion of the diaphragm, with the rest of the ROI filled with lung tissue. The values within the ROIs vary during respiration as more or less of the diaphragm entered the ROI. The ciné scans from adjacent scan positions were aligned in space and time by shifting one ciné scan until the peak and trough of its respiratory surrogate curve was aligned with the curve from the adjacent ciné scan. When all the time series of images were so aligned, a 4D-CT dataset had been constructed. The volumes produced by this method were of a quality consistent with volumes produced using an external surrogate marker. However, the procedure was only implemented using the diaphragm. It is uncertain if the respiratory curves derived from the motion of different anatomical locations (i.e. chest wall, diaphragm) would all follow the same shape and phase; if not this could lead to possible phase shifts between the peaks of the curve (e.g. the chest wall lags the motion of the diaphragm). Additionally, the user's choice of the placement of the ROIs, and therefore the resultant curves, are highly subjective.

1.4.4 Treatment Planning and Delivery with 4D-CT

4D-CT provides CT images of the entire volume of the chest and tumour over the course of a respiratory cycle. The GTV of the tumour can be contoured at each respiratory phase and each GTV can be expanded by conventional margins to obtain the corresponding CTV at the same phase. An internal target volume (or ITV) is defined by

overlapping all the CTV contours at different respiratory phases. Finally the ITV is expanded to account for setup uncertainties to obtain the PTV (figure 1-8).^{30, 52}

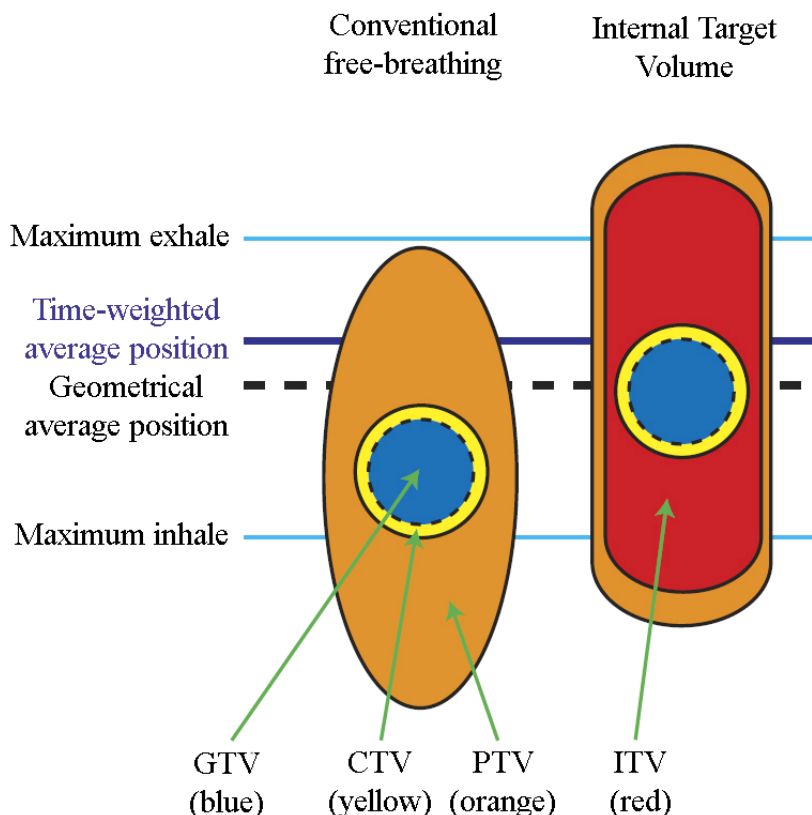


Figure 1-8: Definition of 4D-CT derived treatment margins.

Adapted from *Wolthaus et al.*⁴²

The motion encompassing volume produced from 4D-CT treatment planning provides a more accurate representation of the tumour volume in the presence of respiratory motion. The 4D-CT derived treatment margins require significant time and effort to produce and must be compared against treatment margins produced from other motion-encompassing methods to justify the additional resources required to produce them. In a study comparing fluoroscopy derived treatment margins to 4D-CT derived

treatment margins, it was shown that fluoroscopy overestimated the margins by 52%. As a consequence, treatments performed using fluoroscopic derived treatment margins would have resulted in over-irradiation of healthy tissue during treatment.⁵³ The GTVs derived from 4D-CT have been shown to be significantly different from the GTVs derived from free-breathing helical CT scans; there were also significant differences between the size and shape of the PTVs. In general, the free-breathing helical CT PTVs tended to underestimate the motion of the tumour, while the treatment plans derived from 4D-CT provided a reduction of mean dose to the lung,^{28, 42, 54-56} which is an indicator of radiation pneumonitis.⁸ Additionally, MIP derived GTV contours have been compared to the GTVs composited from 4D-CT volumes at all phases. The MIP GTVs were significantly smaller than the 4D-CT GTVs,⁵⁷ suggesting that MIP GTVs underestimate the tumour volume. 4D-CT derived treatment margins have been shown to be significantly different than the respiratory motion encompassing treatment margins produced by both fluoroscopy and MIP imaging. Additionally, the 4D-CT derived GTVs have been shown to be reproducible between repeat scans.⁵⁸

Knowledge of the position of the tumour over the entire respiratory cycle allows treatment of the tumour at specific respiratory phases. Gated radiotherapy involves the delivery of radiation to the tumour at a specific phase by considering the tumour as a stationary target at the moment of treatment.^{59, 60} The radiation beam is turned on only when the tumour is within the field of view of the beam. The position of the tumour is determined by an external respiratory surrogate that is correlated to the motion of the tumour or by internal fiducial markers that are tracked fluoroscopically. Gated radiotherapy allows for smaller treatment volumes that result in an increase to the

minimum dose delivered to the tumour and a decrease of the mean dose delivered to the lung, esophagus and heart.⁶¹ It is important to note that the correlation between the position of an external marker and the location of the tumour determined with a breath hold scan will not be the same during free-breathing.⁶² Therefore, when performing gated radiotherapy on a free breathing patient it is important to acquire and plan on a free breathing 4D-CT scan. An additional concern of gated radiotherapy is the time required for a patient's treatment session. If, through the action of gating, the radiation duty cycle (ratio of the time the radiation beam is on versus the total treatment time) is approximately 30%, versus 100% for conventional radiation treatment, there will be a three fold increase in treatment time,⁶³ reducing patient throughput.

1.5 Limitations of Current 4D-CT Imaging and Treatment Methods

1.5.1 4D-CT Artifacts

While 4D-CT scanning produces volumes that are an improvement over 3D images acquired without any form of respiratory gating, artifacts are still present in most 4D-CT volumes produced by existing methods. It has been shown in the literature that anywhere from 30%⁶⁴ to 90%⁶⁵ of 4D-CT volumes generated by commercially available methods will contain some form of imaging artifact. The most common artifacts within the 4D-CT volumes are similar to the inter-scan artifacts present when using conventional helical or sequential CT scanning to acquire free-breathing thoracic volumes. These artifacts are a result of combining volumes from temporally misaligned respiratory phases into a single volume. The cause of the artifacts is different in 4D-CT than it was

in convention CT, as will be explored in the following sections. *Yamamoto et al.*⁶⁵ has classified 3 types of inter-scan artifacts with the root cause of each artifact being the same from combining images with varying differences of respiratory phase difference (figure 1-8 b-d). Also found in this study is that the severity of artifact was shown to be significantly correlated with abdominal displacement, respiratory period and root mean squared deviation of the quadratic fit from respiratory curve (an indicator of irregular breathing). The consequence of these artifacts is variations in the size and shape of the contoured GTV volume. The GTVs contoured on the corresponding respiratory phases of the 4D-CTs (with artifacts) were found to be significantly larger than the GTVs contour on the end expiration CT volumes⁶⁶ and on the breath hold 3D CT scan.⁶⁷ As such, it is imperative to have artifact-free 4D-CT volumes so not to invalidate the entire 4D-CT motion correction process.

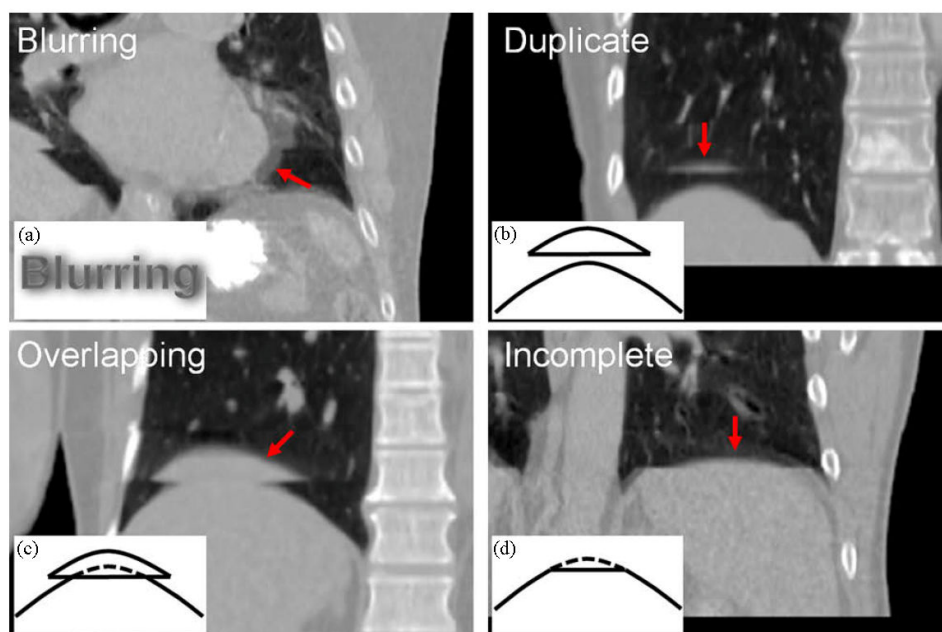


Figure 1-9: Classification of 4D-CT artifacts. (a) Intra-slice artifact. (b-d) Inter-scan artifacts. Adapted from *Yamamoto et al.*⁶⁵

1.5.2 Respiratory Surrogate Correlation Issues

The correlation between the motion of the respiratory surrogate and the anatomy of the subject is integral to the production of artifact-free 4D-CT volumes. Both the degree of correlation and the consistency of correlation will affect the ability to label the images with the correct respiratory phase. There have been conflicting reports over the correlation of the motion of a single external marker and the internal anatomical motion. The studies showing good, consistent correlations have had to phase shift the surrogate signal in order to match the internal motion.⁶⁸⁻⁷⁰ The presence of a phase shift seen in these studies led the authors to caution against trusting the external marker/internal anatomy correlation in the absence of individual patient validation. Studies that claimed good correlations often had Pearson correlation values between internal and external motion as low as 0.60.⁷¹ A study that compared an internal tracking algorithm (using fluoroscopy) to an external method found the internal method to be superior and recommended avoiding external surrogates whenever possible.⁷² The repeated findings of rather poor correlations between motion of an external marker and that of the internal anatomy as well as transient phase shifts between the motions have led researchers to conclude that the relationship between the motion of a surrogate and the corresponding internal anatomy is a highly complex one.⁷³⁻⁷⁵ Not surprisingly, this has led to the development of complex nonlinear predictive algorithms in order to track the motion of the tumour using a respiratory surrogate.^{76, 77} While these methods have exhibited some success, it is further proof that the relationship between the motion of a single external marker and that of the internal anatomy is not necessarily linear or stable. In order to

more properly model the motion of the chest there has been research into tracking multiple external chest markers. When the independent motions of these markers, placed at different locations of the chest, have been compared with each other a phase shift between the separate motions has been found. The authors were able to combine the motions of the multiple markers to provide a surrogate that showed an improved correlation with the internal anatomy.^{78, 79} Thus far, this method of generation of a more reliable respiratory surrogate has not been used to generate 4D-CT volumes.

Only recently has the topic of irregular breathing with regards to respiratory surrogates been studied. Breathing is a complex periodic process with inherent irregularities to it.^{80, 81} A recent paper has compared the ability of an external marker to predict the locations of lung vessels in groups of patients classified as regular and irregular breathers.⁸² The external marker was not a reliable predictor for all patients as only in regular breathers was the marker able to show a consistent and accurate prediction of the locations of lung vessels.

1.5.3 Improvements to 4D-CT Methods

Artifacts within 4D-CT volumes have been shown to occur as a result of incorrect respiratory phase labeling of the acquired images. The first efforts to improve 4D-CT sorting methods focused on adjusting the respiratory phase tagging procedure. Phase angle determination from irregular breathing curves will likely be erroneous because the algorithms used to determine the phase angle use the entire surrogate data curve and assume a constant respiratory period. It can be improved by excluding irregular

breathing sections from the phase angle determination algorithm.⁸³ Another method to improve the phase angle determination is manual selection of the maximum amplitudes of the breathing curve, thus manually deciding the breathing cycle length.⁶⁴ With regards to amplitude based sorting, determining which peaks (troughs) to use as the inhalation (exhalation) maxima can be problematic. *Olsen et al.*⁴³ introduced the idea of percentile based binning that redefined the concept of maximum inhalation and exhalation. Binning based on percentiles provides a margin of error for the bins at the extrema of the breathing cycle and was shown to improve the artifacts in the 4D-CT volumes. While these methods all have shown efficacy in their respective studies they do not address the issue of potentially very poor correlation between the motion of the internal anatomy and that of the respiratory surrogate that ultimately results in artifacts.

Nonlinear image registration has been applied to generate 4D-CT volumes as a method to reduce artifacts. When attempting to model the motion of the lung nonlinear registration is required due to the non-rigid nature of the motion. Initial studies using these methods registered breath-hold volumes at maximum inhalation to exhalation. The resulting vector field describing the displacement between the two volumes was interpolated to provide a volume at any phase between maximum inhalation and exhalation.⁸⁴⁻⁸⁶ Nonlinear registration methods were shown to decrease artifacts in the 4D-CT volumes and were accurate to within 3mm. However, it is likely that in the event of breathing cycle hysteresis the true motion of the tumour could not be determined. A novel method uses nonlinear registration to determine the vector transformation between each volume of a ciné scan and a reference breath hold volume.⁸⁷ The transformations between the ciné scan volumes and the reference volume were correlated with the

respiratory curve from an external marker (similar to the external marker 4D-CT methods) and used to transform the reference volume to a particular respiratory phase. The method improved upon image artifacts in the 4D-CT volumes but again it relies on the correlation between the motion of an external surrogate and that of the internal anatomy.

To avoid external respiratory surrogates entirely, image based 4D-CT methods have been developed. The two recently published methods both derived a respiratory surrogate from the information contained within the image in order to label the acquired images with a respiratory phase value.^{88, 89} The images were then retrospectively sorted according to these phases. Both methods showed a reduction in 4D-CT artifacts as compared to external marker produced 4D-CT volumes.

1.6 Image Similarity Metrics for Matching Respiratory States

As discussed in section 1.3.1, during respiration the chest wall moves in and out while the diaphragm moves up and down. Within a CT image, these structures are represented by image pixel intensity values measured in Hounsfield units (HU). The interface between the chest wall and the air surrounding the patient is distinct due to the large difference in HU values of these two materials (air \sim -1000 HU, soft tissue \sim 0 HU). As the chest wall moves during respiration so does the distinct chest wall/air interface, resulting in a change of the intensity values of the pixels within the CT image.²² More importantly, the density of the lungs changes as air is cycled in and out of the lung space

during respiration. Each pixel can be thought of as a linear combination of air and tissue with weighting factors that are dependent on the amount of each substance within the pixel.⁹⁰ The values of the pixels can vary by a few hundred HUs over the course of the respiratory cycle as more or less air is contained within each pixel. It is then evident that the respiratory phase of the anatomy captured during a CT image is directly relatable to the intensity values contained within the lung and at the chest wall/air interface of a CT image.

Image similarity metrics are used to measure the degree of shared information between two images. This process is simple to implement if two images are acquired using the same image modality, due to the linear relationship between intensity values of the two images. The matching of image pairs according to respiratory phase is an obvious problem to approach using image similarity metrics due to the correlation of the respiratory phase with the intensity values within the image. Mutual information (MI) is a method that compares the information content of one image to another image. This technique is especially useful when there exists a nonlinear relationship between the intensity values of the two images (e.g. acquired by different imaging techniques) being matched and has been used to match the respiratory phase of images acquired using CT angiography and fluoroscopy.⁹¹ For images acquired using the same image modality, the high computational cost of MI is not required and simpler image similarity metrics are used. Normalized cross correlation (NCC) is one such metric that is easy to implement, quick to compute and has been shown to produce excellent results when matching the respiratory phase of images acquired using only CT imaging techniques.⁹² In summary, image similarity metrics are highly useful to match the images to a common respiratory

phase. However, high-cost techniques, such as image matching based on mutual information, need only be used for multi-modality imaging as they add little benefit while consuming more computing resources.

1.7 Research Objectives

The work presented in this thesis is focused on three main objectives.

1. Examine the effect of an inconsistent respiratory amplitude on the correlation between the 3D internal anatomy and a 1D external respiratory marker.
2. Develop an image based 4D-CT algorithm that does *not* require the use of an external respiratory surrogate.
3. Develop and test a method to quantify the uncertainties associated with the image based 4D-CT algorithm.

1.8 Thesis Outline

1.8.1 The relationship between an external marker and the internal lung displacement in a porcine model (Chapter 2).

The correlation between the motion of the internal anatomy of the lung and a commercially available radiation therapy external respiratory marker was tested under induced inconsistent breathing amplitudes. The work was performed in a porcine model using nonlinear registration to quantify the internal displacements. This chapter is based upon research paper entitled, "The effect of an inconsistent breathing amplitude on the

relationship between an external marker and the internal lung deformation in a porcine model," published in *Medical Physics* vol. 37 (11): pp. 5951-5960 (2010) by Pierce G, Wang K, Gaede S, Battista J, Lee TY.

1.8.2 The development of an automated image based 4D-CT sorting algorithm (Chapter 3)

This chapter develops the methodology of an automated image based 4D-CT sorting algorithm. The details of the scanning procedure and volume sorting are covered and tested on 5 patients with lung cancer. An external marker 4D-CT algorithm is used on the same patient data and the results are compared to the automated 4D-CT method. This chapter is adapted from on the research paper, "A fully automated non-external marker 4D-CT sorting algorithm using a serial ciné scanning protocol," published in *Physics in Medicine and Biology* vol. 54 (7): pp. 2049-2066 (2009) by Carnes G, Gaede S, Yu E, Van Dyk J, Battista J, Lee TY.

1.8.3 Applying an animal model to quantify the uncertainties of an image based 4D-CT algorithm (Chapter 4)

In this chapter an animal model and scanning protocol are developed in order to quantify the uncertainties resulting from the automated 4D-CT sorting algorithm presented in Chapter 3. Error models are presented and used to test the two central assumptions of the 4D-CT sorting algorithm. The displacement uncertainties are measured using a nonlinear registration algorithm. This chapter is based on the research paper, "Apply an animal model to quantify the uncertainties of an image based 4D-CT

algorithm," submitted to *Physics in Medicine and Biology* by Pierce G, Wang K, Battista J, Lee TY.

1.8.4 Conclusions (Chapter 5)

In this final chapter the main findings of the thesis are summarized and experimental and clinical relevance of the results are discussed. Topics of interest that have resulted from of this work which merit further study are discussed in a section on future work. The final conclusions of the thesis work are presented.

1.9 References

1. *Canadian Cancer Society's Steering Committee: Canadian Cancer Statistics 2010*. 2010, Canadian Cancer Society: Toronto.
2. Falk, S. and C. Williams, *Lung Cancer*. 3rd ed. 2010: Oxford University Press.
3. Ahmad, S., *Radiotherapy in Lung Cancer*, in *Lung Cancer*, S. Desai, Editor. 2007, Cambridge University Press.
4. DeLuca, P.M., A. Wambersie, and G. Whitmore, *ICRU Report 78*. *Journal of the ICRU*, 2007. **7**(2): p. 210.
5. Armstrong, J.G., et al., *Three-dimensional conformal radiation therapy may improve the therapeutic ratio of high dose radiation therapy for lung cancer*. *Int J Radiat Oncol Biol Phys*, 1993. **26**(4): p. 685-9.
6. Martel, M.K., et al., *Estimation of tumor control probability model parameters from 3-D dose distributions of non-small cell lung cancer patients*. *Lung cancer (Amsterdam, Netherlands)*, 1999. **24**: p. 31-7.
7. Jin, J., et al., *Impact of fraction size on lung radiation toxicity: hypofractionation may be beneficial in dose escalation of radiotherapy for lung cancers*. *Journal of Radiation*, 2010.
8. Kwa, S., J. Lebesque, and J. Theuws, *Radiation pneumonitis as a function of mean lung dose: an analysis of pooled data of 540 patients*. *Journal of Radiation*, 1998.
9. Machtay, M., et al., *Higher Biologically Effective Dose of Radiotherapy is Associated with Improved Outcomes for Locally Advanced Non-Small Cell Lung Carcinoma Treated with Chemoradiation: An Analysis of the Radiation Therapy Oncology Group*. *International journal of radiation oncology, biology, physics*, 2010: p. 1-10.
10. Rosenzweig, K.E., et al., *Results of a phase I dose-escalation study using three-dimensional conformal radiotherapy in the treatment of inoperable nonsmall cell lung carcinoma*. *Cancer*, 2005. **103**: p. 2118-27.
11. West, J.B., *Respiratory Physiology: the essentials*. 4th ed. 1990: Williams & Wilkins.
12. Silverthorn, D.U., *Human Physiology: an integrated approach*. 5th ed. 2010: Pearson Benjamin Cummings.

13. Barnes, E.a., et al., *Dosimetric evaluation of lung tumor immobilization using breath hold at deep inspiration*. International journal of radiation oncology, biology, physics, 2001. **50**: p. 1091-8.
14. Davies, S.C., et al., *Ultrasound quantitation of respiratory organ motion in the upper abdomen*. The British journal of radiology, 1994. **67**: p. 1096-102.
15. Ekberg, L., et al., *What margins should be added to the clinical target volume in radiotherapy treatment planning for lung cancer?* Radiotherapy and oncology : journal of the European Society for Therapeutic Radiology and Oncology, 1998. **48**: p. 71-7.
16. Kubo, H.D. and B.C. Hill, *Respiration gated radiotherapy treatment: a technical study*. Physics in medicine and biology, 1996. **41**: p. 83-91.
17. Mageras, G.S., et al., *Fluoroscopic evaluation of diaphragmatic motion reduction with a respiratory gated radiotherapy system*. Journal of applied clinical medical physics / American College of Medical Physics, 2001. **2**: p. 191-200.
18. Seppenwoolde, Y., et al., *Precise and real-time measurement of 3D tumor motion in lung due to breathing and heartbeat, measured during radiotherapy*. International journal of radiation oncology, biology, physics, 2002. **53**: p. 822-34.
19. Sixel, K., et al., *Digital fluoroscopy to quantify lung tumor motion: potential for patient-specific planning target volumes1*. International Journal of Radiation OncologyBiologyPhysics, 2003. **57**: p. 717-723.
20. Stevens, C.W., et al., *Respiratory-driven lung tumor motion is independent of tumor size, tumor location, and pulmonary function*. International journal of radiation oncology, biology, physics, 2001. **51**: p. 62-8.
21. Keall, P.J., et al., *The management of respiratory motion in radiation oncology report of AAPM Task Group 76*. Med Phys, 2006. **33**(10): p. 3874-900.
22. Kalender, W.A., *Computed Tomography*. 2nd ed. 2005: Publicis Corporate Publishing.
23. Balter, J.M., et al., *Uncertainties in CT-based radiation therapy treatment planning associated with patient breathing• 1*. International Journal of Radiation Oncology• Biology• Physics, 1996. **36**: p. 167-174.
24. Chen, G.T.Y., J.H. Kung, and K.P. Beaudette, *Artifacts in computed tomography scanning of moving objects*. Seminars in radiation oncology, 2004. **14**: p. 19-26.
25. Gagné, I.M. and D.M. Robinson, *The impact of tumor motion upon CT image integrity and target delineation*. Medical Physics, 2004. **31**: p. 3378.

26. Berbeco, R.I., et al., *A technique for respiratory-gated radiotherapy treatment verification with an EPID in cine mode*. Phys Med Biol, 2005. **50**(16): p. 3669-79.
27. Shimizu, S., et al., *Impact of respiratory movement on the computed tomographic images of small lung tumors in three-dimensional (3D) radiotherapy*. International journal of radiation oncology, biology, physics, 2000. **46**: p. 1127-33.
28. Rietzel, E., et al., *Four-dimensional image-based treatment planning: Target volume segmentation and dose calculation in the presence of respiratory motion*. Int J Radiat Oncol Biol Phys, 2005. **61**(5): p. 1535-50.
29. Rietzel, E., T. Pan, and G.T.Y. Chen, *Four-dimensional computed tomography: Image formation and clinical protocol*. Medical Physics, 2005. **32**: p. 874.
30. Keall, P., J. Belderbos, and F. Kong, *Physical Basis of Modern Radiotherapy: Dose and Volume*, in *Principles and Practice of Lung Cancer*, H. Pass, et al., Editors. 2010, Lippincott Williams & Williams.
31. Chinneck, C.D., M. McJury, and a.R. Hounsell, *The potential for undertaking slow CT using a modern CT scanner*. The British journal of radiology, 2010. **83**: p. 687-93.
32. Lagerwaard, F.J., et al., *Multiple "slow" CT scans for incorporating lung tumor mobility in radiotherapy planning*. International journal of radiation oncology, biology, physics, 2001. **51**: p. 932-7.
33. van Sörnsen de Koste, J., et al., *Are multiple CT scans required for planning curative radiotherapy in lung tumors of the lower lobe?* International journal of radiation oncology, biology, physics, 2003. **55**: p. 1394-1399.
34. Mori, S., et al., *Physical evaluation of CT scan methods for radiation therapy planning: comparison of fast, slow and gating scan using the 256-detector row CT scanner*. Physics in medicine and biology, 2006. **51**: p. 587-600.
35. van Sörnsen de Koste, J.R., et al., *Dosimetric consequences of tumor mobility in radiotherapy of stage I non-small cell lung cancer—an analysis of data generated using 'slow' CT scans*. Radiotherapy and oncology: journal of the European Society for Therapeutic Radiology and Oncology, 2001. **61**: p. 93.
36. Aruga, T., et al., *Target volume definition for upper abdominal irradiation using CT scans obtained during inhale and exhale phases*. International journal of radiation oncology, biology, physics, 2000. **48**: p. 465-9.
37. Balter, J.M., et al., *Improvement of CT-based treatment-planning models of abdominal targets using static exhale imaging*. International Journal of Radiation Oncology• Biology• Physics, 1998. **41**: p. 939-943.

38. Yamada, K., et al., *Improvement of three-dimensional treatment planning models of small lung targets using high-speed multi-slice computed tomographic imaging*. International journal of radiation oncology, biology, physics, 2002. **54**: p. 1210-6.
39. Keall, P.J., et al., *Acquiring 4D thoracic CT scans using a multislice helical method*. Physics in Medicine and Biology, 2004. **49**: p. 2053-2067.
40. Vedam, S.S., et al., *Acquiring a four-dimensional computed tomography dataset using an external respiratory signal*. Phys Med Biol, 2003. **48**(1): p. 45-62.
41. Wink, N., C. Panknin, and T.D. Solberg, *Phase versus amplitude sorting of 4D-CT data*. J Appl Clin Med Phys, 2006. **7**(1): p. 77-85.
42. Wolthaus, J.W.H., et al., *Comparison of different strategies to use four-dimensional computed tomography in treatment planning for lung cancer patients*. International journal of radiation oncology, biology, physics, 2008. **70**: p. 1229-38.
43. Olsen, J.R., et al., *Effect of novel amplitude/phase binning algorithm on commercial four-dimensional computed tomography quality*. International journal of radiation oncology, biology, physics, 2008. **70**: p. 243-52.
44. Low, D., et al., *A method for the reconstruction of four-dimensional synchronized CT scans acquired during free breathing*. Medical Physics, 2003. **30**: p. 1254.
45. Pan, T., et al., *4D-CT imaging of a volume influenced by respiratory motion on multi-slice CT*. Medical Physics, 2004. **31**: p. 333.
46. Pan, T., *Comparison of helical and cine acquisitions for 4D-CT imaging with multislice CT*. Medical Physics, 2005. **32**: p. 627.
47. Ford, E.C., et al., *Respiration-correlated spiral CT: A method of measuring respiratory-induced anatomic motion for radiation treatment planning*. Medical Physics, 2003. **30**: p. 88.
48. Fitzpatrick, M.J., et al., *Displacement-based binning of time-dependent computed tomography image data sets*. Medical Physics, 2006. **33**: p. 235.
49. Langner, U.W. and P.J. Keall, *Quantification of artifact reduction with real-time cine four-dimensional computed tomography acquisition methods*. International journal of radiation oncology, biology, physics, 2010. **76**: p. 1242-50.
50. Lu, W., et al., *Comparison of spirometry and abdominal height as four-dimensional computed tomography metrics in lung*. Medical Physics, 2005. **32**: p. 2351.

51. Lu, W., et al., *A comparison between amplitude sorting and phase-angle sorting using external respiratory measurement for 4D CT*. Medical Physics, 2006. **33**: p. 2964.
52. *International Commission on Radiation Units and Measurements (ICRU) Report 62*. 1999.
53. van der Geld, Y.G., et al., *Reproducibility of target volumes generated using uncoached 4-dimensional CT scans for peripheral lung cancer*. Radiation oncology (London, England), 2006. **1**: p. 43.
54. Alasti, H., et al., *A novel four-dimensional radiotherapy method for lung cancer: imaging, treatment planning and delivery*. Physics in medicine and biology, 2006. **51**: p. 3251-67.
55. Starkschall, G., et al., *Potential dosimetric benefits of four-dimensional radiation treatment planning*. International journal of radiation oncology, biology, physics, 2009. **73**: p. 1560-5.
56. Hof, H., et al., *4D-CT-based target volume definition in stereotactic radiotherapy of lung tumours: comparison with a conventional technique using individual margins*. Radiotherapy and oncology : journal of the European Society for Therapeutic Radiology and Oncology, 2009. **93**: p. 419-23.
57. Park, K., et al., *Do maximum intensity projection images truly capture tumor motion?* International journal of radiation oncology, biology, physics, 2009. **73**: p. 618-25.
58. Guckenberger, M., et al., *Is a single respiratory correlated 4D-CT study sufficient for evaluation of breathing motion?* International journal of radiation oncology, biology, physics, 2007. **67**: p. 1352-9.
59. Ford, E.C., et al., *Evaluation of respiratory movement during gated radiotherapy using film and electronic portal imaging*. International journal of radiation oncology, biology, physics, 2002. **52**: p. 522-31.
60. Vedam, S.S., et al., *Determining parameters for respiration-gated radiotherapy*. Medical Physics, 2001. **28**: p. 2139.
61. Vlachaki, M., et al., *Impact of respiratory gating using 4-dimensional computed tomography on the dosimetry of tumor and normal tissues in patients with thoracic malignancies*. American journal of clinical oncology, 2009. **32**: p. 262-8.
62. Hunjan, S., et al., *Lack of correlation between external fiducial positions and internal tumor positions during breath-hold CT*. International journal of radiation oncology, biology, physics, 2010. **76**: p. 1586-91.

63. Jiang, S.B., *Technical aspects of image-guided respiration-gated radiation therapy*. Medical dosimetry : official journal of the American Association of Medical Dosimetrists, 2006. **31**: p. 141-51.
64. Rietzel, E. and G.T.Y. Chen, *Improving retrospective sorting of 4D computed tomography data*. Medical Physics, 2006. **33**: p. 377.
65. Yamamoto, T., et al., *Retrospective analysis of artifacts in four-dimensional CT images of 50 abdominal and thoracic radiotherapy patients*. International journal of radiation oncology, biology, physics, 2008. **72**: p. 1250-8.
66. Persson, G.F., et al., *Deviations in delineated GTV caused by artefacts in 4DCT*. Radiotherapy and oncology : journal of the European Society for Therapeutic Radiology and Oncology, 2010. **96**: p. 61-6.
67. Fredberg Persson, G., et al., *Artifacts in conventional computed tomography (CT) and free breathing four-dimensional CT induce uncertainty in gross tumor volume determination*. International journal of radiation oncology, biology, physics, 2010: p. 1-8.
68. Gierga, D.P., et al., *The correlation between internal and external markers for abdominal tumors: implications for respiratory gating*. International journal of radiation oncology, biology, physics, 2005. **61**: p. 1551-8.
69. Ionascu, D., et al., *Internal-external correlation investigations of respiratory induced motion of lung tumors*. Medical Physics, 2007. **34**: p. 3893.
70. Gaede, S., et al., *The use of CT density changes at internal tissue interfaces to correlate internal organ motion with an external surrogate*. Physics in medicine and biology, 2009. **54**: p. 259-73.
71. Ahn, S., *A feasibility study on the prediction of tumour location in the lung from skin motion*. British Journal of Radiology, 2004. **77**: p. 588-596.
72. Korreman, S.S., et al., *Comparison of respiratory surrogates for gated lung radiotherapy without internal fiducials*. Acta oncologica (Stockholm, Sweden), 2006. **45**: p. 935-42.
73. Hoisak, J.D.P., et al., *Correlation of lung tumor motion with external surrogate indicators of respiration*. International journal of radiation oncology, biology, physics, 2004. **60**: p. 1298-306.
74. Koch, N., et al., *Evaluation of internal lung motion for respiratory-gated radiotherapy using MRI: Part I--correlating internal lung motion with skin fiducial motion*. International journal of radiation oncology, biology, physics, 2004. **60**: p. 1459-72.

75. Ozhasoglu, C. and M.J. Murphy, *Issues in respiratory motion compensation during external-beam radiotherapy*. Int J Radiat Oncol Biol Phys, 2002. **52**(5): p. 1389-99.
76. Isaksson, M., J. Jalden, and M.J. Murphy, *On using an adaptive neural network to predict lung tumor motion during respiration for radiotherapy applications*. Medical Physics, 2005. **32**: p. 3801.
77. Kanoulas, E., et al., *Derivation of the tumor position from external respiratory surrogates with periodical updating of the internal/external correlation*. Phys Med Biol, 2007. **52**(17): p. 5443-56.
78. Hughes, S., et al., *Assessment of two novel ventilatory surrogates for use in the delivery of gated/tracked radiotherapy for non-small cell lung cancer*. Radiotherapy and oncology : journal of the European Society for Therapeutic Radiology and Oncology, 2009. **91**: p. 336-41.
79. Yan, H., et al., *The investigation on the location effect of external markers in respiratory-gated radiotherapy*. Journal of applied clinical medical physics / American College of Medical Physics, 2008. **9**: p. 2758.
80. Benchetrit, G., *Breathing pattern in humans: diversity and individuality*. Respiration physiology, 2000. **122**: p. 123-9.
81. Bruce, E.N., *Temporal variations in the pattern of breathing*. Journal of applied physiology (Bethesda, Md. : 1985), 1996. **80**: p. 1079-87.
82. Spadea, M.F., et al., *Uncertainties in lung motion prediction relying on external surrogate: a 4DCT study in regular vs. irregular breathers*. Technol Cancer Res Treat, 2010. **9**(3): p. 307-16.
83. Pan, T., X. Sun, and D. Luo, *Improvement of the cine-CT based 4D-CT imaging*. Medical Physics, 2007. **34**: p. 4499.
84. Sarrut, D., et al., *Simulation of four-dimensional CT images from deformable registration between inhale and exhale breath-hold CT scans*. Medical Physics, 2006. **33**: p. 605.
85. Schreiber, E., G.T.Y. Chen, and L. Xing, *Image interpolation in 4D CT using a BSpline deformable registration model*. International journal of radiation oncology, biology, physics, 2006. **64**: p. 1537-50.
86. Xu, S., et al., *Lung deformation estimation and four-dimensional CT lung reconstruction*. Academic radiology, 2006. **13**: p. 1082-92.
87. McClelland, J., et al., *A continuous 4D motion model from multiple respiratory cycles for use in lung radiotherapy*. Medical Physics, 2006. **33**: p. 3348.

88. Li, R., et al., *4D CT sorting based on patient internal anatomy*. Physics in medicine and biology, 2009. **54**: p. 4821-33.
89. Zeng, R., et al., *Iterative sorting for four-dimensional CT images based on internal anatomy motion*. Medical Physics, 2008. **35**: p. 917.
90. Lu, W., et al., *Quantitation of the reconstruction quality of a four-dimensional computed tomography process for lung cancer patients*. Medical Physics, 2005. **32**: p. 890.
91. Martin-Leung, B., et al., *Mutual information based respiration detection*. International Congress Series, 2003. **1256**: p. 1085-1092.
92. Eck, K. and J. Bredno, *Absolute alignment of breathing states using image similarity derivatives*. Imaging 2005: Visualization, Image, 2005.

Chapter 2

The relationship between an external marker and the internal anatomic lung displacement in a porcine model

2.1 Introduction

Respiration-induced lung tumour motion requires the use of large margins around the tumour to ensure adequate target coverage in conventional radiation treatment of lung cancer.¹⁻⁵ Gating the radiation beam to one respiratory phase (gated radiotherapy) enables a potential reduction in the size of these margins and allows for dose escalation.⁶⁻¹¹ However, any gating errors could result in geographical target misses, resulting in reduced tumour control and over-irradiation of the healthy lung tissue, potentially resulting in pneumonitis.¹²⁻¹⁴

Gated radiotherapy usually relies on an external respiratory marker to predict the internal location of the tumour. An external surrogate marker commonly used in clinical practice is the Varian Real-time Position Management (RPM) device, which records the motion of a small plastic block placed on the chest using a camera and presents the data as one dimensional curve of varying amplitude versus time.^{10, 15-18} Besides being used as a predictor of the location of the tumour during therapy, the RPM amplitude curve can also be used to sort CT images according to respiratory phase into 4 dimensional CT volumes (amplitude based 4D-CT). Prior to treatment, a 4D-CT scan is used to develop the gated radiotherapy treatment plan, including the choice of optimal respiratory phase for delivering radiation. Both 4D-CT sorting and gated radiotherapy rely on the

assumption that the motion of the marker is strictly correlated to the motion of anatomy (target and healthy tissue) and that this correlation is maintained during individual treatment sessions over the period of several weeks of fractionated therapy. Violation of this assumption would invalidate the use of the 4D-CT plan and associated RPM gated radiotherapy delivery.

Several studies have investigated the correlation between an external respiratory marker and internal anatomy in patients.¹⁹⁻²⁶ These studies compared the fluoroscopically tracked motion of gold fiducial markers or internal anatomical landmarks (e.g. diaphragm) to the unidirectional motion of the external surrogate marker. In general, the motion of the marker correlated reasonably well with that of the fiducials and internal anatomy. However, none of these studies investigated the potentially negative effect of inconsistent breathing amplitudes.^{22-24, 26} Other studies have investigated the correlation between the programmable motion of a lung phantom and an external marker using patient respiratory data with inconsistent breathing amplitudes.^{27, 28} The conclusions of these studies may be limited since the phantoms do not exhibit visco-elastic deformations, which are present within the lungs. In attempts to simulate visco-elastic lung properties similar to human lungs, there have been developments of both an *ex-vivo* lung preparation²⁹ and an inorganic deformable phantom.³⁰ These systems show promise in their respective applications but lack the chest wall/pleura and lung interaction properties required for the proper testing of an external marker system.

In this work, we investigated the effect of inducing an inconsistent amplitude of breathing on the relationship between the one-dimensional motion of an external marker and average three-dimensional motion within regions of interest in both the right (RL)

and left lungs (LL) and the chest wall (CW) of a pig. Motions, calculated from the vector displacement fields resulting from a nonlinear registration algorithm within specific regions of interest are used as a surrogate for the motion of a tumour imbedded within lung tissue. Two separate experiments are performed to examine the relationship between the internal anatomy and the external marker. The first experiment tested the correlation between the anatomy and the external marker at a single time point by looking for anatomical differences between volumes collected during consistent and inconsistent breathing, sorted into the same respiratory phase bins according to the RPM amplitude values (i.e. amplitude based 4D-CT sorting). The second experiment investigated the correlation between the anatomy and the external marker over entire breathing cycles by performing a linear regression between the motion of the anatomy (calculated using nonlinear registration), within three regions of interest, and the motion of the external marker. Comparisons were made between breathing cycles categorized as consistent or inconsistent to determine if the consistency of the amplitude had an effect on the correlation. If this relationship is affected by variations in the breathing amplitude, then measures to prevent or account for inconsistencies in amplitude during acquisition of amplitude based 4D-CT scans, as well as during external marker gated radiotherapy, are warranted.

2.2 Methods

2.2.1 Image Acquisition

Four separate anesthetized and ventilated (Harvard Apparatus, Holliston, MA) female Landrace cross pigs were studied 3 times each. Scanning was performed on a GE

Healthcare HD750 CT scanner (Waukesha, WI). The breathing rate of the pigs was set at 20 breaths/min. In each study, a 4.0 cm section of the animal was scanned 20 times. Each (ciné) scan was performed with x-rays continuously on for 3.6 s, 0.6 s longer than the average length of a breathing cycle and used the following scan parameters: 200 mA, 120 kVp, 64×0.625 mm slices, and a gantry rotation time of 0.4 s. The pig's breathing amplitude was varied by periodically crimping the ventilator gas return tube at a rate of once per 3 seconds. Each ciné scan was retrospectively reconstructed into a time series of volumes with a time spacing of 0.1 s, resulting in 33 volumes in each series. A Varian RPM system (Varian Medical Systems, Palo Alto, CA), which was synchronized to the CT scanner to provide an x-ray on time-stamp on the recorded RPM amplitude versus time curve. The (RPM) amplitude curve depicted the relative height of a location on the animal's chest (marked by a reflective block) continuously for the duration of the 20 ciné scans in a study. The reflective block was placed within the field of view of the CT scanner to allow for the best possible correlation between the internal motion and external amplitude curve.

2.2.2 Categorization of Breathing Patterns

The time points of end exhalation and end inhalation in the entire RPM amplitude versus time curve collected during each study (20 ciné scans) were found using a normalized cumulative amplitude histogram created from the curve. An example of an amplitude histogram and the resulting normalized cumulative histogram from a study is shown in figure 2-1. Following the lead of *Lu et al.*,³¹ the end of expiration amplitude was assigned as the 1st percentile of the normalized cumulative histogram while the end

of inspiration amplitude was assigned as the 95th percentile. A scan was categorized as a consistent amplitude scan (CAS) if both the minimum expiration and the maximum inhalation amplitudes during the scan were less than the 1st and 95th percentile amplitudes, respectively (figure 2-2). All other breathing cycles were classified as inconsistent amplitude scans (IAS). The inconsistent amplitude definitions used included two types of breathing cycles: one in which exhalation was arrested before it reach "normal" end exhalation, or underbreathing (1st percentile), and one in which inhalation was exceeded "normal" end inhalation, or overbreathing (95th percentile).

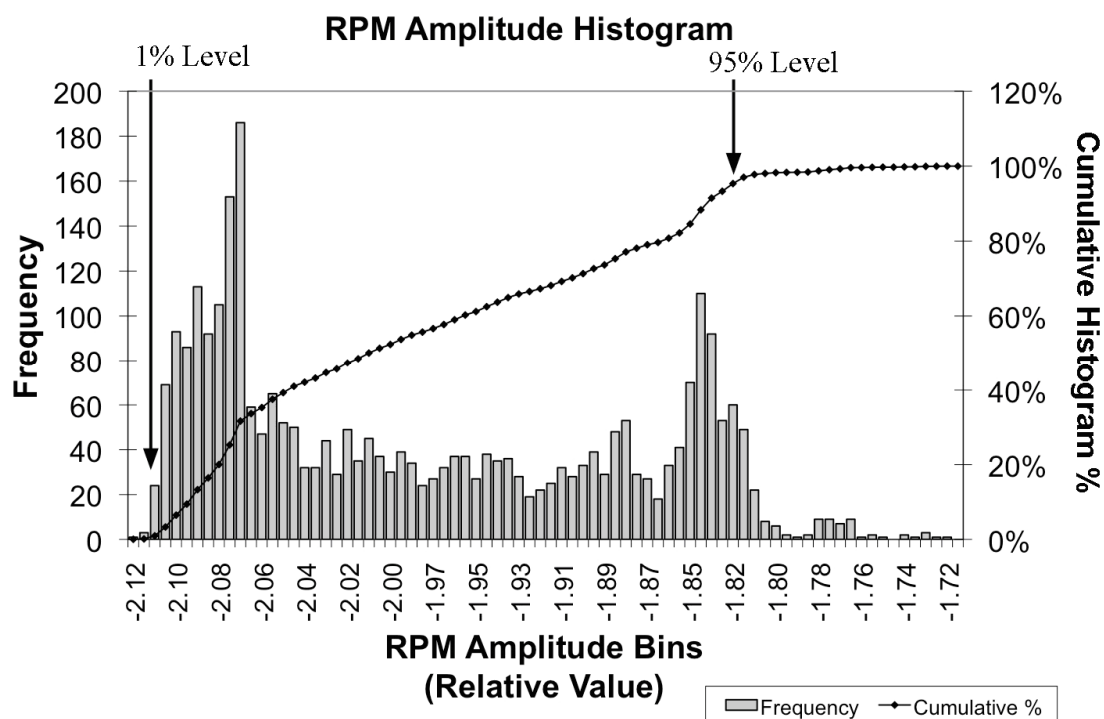


Figure 2-1: Histogram of pig RPM plotted with the cumulative histogram curve. The percentile bins used to determine the maximum inspiration and maximum expiration are marked.

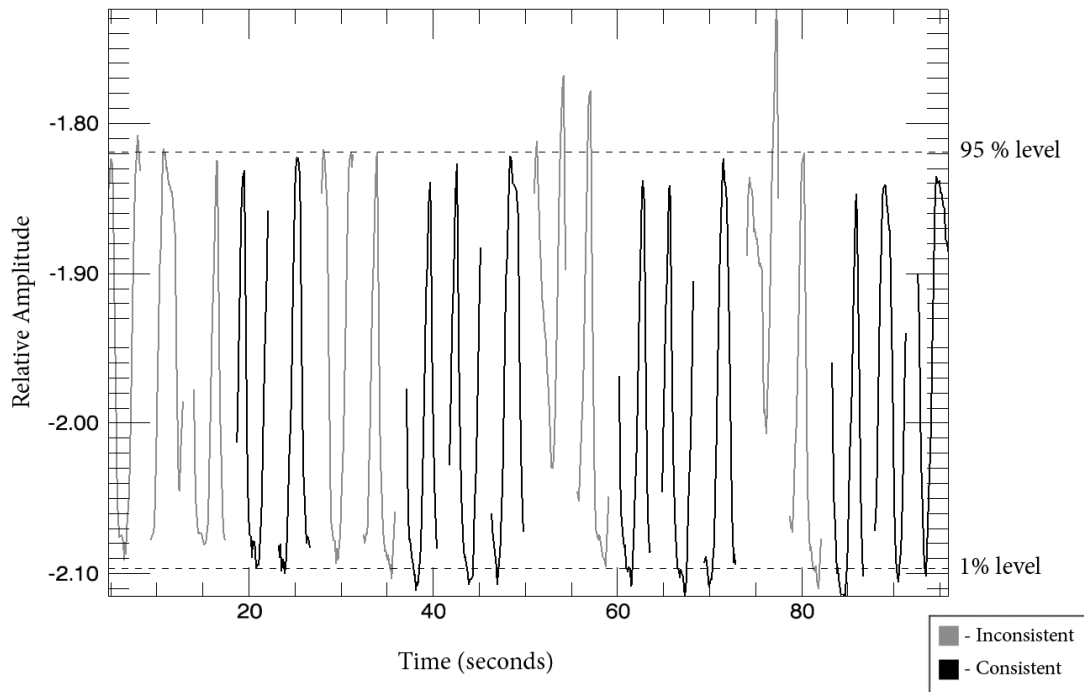


Figure 2-2: Pig RPM breath cycle with consistent and inconsistent breathing cycles categorized according to the percentile definitions

2.2.3 Choosing a Reference Scan (RS)

For each study of 20 ciné scans, a reference scan (RS) was chosen from the set of CASs. The first step in choosing a RS was to truncate the each CAS RPM amplitude curve to exactly one period since, as described in section 2.2.1, each ciné scan duration was 0.6 s longer than a respiratory period. The truncated curve was then translated to begin at maximum expiration. Then the truncated and translated RPM amplitude curve from each CAS was crosscorrelated with all the other CASs and the maxima, for each translated CAS, of the Pearson crosscorrelation values were averaged. After this was performed for each CAS within a study, the highest average maximum Pearson cross-correlation value was accepted as the RS.

2.2.4 4D-CT Sorting Algorithm

In this section, the 4D-CT sorting algorithm used in our investigations is briefly described. CT volumes from a ciné scan were sorted into phase bins created by first dividing the interval between the maximum expiration and maximum inspiration of the RS amplitude curve into five equally spaced bins. These five bins, on the positive slope of the RPM curve, were used to sample the inspiration phase of the breathing cycle. Three additional bins on the negative slope of the RPM curve were used to sample the expiration phase. As shown in figure 2-3, the phase bins were chosen such that the centers of the first and last (fifth) bin on the positive slope of the RPM amplitude curve corresponded with the minimum (exhalation) and maximum (inhalation) amplitude of the reference scan.

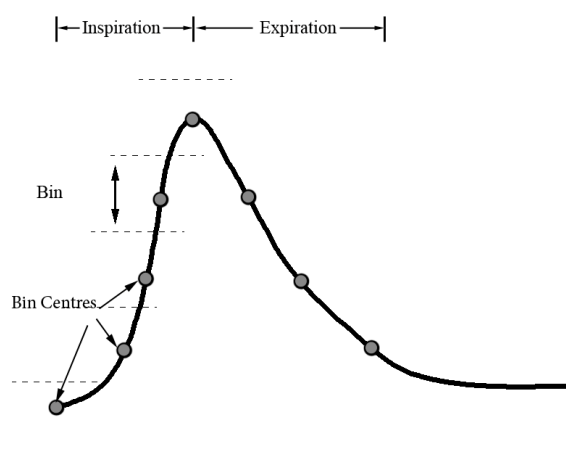


Figure 2-3: Example of reference scan curve divided into the respiratory sorting bins

The volumes from each ciné scan (CAS, IAS, or RS) were sorted using their associated RPM amplitude values. If multiple RPM amplitude values occurred within a phase bin, the RPM value (and associated volume) closest to the center of the phase bin was selected. Conversely, if there were no RPM amplitude values within a phase bin, then no volume was selected. These will be referred to as the sorted CAS, sorted IAS, and sorted RS data.

2.2.5 Subsampling of Ciné Scans

The number of volumes in each scan (CAS, IAS, or RS) was reduced from 33 at 0.1 s intervals to 12 at 0.3 s intervals by selecting every fourth volume from the time series, beginning with the first volume. The subsampled scans were designated CAS₁₂, IAS₁₂, and RS₁₂ for consistent amplitude scan, inconsistent amplitude scan, and reference scan, respectively.

2.2.6 Nonlinear Registration Algorithm

The anatomical displacements between two volumes was quantified as a vector field using nonlinear registration.³² The algorithm has been optimized for lung images and utilized a multiresolution strategy to determine the minimum vector field required to register the two volumes. The algorithm began with both volumes at 1/4 the native

resolution and the vector field at 1/8 native image resolution. The cost function of the optimization process consisted of two terms:

$$\text{cost function} = \left\{ \begin{array}{ll} (1 - NCC) + \frac{cd^3}{d_{\max}^3 - d^3} & \text{if } d^3 < d_{\max}^3 \\ \infty & \text{otherwise} \end{array} \right\} \quad (2.1)$$

The first term is the difference between 1.0 and the normalized cross-correlation (NCC) between the two volumes; the second term penalizes large deformations and limits the vector length (d) to below a set maximum (d_{\max}). The constant c determines the relative weighting between the two terms and was determined by registering test volumes with known deformations. A value of 1.2 was found to produce the smallest residual displacement errors for lung volumes. For each volume resolution, the cost function was optimized using the Nelder–Mead simplex algorithm³³ until it ceased to decrease. The resulting displacement vector field was smoothed using a 3D mean smoothing algorithm to limit discontinuities that may have arisen from optimizing each vector independently. The algorithm then deformed the source volume using the smoothed vector field, increased the resolution of the volumes and the vector field by twofold, and began another round of optimization. The process continued until the volumes had reached their native resolution. The result of the registration algorithm was a three-dimensional displacement vector field at 1/2 the native resolution of the volumes. For the analysis of the effect of inconsistent breathing amplitudes, the magnitude of the displacement vector field was calculated using:

$$|r| = \sqrt{\bar{x}^2 + \bar{y}^2 + \bar{z}^2} \quad (2.2)$$

where \bar{x} , \bar{y} , and \bar{z} are the orthogonal vector components of the vector field and $|r|$ is the magnitude of displacement. The magnitude of the displacement vector field can then be displayed as an image (figure 2-4).

The accuracy of the nonlinear registration algorithm was determined using volumes provided by the DIR-laboratory group.³⁴ Registrations were performed between the inspiration and expiration volumes of five full lung data sets. The error of the nonlinear registration algorithm was quantified by averaging the differences of over 300 landmarks previously selected by the DIR-laboratory group using a software assisted selection process on the registered inspiration and expiration volumes.

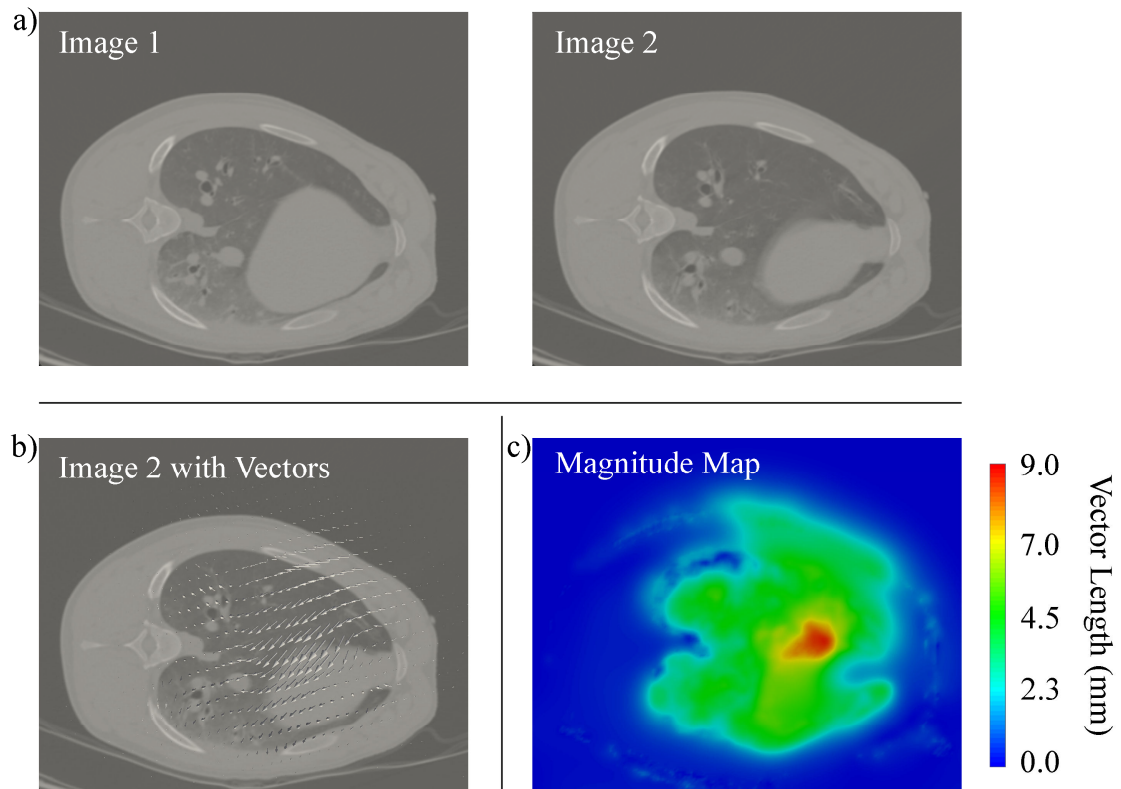


Figure 2-4: Nonlinear registration example (a) Axial images from two volumes collected at different time points of the breathing cycle. (b) The optimum deformation vector field determined with nonlinear registration to warp image 1 to image 2 is displayed superimposed on image 2. (c) Image of the magnitude of deformation vector field shown in (b).

2.2.7 Experiments and Analysis

2.2.7.1 Effect of inconsistent breathing amplitude on RPM prediction accuracy

To determine the effect of the inconsistent breathing amplitude on the accuracy of the RPM amplitude curve to predict the internal anatomy at specific time points, the data sorted using the 4D-CT protocol were used (section 2.2.4). The volumes from the sorted

CAS and IAS were registered with those of the sorted RS at the same respiratory phase using the nonlinear registration algorithm (section 2.2.6). The magnitude of deformation vector fields was calculated using equation 2.2 (figure 2-4).

Three cylindrical ROIs, one each in the left lung (LL), right lung (RL), and the lateral chest wall (CW), were drawn in the maximum inspiration volume of the sorted RS with radius of approximately 2.5 cm and length 2.8 cm (slices 10–54). Figure 2-5 shows the locations of the ROIs and the RPM box on an axial image of one of the pigs. The ROIs were overlaid on the displacement vector fields and the average magnitude of displacement in each ROI was recorded for every phase of sorted CAS and IAS. The intraphase displacement results were tested for significant differences between the sorted CAS and IAS using independent sample two-tailed student's t-test or Mann–Whitney U test for normally and non-normally distributed data, respectively. Significance was declared at $p < 0.05$ level. All statistical calculations were performed using SPSS (SPSS Inc., Chicago, IL).

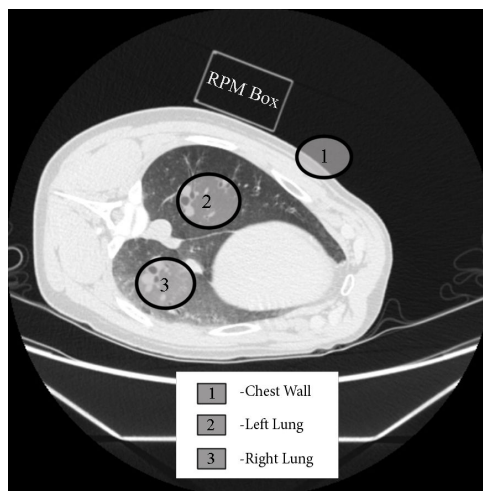


Figure 2-5: Location of ROIs on axial image of a pig

In addition, we sought to determine if there was any significant difference in the difference of a sorted RPM amplitude value from the center point of the bin into which it was sorted, between volumes from sorted CAS and IAS. A two-tailed unpaired Student's t-test was performed on the data.

2.2.7.2 Effect of inconsistent breathing on RPM correlation with anatomy

For this investigation, magnitude of the anatomical displacements of each volume in the subsampled cine scans CAS_{12} and IAS_{12} with respect to the maximum expiration volume in RS_{12} were determined using nonlinear registration and the magnitude of displacements calculated using equation 2.2 (figure 2-4c).

The same cylindrical ROIs as in section 2.2.7.1 above were drawn in the maximum inspiration CT volume from the RS_{12} series and overlaid on the magnitude displacement maps. The average displacement magnitude within the ROIs was recorded, resulting in three magnitude displacement curves, one for each ROI, for every CAS_{12} and IAS_{12} . Since the displacements of CAS_{12} and IAS_{12} were calculated with respect to the maximum expiration volume in the subsampled RS_{12} , the RPM amplitude value of the maximum expiration volume in RS_{12} was subtracted from the entire RPM amplitude curve to give RPM_{ref} to be used for the regressions. A linear regression was performed between each ROI displacement curve from CAS_{12} or IAS_{12} , and the corresponding RPM values from the RPM_{ref} curve. The results of the regression analyses (Pearson coefficient, slope, and intercept) from CAS_{12} and IAS_{12} were compared for significant differences using independent sample two-tailed student's t-test or Mann-Whitney U test for

normally and non-normally distributed data, respectively. Significance was declared at $P < 0.05$ level. All statistical calculations were performed using SPSS (SPSS Inc., Chicago, IL).

2.3 Results

The results from the nonlinear registration error analysis using the DIR-laboratory³⁴ data sets are shown in table 2-1. The table displays the average distance between the user selected landmarks before and after the registration of the inspiration and expiration volumes. In all cases, the distances between landmark points decreased. The superior-inferior direction had greater errors (residual magnitudes of displacement) than the other two directions. The lowest total error was 1.18 mm (decreased from 3.89 mm before registration), while the largest error was 2.34 mm (decreased from 9.83 mm).

Table 2-1: Results of nonlinear registration analysis

Average displacement difference between preselected landmarks in expiration and inspiration volumes after non-linear registration					
Results in mm					
Case		Right-Left (x)	Anterior-Posterior (y)	Superior-Inferior (z)	$ r = \sqrt{\bar{x}^2 + \bar{y}^2 + \bar{z}^2}$
1	Before Registration	0.59	0.69	3.56	3.89
	After Registration	0.40	0.46	0.89	1.18
2	Before Registration	0.71	0.70	3.78	4.34
	After Registration	0.51	0.54	0.98	1.38
3	Before Registration	1.23	1.35	6.33	6.94
	After Registration	0.59	0.59	1.40	1.81
4	Before Registration	1.01	1.42	9.39	9.83
	After Registration	0.88	0.78	1.70	2.34
5	Before Registration	0.90	1.70	6.68	7.48
	After Registration	0.89	0.83	1.65	2.31

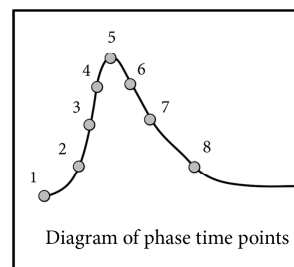
2.3.1 RPM Prediction Accuracy Experiment

The average magnitude of displacements (and standard deviations) of the sorted CASs from the sorted RS over all eight phases from the 12 studies were 1.29 (0.36), 1.23 (0.43), and 1.00 mm (0.33) in the LL, RL, and CW ROIs, respectively. The values from the IASs for the same ROIs trended higher 1.40 (0.42), 1.35 (0.51), and 1.05 mm (0.31) but only the LL ROI averaged over all phases showed significantly higher values than those of sorted CASs. Within each study, individual phases and ROIs showed significant differences between the average displacements of the CAS and IAS, with the IAS values being larger. Additionally, within some phase bins, the average distance (magnitude of the difference) of the RPM amplitude values from the center of the phase bin into which they were sorted was greater for sorted IAS volumes than sorted CAS volumes. Table 2-2 summarizes the abovementioned significant differences according to study, ROI, and respiratory phases.

Table 2-2: Summary of magnitude of displacement respiratory phase binning results

Study	Phases Showing Significant Differences			
	ROI			RPM
	Right Lung	Left Lung	Chest Wall	
A1	3,5	1,3		1,5
A2				1
A3	5	5	5,7,8	
B1	5	1,5	5	5
B2	4,5	5	5	5
B3			3	1
C1				5,6
C2				
C3				1
D1	5	5		
D2	4	3,4	5	
D3		5		7

bold indicated phases where the RPM values showed no significant difference



2.3.2 Linear Correlation Experiment

The slopes and intercepts obtained from the linear regressions between the magnitude of the displacement vector fields of the CAS_{12} and IAS_{12} volumes with respect to the RS_{12} maximum expiration volume and the RPM amplitudes showed significant differences between the CAS and the IAS volumes. The slopes of the regression were found to be significantly different between CAS and IAS volumes in 6/12, 10/12, and 4/12 studies in the RL, LL, and CW ROI, respectively. The intercept showed significant differences in 3/12, 6/12 and 4/12 studies for the same ROIs. Table 2-3 shows a summary of the results of the linear regression analyses. Of note, the standard deviations of the slopes and intercepts of the CAS regression analyses were always smaller than those of the IAS regression analyses, indicating a more stable linear relationship. Table 2-4 shows the Pearson correlation values of the linear regressions for all three regions of

interest. There were a total of six instances (combination of study and ROI) that showed significant differences between the CAS and IAS ($p < 0.01$). Of note, however, in all of these cases the Pearson correlation value was greater than 0.891. The Pearson values for all 12 studies did not fall below a value of 0.763, which denotes a significant correlation at the $p < 0.01$ level. The average Pearson value over all the studies was extremely high (0.947 ± 0.074 for CAS and 0.939 ± 0.060 for IAS) for all regions of interest. Figure 2-6 shows plots of the regression lines from all CAS (figure 2-6a) and IAS (figure 2-6b) in study B2, along with the mean and 95% confidence interval lines.³⁵ The regression lines from the CAS (figure 2-6a) display a tighter confidence interval and few deviations from the mean line than the regression lines from the IAS (figure 2-6b).

Table 2-3: Linear correlation results. Summary of the results from the linear correlation analysis of the motions of an external marker and internal anatomy. Asterisks indicate a significant difference ($p < 0.05$) in the slope or the intercept between the consistent and inconsistent amplitude regressions.

Study	Right Lung		Left Lung		Chest Wall	
	Slope	Intercept	Slope	Intercept	Slope	Intercept
A1		*	*			
A2	*		*			
A3			*	*		
B1			*	*	*	*
B2	*	*	*	*	*	*
B3						
C1			*			
C2	*		*	*	*	*
C3	*		*	*		
D1						
D2	*		*			
D3	*	*	*	*	*	*
Totals	6	3	10	6	4	4

* - significant difference between regular and irregular bcs ($p < 0.05$)

Table 2-4: Summary of Pearson correlation coefficients

	Right Lung ROI				Left Lung ROI				Chest Wall ROI			
	Consistent		Inconsistent		Consistent		Inconsistent		Consistent		Inconsistent	
	Value	+/- SD	Value	+/- SD	Value	+/- SD	Value	+/- SD	Value	+/- SD	Value	+/- SD
A1	0.891 +/- 0.047	* 0.032	0.963 +/- 0.032	0.033	0.923 +/- 0.033	* 0.019	0.971 +/- 0.019	0.954 +/- 0.040	0.967 +/- 0.017	0.981 +/- 0.009	0.012	0.980 +/- 0.020
A2	0.982 +/- 0.009	0.005	0.984 +/- 0.012	0.006	0.986 +/- 0.006	0.007	0.988 +/- 0.007	0.981 +/- 0.012	0.980 +/- 0.020	0.976 +/- 0.009	*	0.914 +/- 0.072
A3	0.991 +/- 0.005	0.003	0.980 +/- 0.019	0.019	0.977 +/- 0.008	0.015	0.974 +/- 0.015	0.983 +/- 0.009	0.921 +/- 0.059	0.986 +/- 0.010	*	0.937 +/- 0.072
B1	0.992 +/- 0.003	0.014	0.974 +/- 0.025	0.025	0.949 +/- 0.017	0.036	0.939 +/- 0.036	0.982 +/- 0.010	0.987 +/- 0.008	0.983 +/- 0.009	0.009	0.983 +/- 0.009
B2	0.963 +/- 0.014	0.008	0.818 +/- 0.242	0.242	0.955 +/- 0.015	0.028	0.951 +/- 0.028	0.982 +/- 0.010	0.987 +/- 0.008	0.986 +/- 0.010	*	0.937 +/- 0.072
B3	0.983 +/- 0.008	0.017	0.981 +/- 0.022	0.022	0.959 +/- 0.014	0.039	0.969 +/- 0.039	0.978 +/- 0.009	0.977 +/- 0.012	0.974 +/- 0.013	0.013	0.975 +/- 0.011
C1	0.983 +/- 0.017	0.020	0.992 +/- 0.003	0.003	0.986 +/- 0.011	0.004	0.992 +/- 0.004	0.978 +/- 0.009	0.977 +/- 0.012	0.763 +/- 0.095	0.095	0.795 +/- 0.086
C2	0.995 +/- 0.003	0.004	0.993 +/- 0.005	0.005	0.960 +/- 0.020	* 0.039	0.926 +/- 0.039	0.974 +/- 0.013	0.975 +/- 0.011	0.990 +/- 0.005	0.005	0.980 +/- 0.019
C3	0.955 +/- 0.020	0.009	0.949 +/- 0.025	0.025	0.960 +/- 0.012	0.024	0.951 +/- 0.024	0.803 +/- 0.075	0.850 +/- 0.110	0.979 +/- 0.007	0.007	0.981 +/- 0.006
D1	0.992 +/- 0.004	0.009	0.986 +/- 0.009	0.009	0.973 +/- 0.011	0.012	0.968 +/- 0.012	0.990 +/- 0.005	0.980 +/- 0.019	0.990 +/- 0.005	0.005	0.980 +/- 0.019
D2	0.948 +/- 0.025	0.021	0.919 +/- 0.067	0.067	0.832 +/- 0.069	0.134	0.810 +/- 0.134	0.803 +/- 0.075	0.850 +/- 0.110	0.979 +/- 0.007	0.007	0.981 +/- 0.006
D3	0.993 +/- 0.005	0.030	0.982 +/- 0.021	0.021	0.992 +/- 0.005	0.011	0.987 +/- 0.011	0.979 +/- 0.007	0.981 +/- 0.006	0.946 +/- 0.077	0.077	0.939 +/- 0.061
Average	0.972 +/- 0.030	0.049	0.960 +/- 0.049	0.049	0.954 +/- 0.043	0.049	0.952 +/- 0.049	0.946 +/- 0.077	0.939 +/- 0.061	0.946 +/- 0.077	0.077	0.939 +/- 0.061

* significant difference between the consistent and inconsistent data with $p < 0.05$
All values exhibit a significant linear correlation at the $p = 0.01$ level

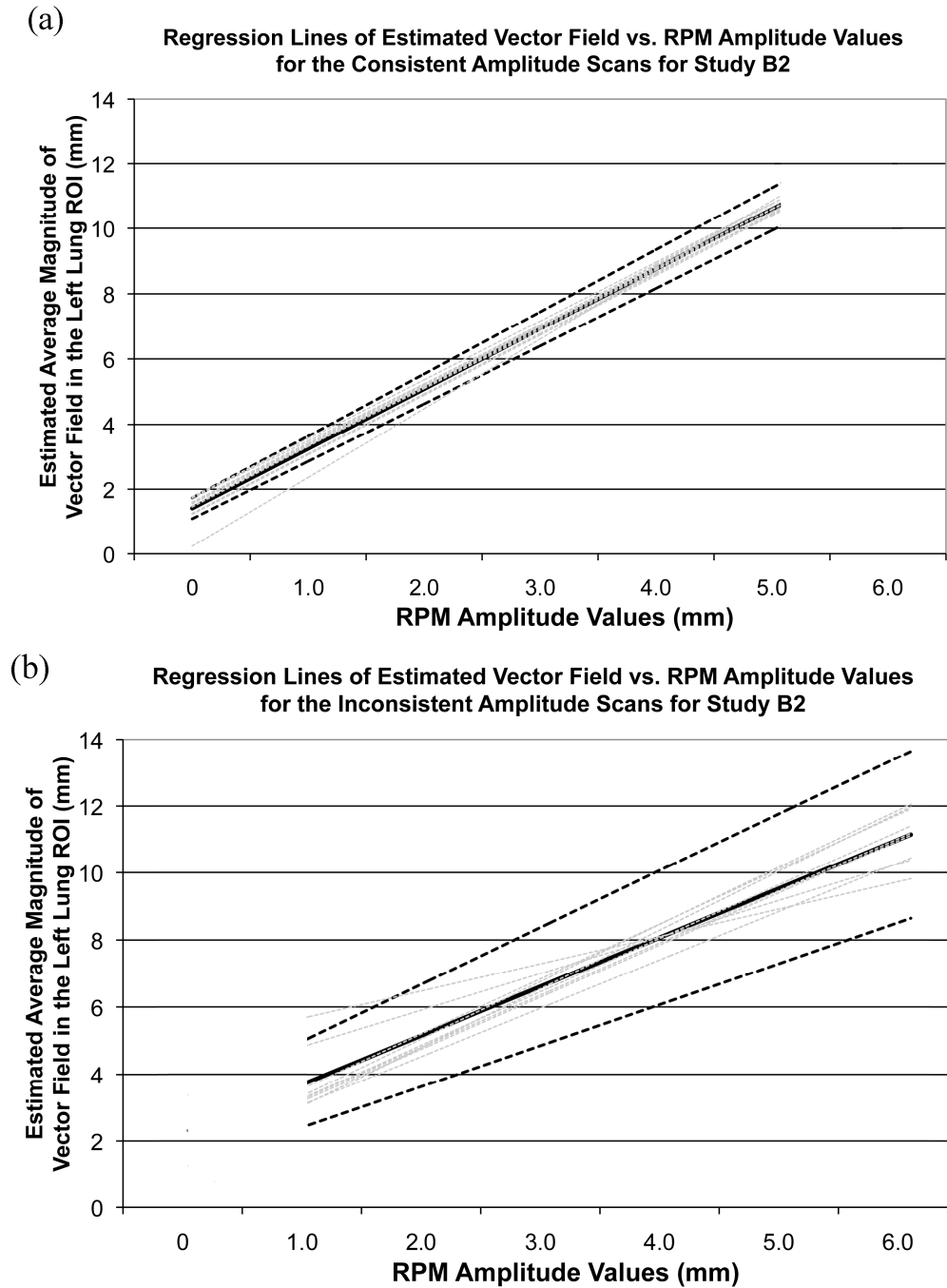


Figure 2-6: Regression results from inconsistent breathing cycles plot of the regression analysis results from Study B2. Shown are the individual regression lines (gray) between motions of an external marker and internal anatomy. The mean of the lines (black) and the 95% confidence interval for data collected during (a) consistent amplitudes & (b) inconsistent amplitudes are shown.

2.4 Discussion

A respiratory surrogate (e.g., the RPM system) must accurately predict the 3D motion of internal anatomy for it to be used confidently to gate radiotherapy and to limit artifacts in 4D-CT scans sorted with the help of the surrogate. In the current study, we tested how the magnitude of the anatomical displacement relative to a reference volume was affected by the inconsistent amplitude of breathing for volumes with the same RPM amplitude value. It was found that over the course of 12 studies, images collected during scans with inconsistent breathing amplitudes had a significantly greater displacements within the left lung of the animal. The left lung was most affected due to the right lateral recumbent position during scans. It was found that within each study, IAS volumes had significantly more anatomical displacements with respect to the reference volume than CAS volumes at a number of respiratory phases. The increase in magnitude of displacement occurred in phases at which the RPM amplitude is both significantly different (table 2-2 nonbold phases) or not different (table 2-2 bold phases) between the CASs and IASs. As such, the increase in deformation cannot be entirely attributed to difference in RPM amplitude between the sorted CASs and IASs. This result calls into question the ability of the one-dimensional motion of a single marker (e.g., the RPM amplitude curve) to accurately predict the full motion of a viscoelastic system such as the lungs, specifically when the amplitude of breathing is inconsistent.

We correlated the motion of the external RPM marker and the motion of ROIs defined within the thorax and chest wall by linear regression. The slope of the regression line indicate the ratio of motion of the external marker to that of the anatomy. We found in our studies that the linear correlations between the RPM amplitude curve and motion

of the internal anatomy were significantly correlated on a cycle by cycle basis (Pearson correlation coefficients for all studies > 0.763). However, there were significant differences in the slopes and intercepts of the regression lines between the consistent amplitude scans and the inconsistent amplitude scans. These results indicate that the same linear relationship between the motions of the external RPM marker and the internal anatomy was not preserved in the presence of inconsistent breathing amplitudes, but was restored when consistent breathing amplitudes returned.

Our study is one among several that compared the motion of an external marker to that of either internal anatomy or implanted fiducials. *Vedam et al.*²⁶ compared the motions of an optically tracked external marker to fluoroscopically acquired diaphragmatic motion. Similarly, *Korreman et al.*²³ compared motions of an external marker and fluoroscopically tracked implanted fiducials over a number of breath cycles. *Koch et al.*²² performed correlation analysis of motions measured using MRI images of a lung vessel and a skin marker over more than one breathing cycle. All of these studies used patients that exhibited some signs of irregular breathing during the studies. The correlation between the external marker and the internal anatomy showed varied results: Vedam found a high degree of correlation, Korreman found correlations to be good with some patients and poor with others, while Koch found that the correlation could depend on which structure in the lung was compared to the external marker. We showed, as did these studies, that there is a linear correlation between the motion of an external marker and the internal anatomy; our study extends the results of these prior works by sorting breath cycles according to the consistency of the breathing cycle amplitude and compared groups with highly variable amplitudes to ones having steady amplitudes. Our results

further support the need for breath coaching to train the patient to have a consistent breathing cycle over the course of the treatment. It has been well documented that there may be a variable relationship between the external marker and the internal anatomy in free breathing patients. As a result, a number of groups have developed adaptive external marker internal anatomy prediction algorithms to account for the changed relationship due to irregularities in patient breathing (*Ionascu et al.*³⁶ and *Kanoulas et al.*³⁷). The external marker curves shown in these two papers exhibit amplitude inconsistencies similar to the ones we have induced in our studies. In our work, we observed that the relationship between the external marker and internal anatomy changed only during the inconsistent amplitude scans. If this observation is repeated in patients, a method of continually changing the tumor-external marker correlation model throughout the treatment would be unnecessary. Instead, an alternative method may be to develop a procedure to recognize deviations from a consistent maximum amplitude of breathing in real time, by looking for high slope values or changes to the Fourier transform frequency spectrum of the RPM trace. This method could be used to pause or stall the radiation treatment at the onset of inconsistent breathing amplitudes and resume treatment when the breathing cycle has returned to the consistent pattern.

In this study, we changed the ventilator back pressure as a method to induce inconsistent breathing amplitudes. While inconsistent breathing amplitudes are not the only component of irregular breathing, it is one of the most important components if amplitude based 4D-CT is used for treatment planning or amplitude based respiratory gating is to be used to treat patients. The pig model presented in this study provides an *in-vivo* viscoelastic model to investigate how lung tissue, along with the chest wall, is

affected by highly variable breathing amplitudes. A further expansion on this study would be to use a programmable ventilator along with actual patient breathing curves to simulate both inconsistent breathing amplitudes and inconsistent breathing period lengths.

The method we have developed in the porcine model for the analysis of motions of internal anatomy during consistent and inconsistent breathing amplitudes as well as their comparison with motion of the RPM marker can be applied to human studies with minimal modifications. The radiation dose of the study would have to be significantly reduced below the current level of 20 mSv possibly by using iterative reconstruction algorithms (e.g., ASIR³⁸) and collecting fewer breathing cycles. Such human studies will verify whether the results obtained in our porcine model apply to human lungs.

The noise in the images used in this study approximately equivalent to the noise of images acquired during clinical 4D-CT studies. The tube current values used in this study are 2.5 times higher than a clinical study (200 mA vs. 80 mA), while the slice thickness used in this study is 4 times smaller (0.625 mm vs. 2.5 mm) than in a clinical study. The difference of these two values leads to a decrease in noise by 1.58 times and an increase in noise of 2 times, respectively, resulting in a total increase in noise of 26%. This slightly larger noise value is also decreased because the diameter of the pigs used in this study are smaller than the diameter of a human patient. Therefore, the noise between these two studies is approximately equivalent.*

* This paragraph did not appear in the original published paper. It was requested as an additional by one of the PhD examiners.

2.5 References

1. Engelsman, M., et al., *The effect of breathing and set-up errors on the cumulative dose to a lung tumor*. Radiotherapy and oncology : journal of the European Society for Therapeutic Radiology and Oncology, 2001. **60**: p. 95-105.
2. Lujan, A., E. Larsen, and J.M. Balter, *A method for incorporating organ motion due to breathing into 3D dose calculations*. Medical physics, 1999: p. 715-720.
3. Ozhasoglu, C. and M.J. Murphy, *Issues in respiratory motion compensation during external-beam radiotherapy*. Int J Radiat Oncol Biol Phys, 2002. **52**(5): p. 1389-99.
4. Shimizu, S., et al., *Impact of respiratory movement on the computed tomographic images of small lung tumors in three-dimensional (3D) radiotherapy*. International journal of radiation oncology, biology, physics, 2000. **46**: p. 1127-33.
5. Shirato, H., et al., *Intrafractional tumor motion: lung and liver*. Seminars in radiation oncology, 2004. **14**: p. 10-8.
6. Belderbos, J., et al., *Final results of a Phase I/II dose escalation trial in non-small-cell lung cancer using three-dimensional conformal radiotherapy*. International journal of radiation oncology, biology, physics, 2006. **66**: p. 126-34.
7. Bradley, J.D., et al., *Toxicity and outcome results of RTOG 9311: a phase I-II dose-escalation study using three-dimensional conformal radiotherapy in patients with inoperable non-small-cell lung carcinoma*. International journal of radiation oncology, biology, physics, 2005. **61**: p. 318-28.
8. Ford, E.C., et al., *Evaluation of respiratory movement during gated radiotherapy using film and electronic portal imaging*. International journal of radiation oncology, biology, physics, 2002. **52**: p. 522-31.
9. Hayman, J.a., M.K. Martel, and R.T. Haken, *Dose escalation in non-small-cell lung cancer using three-dimensional conformal radiation therapy: Update of a phase I trial*. Journal of Clinical, 2001. **19**: p. 127-136.
10. Underberg, R.W.M., et al., *Four-dimensional CT scans for treatment planning in stereotactic radiotherapy for stage I lung cancer*. International journal of radiation oncology, biology, physics, 2004. **60**: p. 1283-90.
11. Jin, J., et al., *Impact of fraction size on lung radiation toxicity: hypofractionation may be beneficial in dose escalation of radiotherapy for lung cancers*. Journal of Radiation, 2010.

12. Graham, M.V., et al., *Clinical dose-volume histogram analysis for pneumonitis after 3D treatment for non-small cell lung cancer (NSCLC)*. International journal of radiation oncology, biology, physics, 1999. **45**: p. 323-9.
13. Hernando, M.L., et al., *Radiation-induced pulmonary toxicity: a dose-volume histogram analysis in 201 patients with lung cancer*. International journal of radiation oncology, biology, physics, 2001. **51**: p. 650-9.
14. Ramella, S., et al., *Adding ipsilateral V20 and V30 to conventional dosimetric constraints predicts radiation pneumonitis in stage IIIA-B NSCLC treated with combined-modality therapy*. International journal of radiation oncology, biology, physics, 2010. **76**: p. 110-5.
15. Ruan, D., J.a. Fessler, and J.M. Balter, *Mean position tracking of respiratory motion*. Medical Physics, 2008. **35**: p. 782.
16. van Sörnsen de Koste, J.R., et al., *Verifying 4D gated radiotherapy using time-integrated electronic portal imaging: a phantom and clinical study*. Radiation oncology (London, England), 2007. **2**: p. 32.
17. Yorke, E., et al., *Interfractional anatomic variation in patients treated with respiration-gated radiotherapy*. Journal of applied clinical medical physics / American College of Medical Physics, 2005. **6**: p. 19-32.
18. Ahmed, R.S., et al., *Intensity modulation with respiratory gating for radiotherapy of the pleural space*. Medical dosimetry : official journal of the American Association of Medical Dosimetrists, 2007. **32**: p. 16-22.
19. Beddar, a.S., et al., *Correlation between internal fiducial tumor motion and external marker motion for liver tumors imaged with 4D-CT*. International journal of radiation oncology, biology, physics, 2007. **67**: p. 630-8.
20. Gaede, S., et al., *The use of CT density changes at internal tissue interfaces to correlate internal organ motion with an external surrogate*. Physics in medicine and biology, 2009. **54**: p. 259-73.
21. Killoran, J.H., et al., *Inter fractional variability of breathing phase definition as determined by fiducial location*. Medical Physics, 2008. **35**: p. 753.
22. Koch, N., et al., *Evaluation of internal lung motion for respiratory-gated radiotherapy using MRI: Part I--correlating internal lung motion with skin fiducial motion*. International journal of radiation oncology, biology, physics, 2004. **60**: p. 1459-72.
23. Korreman, S.S., et al., *Comparison of respiratory surrogates for gated lung radiotherapy without internal fiducials*. Acta oncologica (Stockholm, Sweden), 2006. **45**: p. 935-42.

24. Mageras, G.S., et al., *Fluoroscopic evaluation of diaphragmatic motion reduction with a respiratory gated radiotherapy system*. Journal of applied clinical medical physics / American College of Medical Physics, 2001. **2**: p. 191-200.
25. Spoelstra, F.O.B., et al., *Analysis of reproducibility of respiration-triggered gated radiotherapy for lung tumors*. Radiotherapy and oncology : journal of the European Society for Therapeutic Radiology and Oncology, 2008. **87**: p. 59-64.
26. Vedam, S.S., et al., *Quantifying the predictability of diaphragm motion during respiration with a noninvasive external marker*. Med Phys, 2003. **30**(4): p. 505-13.
27. Park, K., et al., *Do maximum intensity projection images truly capture tumor motion?* International journal of radiation oncology, biology, physics, 2009. **73**: p. 618-25.
28. Simon, L., et al., *Initial evaluation of a four-dimensional computed tomography system using a programmable motor*. Journal of applied clinical medical physics / American College of Medical Physics, 2006. **7**: p. 50-65.
29. Dinkel, J., et al., *Four-dimensional multislice helical CT of the lung: qualitative comparison of retrospectively gated and static images in an ex-vivo system*. Radiother Oncol, 2007. **85**(2): p. 215-22.
30. Serban, M., et al., *A deformable phantom for 4D radiotherapy verification: Design and image registration evaluation*. Medical physics, 2008: p. 1094-1102.
31. Lu, W., et al., *A comparison between amplitude sorting and phase-angle sorting using external respiratory measurement for 4D CT*. Medical Physics, 2006. **33**: p. 2964.
32. Starreveld, Y.P., *Fast nonlinear registration applied to stereotactic functional neurosurgery*. 2002, University of Western Ontario: London.
33. Nelder, J., *A simplex method for function minimization*. The computer journal, 1965.
34. Castillo, R., E. Castillo, and R. Guerra, *A framework for evaluation of deformable image registration spatial accuracy using large landmark point sets*. Physics in Medicine, 2009. **54**: p. 1849-1870.
35. Ewing, J., et al., *Direct comparison of local cerebral blood flow rates measured by MRI arterial spin-tagging and quantitative autoradiography in a rat model of experimental cerebral*. of Cerebral Blood Flow, 2003: p. 198-209.
36. Ionascu, D., et al., *Internal-external correlation investigations of respiratory induced motion of lung tumors*. Medical Physics, 2007. **34**: p. 3893.

37. Kanoulas, E., et al., *Derivation of the tumor position from external respiratory surrogates with periodical updating of the internal/external correlation*. Phys Med Biol, 2007. **52**(17): p. 5443-56.
38. Silva, A.C., et al., *Innovations in CT dose reduction strategy: application of the adaptive statistical iterative reconstruction algorithm*. AJR. American journal of roentgenology, 2010. **194**: p. 191-9.

Chapter 3

The development of an automated image based 4D-CT sorting algorithm

3.1 Introduction

Tumour movement due to respiration can adversely affect the planning and delivery of radiation treatment to lung cancers.¹⁻⁶ In an attempt to better treat these tumours some clinical centres have adjusted their treatment plans in response to respiratory motion.⁷⁻¹⁴ While some centres attempt to respiratory gate the tumour motion,^{15, 16} others attempt to adjust the treatment planning margins in response to the maximum excursion of the tumour at inspiration and expiration.¹⁷ 4-Dimensional Computed Tomography (4D-CT) imaging has been developed to visualize the tumor motion throughout the respiratory cycle.¹⁸⁻²⁴ Visualization of the tumour is required to provide a patient specific treatment plan for both respiratory gated and non-respiratory gated treatment.

Current methods to produce 4D-CT images require a surrogate respiratory signal from either a chest height marker (e.g., the Varian Real-time Position Management (RPM) System (Varian Oncology System, Palo, Alto, CA))^{18, 19, 21-23}, a strain gauge²⁴ or spirometer.²⁰ Volumes are produced by sorting images using the phase^{19, 22, 23} or the amplitude^{18, 20, 21, 24} of the surrogate signal. However, 4D-CT imaging sorting methods that are dependent upon an external respiratory signal are prone to artifacts due to non-reproducible breathing.^{25, 26} Published methods that adjust the sorting for non-

reproducible breathing include breath coaching using audio/visual feedback,^{27, 28} the use of non-rigid registration,^{25, 29, 30} and retrospective selection of the peak and valley positions of the respiratory waveform.^{26, 31, 32} In addition, recent independent studies by *Lu et al.*³³ and *Abdelmour et al.*³⁴ demonstrate a decrease in these breathing artifacts when using amplitude sorting.

In the wake of using surrogate respiratory signals to sort 4D-CT datasets, the relationship between the surrogate respiratory signal (obtained at one location of the abdomen) and the motion at other positions of the chest has been the subject of investigations. *Ozhasoglu and Murphy*⁴ found spatial and temporal misalignments between the motion of the chest and the motion of the abdomen. More importantly, no definitive relationship between the 3D motion of a tumour and the linear motion of an external marker was found. A more recent study³⁵ demonstrated phase shifts between the chest wall motion and motion of an external marker placed on the abdomen. In addition, hybrid gating has been recently developed to overcome the non-linear relationship between the tumour and the external marker.³⁶ These studies indicate that respiratory motion recorded with a single abdominal marker cannot accurately represent the motion of the chest or the highly complex 3D tumour motion.

Recent studies have attempted to align respiratory states without the use of an external respiratory surrogate. *Hope et al.*³⁷ presented an algorithm that automatically sorted ciné time series images according to respiratory phase to produce 4D-CT images. However, it is unknown how well the algorithm handles non-reproducible breathing patterns. A recently published lung model registration method²⁹ based upon an internal respiratory surrogate and non-rigid registration produced good results for 3 out of a total

of 5 patients. In addition, *Eck et al.*³⁸ showed normalized cross correlation (NCC) to be a useful metric to match the respiratory phase of the CT images based on image similarity.

In this work, a new fully automated sorting algorithm that uses NCC to determine CT volumes and produce 4D-CT images is presented. The method does not require an external respiratory signal and performs well in the presence of non-reproducible breathing. The new automated method is compared to published amplitude and phase angle sorting methods that are currently in clinical use. The comparison shows our method to perform well in comparison to the methods that use the external respiratory surrogate. In addition, our method produces 4D-CT images free of inter-slice “banding” artifacts that can result in erroneous estimates of tumour volume.

3.2 Methods

Patients were scanned using a 4-slice CT scanner (Discovery LS, General Electric Healthcare Technologies, Waukesha, WI) operating in axial ciné mode. The amplitude of the respiratory motion was monitored using the Varian RPM system with the tracking block placed on the abdomen. The phase angle respiratory curve was calculated from the measured amplitude respiratory curve using the Varian RPM software (ver. 1.6). The respiratory trace was synchronized to the CT image acquisition via a TTL (transistor-transistor logic) signal provided by the CT scanner when the x-rays were on. The patients were allowed to breath freely with no prior breath coaching. The Health Sciences Research Ethics Board of the University of Western Ontario, Canada approved the study procedures. All participating patients gave informed consent for the study.

3.2.1 Image Data Acquisition

3.2.1.1 Scan Parameters

The patients' breathing cycle was monitored prior to scanning, using the RPM system, to determine their average breathing periods. The scanning protocol consisted of a series of asynchronously acquired serial ciné scans, acquired at different scan positions, to cover the entire thorax of a patient. At each ciné scan position, time series of images were acquired for a interval corresponding to the average breathing period plus an addition second to account for possible breathing period variations. The addition of one second was chosen because it has been shown that the standard deviation of the breathing cycle length is rarely greater than 1.0 seconds.⁹ Between two successive ciné scans the couch was translated 3/4 of the axial field of view to the next scan position. This modified translation resulted in a common (overlapping) slice between adjacent ciné scans. Typically, between 20 and 30 translations were needed to cover the entire thorax. The CT scanning parameters were: 0.5 second gantry rotation, four \times 2.5 mm thick slices, 120 kVp and 80 mA. The reduced tube current provided dose savings to the patient. Total scan times were between 2 and 3 minutes for the entire thorax.

3.2.1.2 Definition of Image Data

From each ciné scan, four time series of images, one for each of the four slices, were retrospectively reconstructed at a time spacing of 0.1 seconds. In total, each study resulted in a maximum of 6000 images. Here we develop nomenclature to index each axial image, $I(x, y)$. Each image is indexed by n : the scan position of the ciné scan; s :

the image location within the scan position, and t : the time index within a time series (figure 3-1). The resulting indexed images are represented by:

$$I(n, s)_t = I(x, y) \quad \forall x, y \in [1, 512]; n \in [1, N]; s \in [1, S]; t \in [1, T] \quad (3.1)$$

where, N is the total number of positions scanned; S , the number of image locations, is equal to 4 for a 4 slice scanner; T is the total number of images in a time series. For fixed n and s the entire time series of image is defined as:

$$\tilde{I}(n, s) = I(n, s)_t \quad \forall t \in [1, T] \quad (3.1a)$$

The physical location of any image along the axial direction of the scanner (z axis) is a function of scan position and image location, n and s :

$$z = f_z(n, s) \quad (3.2)$$

where, $f_z(1, 1)$ corresponds to the most inferior slice position.

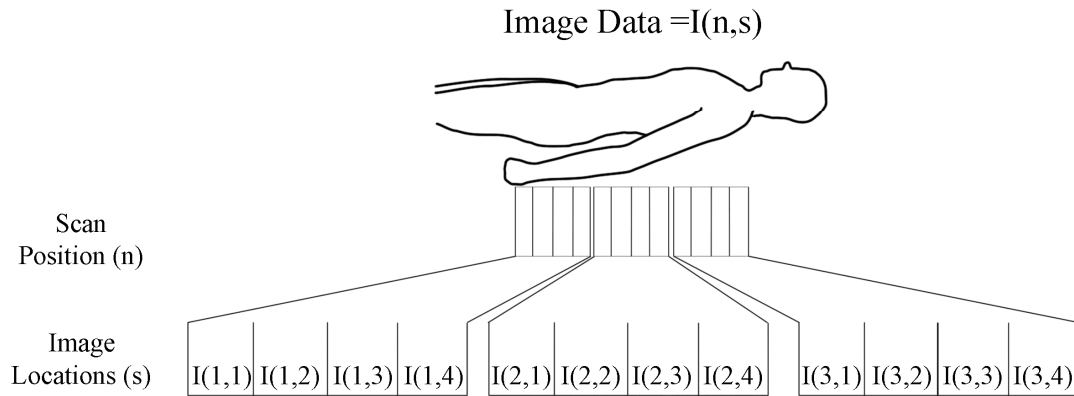


Figure 3-1: A diagram illustrating the definition of scan position (n) and image position (s) within the image data $I(n,s)$. The top diagram outlines the orientation of a patient. The middle diagram shows the scan position blocks. The lower diagram shows the slices within the scan positions, labeled according to n and s .

The overlapping scanning protocol, described in 3.1.1 Scanning Parameters, results in overlapping images between adjacent scan positions. Specifically, the location of the most superior image of scan position (n) has the same physical location as the most inferior image of scan position $n+1$:

$$f_z(n, s = 4) = f_z(n + 1, s = 1) \quad (3.3)$$

such that,

$$\tilde{I}(n,1) \text{ and } \tilde{I}(n-1,4) \quad (3.3a)$$

$$\tilde{I}(n,4) \text{ and } \tilde{I}(n+1,1) \quad (3.3b)$$

are time series of images from overlapping image positions. Each scan position, with exception of the most inferior and most superior, has two overlapping time series of images. The most superior and inferior scan positions each have only one overlapping time series of images.

The image time, in seconds, is related to the image time index, t , by:

$$\text{Image Time} = \Delta t \times t \quad (3.4)$$

where Δt is the reconstruction time increment in seconds. In this study the time increment (Δt) is 0.1 seconds.

3.2.2 4D-CT Methods

To compare RPM sorting algorithms with image based NCC sorting algorithms, both algorithms were used in the study and they are described in the following sections.

3.2.2.1 RPM Sorting Algorithms

Sorting algorithms using the RPM respiratory curve have been previously published.^{18, 19, 21-23} Briefly, a respiratory curve that is synchronized to the image acquisition is collected by the RPM system. The system employs a CCD camera that captures the motion of an external marker placed on the skin surface of the thorax/abdomen. Each image is assigned either an amplitude or phase value derived from the RPM curve. Using the synchronized values the images are sorted into respiratory (phase) ‘bins’ (usually between 8 and 12). Combining images contained within each bin produces a time series of spatially coherent volumes.

Amplitude-Based Algorithm

Each acquired image is indexed by a respiratory amplitude value from the RPM curve and the sign of the first derivative of the RPM curve. The sign of derivative index determines whether the images were collected during inspiration or expiration. Respiratory bins are constructed by dividing the interval between the global maximum and the global minimum of the RPM amplitude curve into two sets of 8 equally spaced subintervals: one set for inspiration and one set for expiration. Images are sorted into appropriate respiratory bins according to the two indices and then all the images in a bin are grouped together to form a 3D volume. The final 4D-CT dataset is comprised of a 3D volume from each respiratory bin. However, variations of the patient's respiratory amplitude during image acquisition may result in some bins containing incomplete volumes. These incomplete volumes are excluded from the final 4D-CT datasets; as a result, not all of the 4D dataset necessarily had 16 3D volumes.

Phase-Based Algorithm

Images were indexed by a phase value between 0 and 2π radians from the phase angle curve calculated by the RPM software. Respiratory phase bins were constructed by dividing the interval of $[0, 2\pi]$ into 16 equal spaced subintervals. All the images were sorted into bins according to their phase index. As in the amplitude-based algorithm the 4D-CT dataset consisted of complete 3D volumes from each phase bin.

3.2.2.2 Image Matching Based on Normalized Cross Correlation

The Normalized Cross Correlation (NCC) coefficients between two 2D images is defined as:

$$NCC(I_A, I_B) = \frac{\sum_{x,y} (I_A(x,y) - \bar{I}_A)(I_B(x,y) - \bar{I}_B)}{\sqrt{\sum_{x,y} (I_A(x,y) - \bar{I}_A)^2 \sum_{x,y} (I_B(x,y) - \bar{I}_B)^2}} \quad (3.5)$$

where $I_A(x,y)$ and $I_B(x,y)$ are the pixel values at pixels x and y of images I_A and I_B respectively. \bar{I}_A and \bar{I}_B are the mean pixel values of images I_A and I_B . The NCC coefficient varies between a value of -1.0 and 1.0 ; a value of 1.0 corresponds to perfect image similarity.

The NCC 4D-CT sorting algorithm consists of 3 steps. First, the *Truncation and Shift* step reduces the number of images in each time series of images to a single breathing period of images and shifts the time series to begin at maximum expiration. Next, the *Volume Determination* step assigned all the image data to produce 3D volumes at each 4D-CT time point. Lastly, the *Optimization* step selects the optimum reference image scan position to reduce possible artifacts due to breathing cycle variations. The implementation of each step is described in detail below.

Step 1 –Truncation and Shift

The raw data consists of multiple time series of images acquired serially for a time period equal to the patient’s average breathing period plus an additional second. The first step of the NCC algorithm is to select a single breathing cycle of images from each time series of images. The breathing cycle length of a periodic time series of images (figure 3-2) can be determined by locating the image within the breathing cycle that is most similar to the first image. Using equation 3.5, the NCC coefficient is used as an image similarity metric:

$$NCC_{BC}[t] = NCC(I(n, s)_{t=1}, \tilde{I}(n, s)) \quad t \in [1, T] \quad (3.6)$$

where $\tilde{I}(n, s)$ is the time series of images at scan position n , and image position s ; $I(n, s)_{t=1}$ is the first image of the same series.

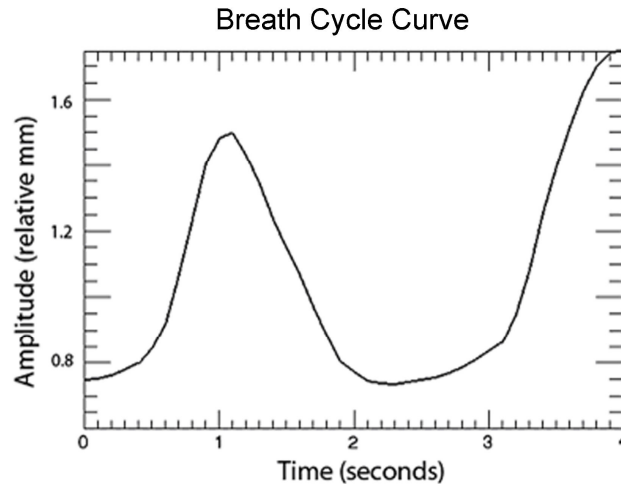


Figure 3-2: The curve shows a breath cycle curve of images from a cine time series generated by tracking the chest at a single point. The curve displays the breathing cycle’s periodicity.

The NCC coefficients, $NCC_{BC}[t]$, begin at a value of 1.0, decrease to a minimum and then return to a local maximum (figure 3-3). Assuming that each time series returns to its initial respiratory state the breath cycle duration is defined as the time index value associated with the local maximum of $NCC_{BC}[t]$ past the $T/2$ point:

$$T_{BC} = \max_t(NCC_{BC}[t]) \quad \text{where } t \geq \frac{T}{2} \quad (3.7)$$

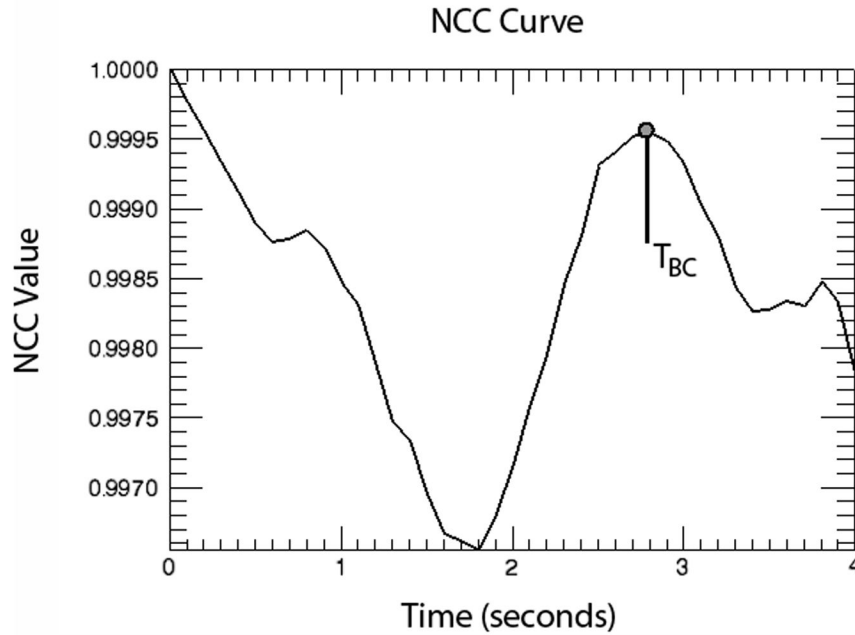


Figure 3-3: The curve displays the results of a NCC algorithm between the first image of a ciné time series and each subsequent image. The maximum past the half way mark is labeled T_{BC} and indicates the length of one breath cycle.

The time series of images is truncated to this point (figure 3-4) and the limits of t in equation 3.1 are changed to $t \in [1, T_{BC}]$. All slices within a scan position were scanned synchronously and have the same breathing cycle length. Therefore, T_{BC} is only a function of scan position ($T_{BC} = T_{BC}(n)$) and the value at scan of T_{BC} position n is set to the average value of the 4 time series of images within the scan position.

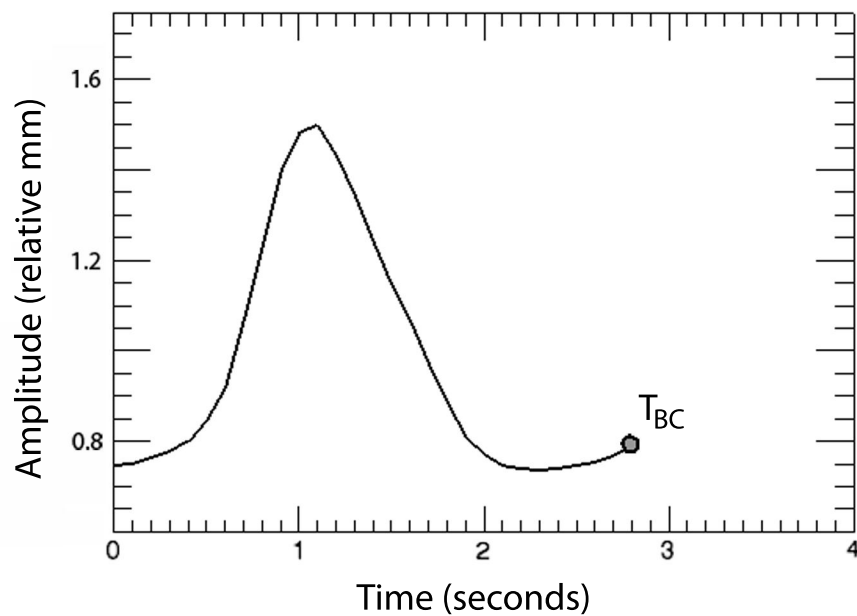


Figure 3-4: A plot of the breath cycle curve from figure 3-3 truncated to exactly one breath cycle.

In addition to truncating each time series of images to one breathing cycle each series must be shifted to begin at a specific respiratory phase. We chose to shift each time series to begin at maximum expiration and performed this step using an image derived chest height (CH). The CH is determined from a vertical profile of an axial

image (figure 3-5). The patient is assumed to be centered resulting in the first profile being taken from the midline of the image. The CH is defined as the first instance that the y -coordinate of the profile, in pixels, exceeds -400 HU. The final CH is the average of 40 CHs profiles (20 on either side of the first midline profile). After performing this operation for an entire time series of images, the time series is shifted until the image with the lowest CH (corresponding to maximum expiration) is the first image of the series. This was performed for every time series of images independently.

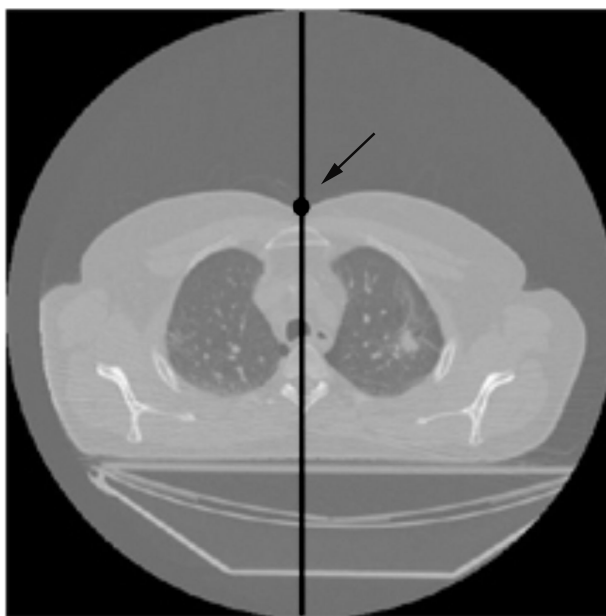


Figure 3-5: An axial CT image of the thorax; highlighted is the profile line and chest position.

Step 2 – Volume Determination

The second step in the algorithm assigns the data from the asynchronously acquired time series of images, which have been truncated and shifted, into coherent 3D volumes. The images are assigned to volumes that are indexed by a volume phase index value (m). Each volume has a set of reference images, from a single scan position, that are used as the basis for producing each volume. Images at scan positions adjacent to the reference images are assigned to a volume based upon the image similarity to the reference images. This process is continued using the assigned images as the reference images and assigning the images at next adjacent scan position. The process is continued in this "daisy chaining" fashion to determine an entire volume.

To begin, the reference images corresponding to a phase are selected by a image phase index value (p). The image phase index value is a time index value (t) that locates the reference images within a time series of images. Two variables determine the image phase index value: the volume phase index value of the desired volume (m) and the scan position of the reference images (n_R):

$$p_m(n_R) = m \times \frac{T_{BC}(n_R)}{M} \quad m \in [1, M] \text{ and } M \leq T_{BC}(n_R) \quad (3.8)$$

where M is the total number of 3D volumes in the final 4D-CT dataset; in this study $M = 16$.

Each final 3D volume is influenced by the scan position of the reference images. The problem of determining n_R is dealt with in *Step 3*. For simplicity in the rest of this

section, n_R is assumed to be a general scan position between $n = I$ and $n = N$, and the image phase index value, $p_m(n_R)$ is abbreviated to p_m .

Using equations 3.1 and 3.8 the reference images are determined from the appropriate time series of images:

$$I_R(n_R, s)_{t=p_m} = I(x, y)_{n_R, s, p_m} \quad \forall x, y \in [1, 512]; n_R \in [1, N]; s \in [1, S]; \quad (3.9)$$

$$p_m \in [1, T_{BC}(n_R)]; m \in [1, M]$$

Images for non-integer values of p_m are produced by linear interpolation of the neighbouring images:

$$I_R(n_R, s)_{t=p_m} = w_1 \bullet I(x, y)_{n_R, s, \text{ceil}(p_m)} + w_2 \bullet I(x, y)_{n_R, s, \text{floor}(p_m)} \quad (3.9a)$$

where $\text{floor}(p_m)$ is a function that rounds p_m to the first integer less than p_m , $\text{ceil}(p_m)$ is a function that rounds p_m to the first integer greater than p_m . The weighting factors are:

$$w_1 = p_m - \text{floor}(p_m) \quad (3.9b)$$

$$w_2 = \text{ceil}(p_m) - p_m$$

Once the reference images for a volume have been chosen we begin to assign images to that volume. The reference images possess two sets of overlapping slice positions, one at the inferior image position ($s = I$), one at the superior image position ($s = 4$). At each of these overlapping image positions the NCC is calculated between the reference images and the overlapping time series of images at the adjacent scan positions (n_R-1, n_R+1):

$$\begin{aligned}
NCC_{Inf,n_R-1}[t] &= NCC(I_R(n_R,1)_{t=p_m}, \tilde{I}(n_R-1,4)) \quad t \in [1, T_{BC}(n_R-1)] \\
\text{and} & \\
NCC_{Sup,n_R+1}[t] &= NCC(I_R(n_R,4)_{t=p_m}, \tilde{I}(n_R+1,1)) \quad t \in [1, T_{BC}(n_R+1)]
\end{aligned} \tag{3.10}$$

NCC_{Inf,n_R-1} and NCC_{Sup,n_R+1} are matching functions that contain the NCC coefficients as defined in equation 3.6. The maxima of these functions determine the time index values of the images at adjacent scan positions, n_R-1 and n_R+1 , that are most similar to the reference images. These matched images are assigned to the volume that is described by the reference images determined by the image phase index value, p_m .

To record the time index values of the volumes, a lookup table, $\tau(m,n)$, is generated. The first value added to the lookup table is the image phase index value, p_m , recorded at the reference scan position:

$$\tau(m, n_R) = p_m \tag{3.11}$$

After the first matching, as described by equation 3.10, the time index values of the first assigned images are also recorded:

$$\begin{aligned}
\tau(m, n_R - 1) &= \max_t(NCC_{Inf,n_R-1}[t]) \quad t \in [1, T_{BC}(n_R - 1)] \\
\text{and} & \\
\tau(m, n_R + 1) &= \max_t(NCC_{Sup,n_R+1}[t]) \quad t \in [1, T_{BC}(n_R + 1)]
\end{aligned} \tag{3.12}$$

As in equation 3.7, the $\max_t(\)$ function determines the time index value corresponding to the maximum of function argument. The next step in the algorithm uses the first assigned images, described by equation 3.12, to assign images from the next scan positions (i.e. n_R+2 and n_R-2) to the volume:

$$\begin{aligned}
NCC_{Inf,n_R-2}[t] &= NCC(I_R(n_R-1,1)_{t=\tau(m,n_R-1)}, \tilde{I}(n_R-2,4)) \quad t \in [1, T_{BC}(n_R-2)] \\
\text{and} & \\
NCC_{Sup,n_R+2}[t] &= NCC(I_R(n_R+1,4)_{t=\tau(m,n_R+1)}, \tilde{I}(n_R+2,1)) \quad t \in [1, T_{BC}(n_R+2)]
\end{aligned} \tag{3.13}$$

Again, the time index values of sorted images are recorded into the same bin of the lookup table $\tau(m, n)$:

$$\begin{aligned}
\tau(m, n_R-2) &= \max_t (NCC_{Inf,n_R-2}[t]) \quad t \in [1, T_{BC}(n_R-2)] \\
\text{and} & \\
\tau(m, n_R+2) &= \max_t (NCC_{Sup,n_R+2}[t]) \quad t \in [1, T_{BC}(n_R+2)]
\end{aligned} \tag{\pi}$$

The process continues in this "daisy chain" fashion to fill the entire lookup table at this volume phase index value. The physical direction in which the algorithm proceeds depends on the initial location of reference scan position. Three options exist: 1) the reference scan position is $I < n_R < N$ and the cascade proceeds in both the inferior (for $n = n_R$ to I) and in the superior directions (for $n = n_R$ to N); 2) the reference scan position is $n_R = I$ and the cascade proceeds in the superior direction ($n = I$ to N); and 3) the reference scan position is $n_R=N$ and the cascade proceeds in the inferior direction ($n = N$ to I). The matching algorithm for a single reference scan position is illustrated in figure 3-6.

The algorithm is repeated for all phases $m = [1, M]$. The final result of volume determination is described by the formula:

$$\tilde{I}(n, s)_m = \{I(x, y)_{n,s,\tau(m,n)}\} \quad \begin{aligned} &\forall x, y \in [1, 512]; \forall n \in [1, N]; \forall s \in [1, S-1]; \\ &m \in [1, M]; \tau(m, n) \in [1, T_{BC}(n)] \end{aligned} \tag{3.15}$$

where $s = [1, S-1]$ has been truncated by I to remove the overlapping image.

Step 3 - Volume Optimization

Step 2 defined an algorithm to assign asynchronously acquired serial ciné time series of images to a coherent 3D volume. Images are assigned according to a set of reference images, which are taken from one scan position (n_R) time series of images. Therefore, the entire 3D volume is based upon images collected at one particular scan position (n_R). However, breathing cycle variations during image acquisition may introduce artifacts due to a dependence of the algorithm on the location of the reference images. Therefore, an additional algorithm is required to select the location of n_R to optimize the spatially coherence of each volume.

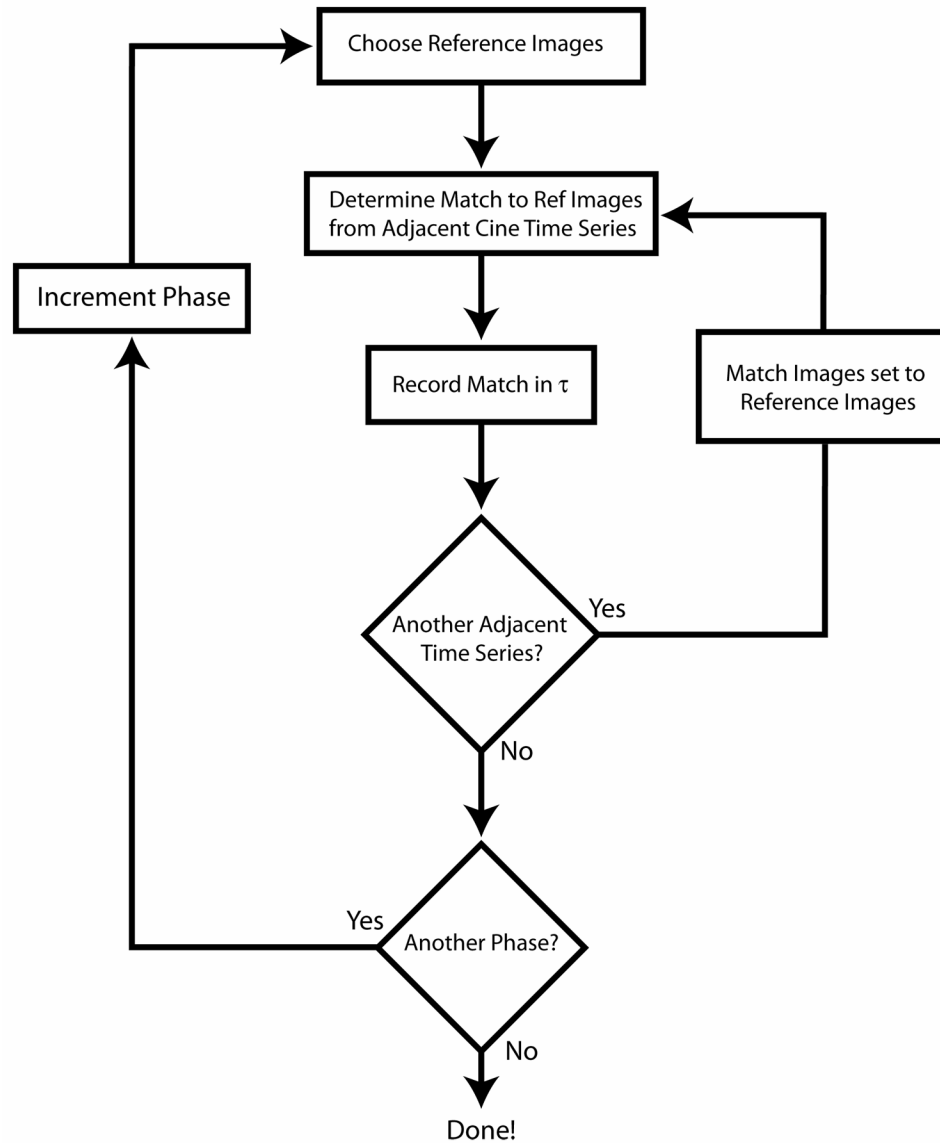


Figure 3-6: A diagram of the algorithm for a single reference scan position. The full algorithm makes use of multiple reference scan positions.

To begin, for a given volume phase index *Step 2 Volume Determination* is repeated 12 times using each of the 12 most inferior scan positions as the reference scan position, (i.e. $n_R = 1$ to 12). The result is 12 unique lookup table, $\tau(m, n)$. Each lookup

table provides a survey of possible 4D-CT volume sets. Each of the survey volume sets is based on different reference images collected during different breathing cycle periods.

The next step, for each set of 4D-CT volumes, is to determine which of the n_R values produces the most spatial coherent volume set. The NCC coefficient value, as a measure of image similarity, was chosen as the measure of the spatial coherence of a sorted volume. All volumes had $N-1$ (the total number of scan positions minus one) image matchings performed. Each matching resulted in an assigned image, with an associated NCC coefficient (equation 3.10). The measure of the spatial coherence of each volume is taken as the sum of the NCC coefficients from the all image matchings. The volume set with the highest sum was selected as the optimal 4D-CT volume set and the scan position, n_R , that produced this volume set, is selected as the optimal reference scan position. A comprehensive explanation for this procedure is available in the discussion.

3.2.3 Comparison and Analysis

The first analysis uses the root mean square deviation (RMSD) to measure the similarity between any image pair as follows:

$$RMSD(I_A, I_B) = \sqrt{\frac{\sum_{x,y} (I_A(x,y) - I_B(x,y))^2}{K}} \quad (3.16)$$

where K is the number of pixels in the images $I_A(x,y)$ and $I_B(x,y)$. $RMSD$ equals 0 if $I_A(x,y)$ and $I_B(x,y)$ are the identical.

For each registered 4D-CT dataset, we define a figure of merit (FOM) as:

$$FOM = \frac{1}{M(N-1)} \sum_M \sum_{N-1} RMSD(I(n,4)_m, I(n+1,1)_m) \quad (3.17)$$

where $I(n,p)_m$ refers to an image from one of the sorted 4D-CT volumes; $I(n,4)_m$ is the image from scan position n , and from the previously removed image position 4; $I(n+1,1)_m$ is the image from scan position n and from image position 1. The previously removed image position 4 is required to provide a comparison of the overlapping images. N is the number of scan positions in the volume and M is the number of phases.

One-way analysis of variance (ANOVA) with Tukey's post-hoc test is used to find significant differences between $FOMs$ from the RPM amplitude sorting method, the RPM phase angle sorting method and NCC sorting method.

In the second analysis we determined the RPM amplitude (and phase) curve value for each image of each volume determined using the NCC algorithm. For each full 3D volume a frequency distribution of these values was determined. The results are histograms of RPM respiratory amplitude (or phase) values from each image used to construct a volume, at each time point. The histograms evaluate the ability of the RPM system, which monitors the motion of an external marker at a single location on the surface of the thorax, to consistently predict the motion of the entire chest. A very narrow RPM respiratory amplitude (or phase) histogram from NCC sorted images indicates a high degree of correlation between the motion of the RPM external marker and the entire chest. Conversely, a wide histogram indicates a low degree of correlation between the motion of the RPM external marker and the entire chest. For comparison,

histograms were produced for volumes determined using both the RPM amplitude sorting method and the RPM phase angle sorting method.

3.3 Results

The RPM amplitude respiratory curve collected from one patient is plotted in figure 3-7. The maximum inspiration amplitude value varies over the course of the curve. Figure 3-8 shows an expanded view of the final four breathing periods and displays both the amplitude curve and corresponding phase angle curve that was calculated by the RPM software. While the maximum of the amplitude curve varies during these breathing cycles, the phase angle curve shows no such variations; cycling between 0 and 2π radians.

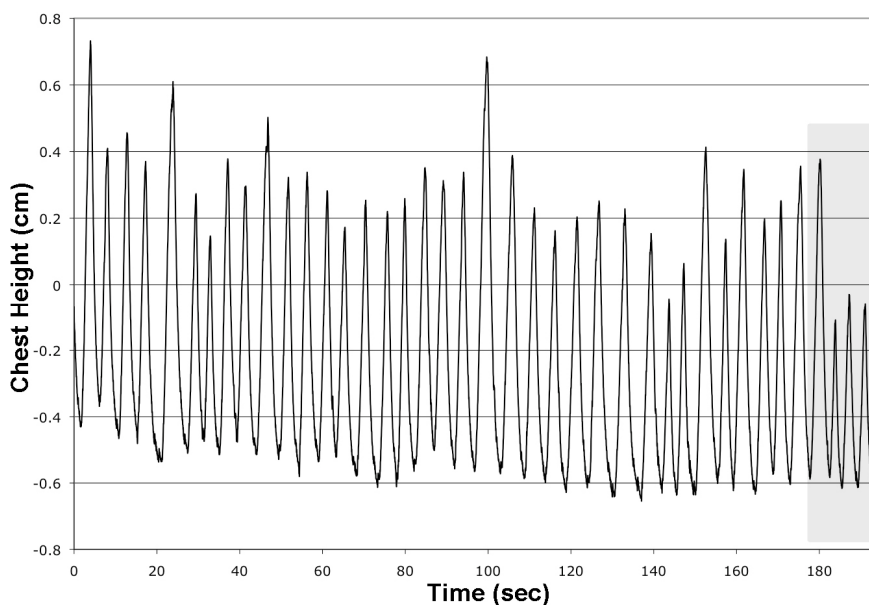


Figure 3-7: Patient RPM curve plot of the RPM amplitude curve for patient 3 collected during CT image acquisition. The highlighted portion is expanded in figure 3-8.

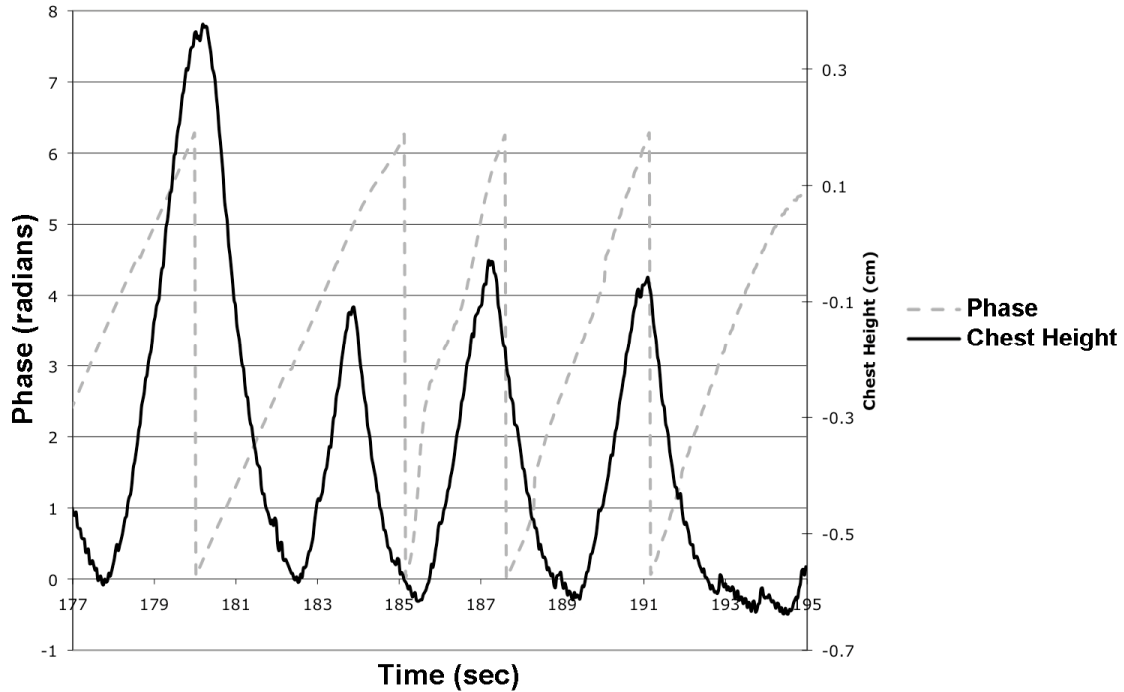


Figure 3-8: Highlighted end section from figure 3-7 is enhanced. The chest height data is plotted with the phase angle data calculated by the RPM software.

Reformatted coronal images of the registered 4D-CT datasets were examined for obvious inter-scan banding artifacts. In general, it was found that images from both RPM sorting methods yielded more artifacts than the NCC method. As well, in some cases the RPM phase angle method yielded more banding artifacts than the RPM amplitude method. Reformatted coronal images from one patient produced by the three different methods, for four phases of the breathing cycle, are shown in figure 3-9. The banding artifacts are prominently displayed at the diaphragm.

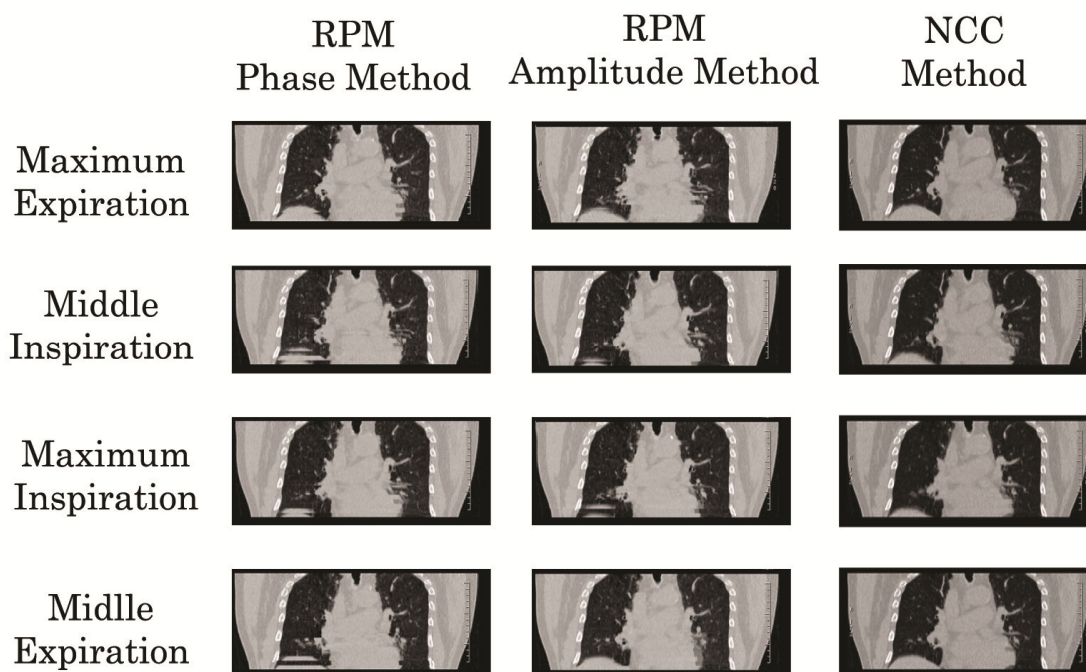


Figure 3-9: Reformatted coronal reconstruction at 4 phases of the breathing cycles using 3 different sorting methods. Images are from patient 2. Inter-slice artifacts are noticeable in both external marker methods.

The Figure of Merit (*FOM*) results are presented in figure 3-10. For all patients, the *FOM* of the NCC method was significantly lower (improved volumes, fewer artifacts) than those of both RPM sorting methods. These results were consistent with the artifacts seen in the reformatted coronal images. The RPM amplitude sorting method had significantly lower *FOM* values than the RPM phase angle sorting method for two of the five patient cases; these differences were also consistent with the artifacts seen in the reformatted coronals.

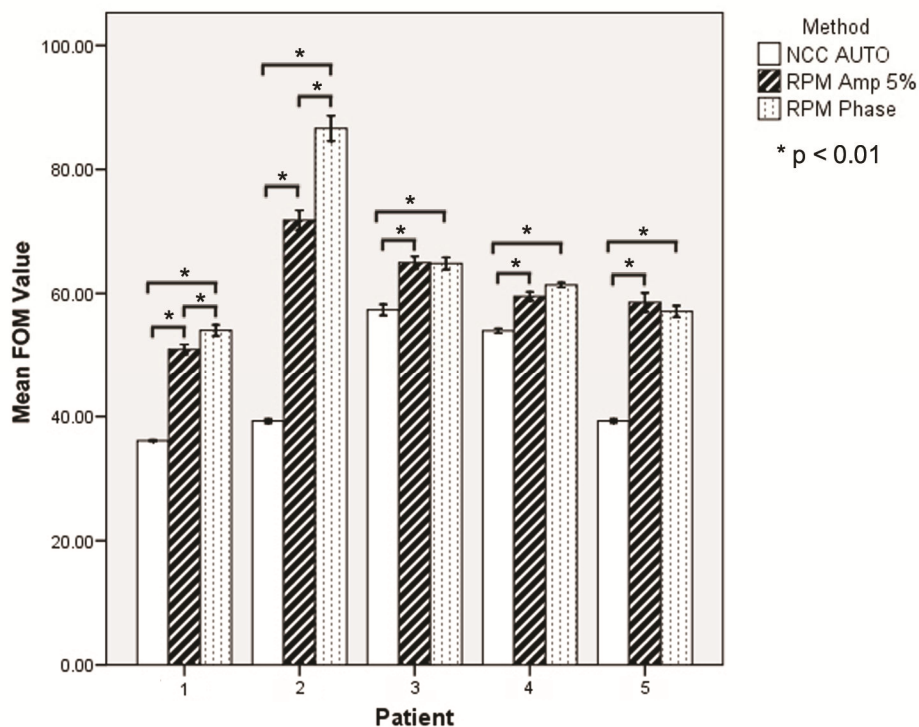


Figure 3-10: FOM values of the overlapping slice pairs for each patient. Significant between methods is indicated. In general, the NCC method was significantly better than both external marker methods.

Figures 3-11 and 3-12 shows the results of the histogram analysis for a single patient. Figure 3-11 contains histograms of the amplitude values associated with the NCC volumes; for comparison the RPM amplitude method histograms are plotted on the same graph. The x-axis is labeled with the amplitude bin values, between the global minimum and global maximum of the RPM curve for this patient. The y-axis is the bin value frequency. The histograms from the RPM method display a single bin distribution. This is expected as the images are binned according to the amplitude value. In comparison, the NCC image histograms, while centered on the RPM images' histograms,

show a wide distribution of amplitude values. Figure 3-12 shows the phase angle histogram for the NCC and phase angle sorted volumes. The x-axis is labeled with the sorting bins, between 0 and 2π . The same results as figure 3-11 are evident: the RPM phase angle histograms are confined to a single bin while the NCC image histograms show a wide range of bins with values.

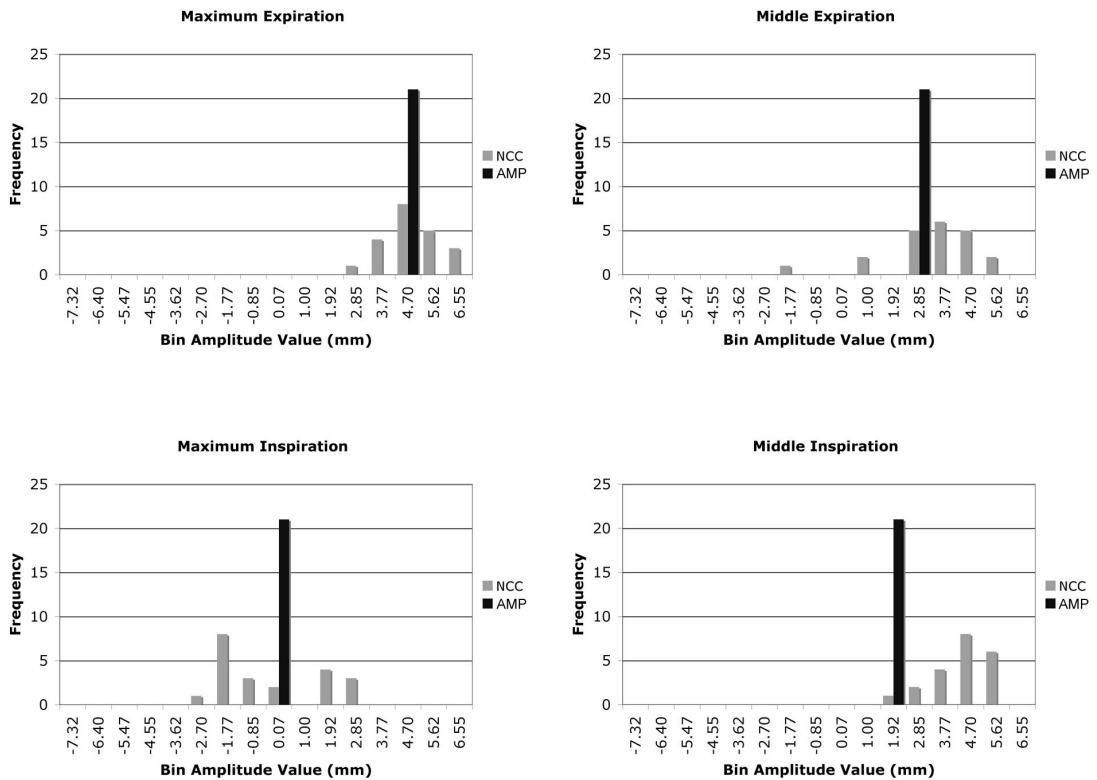


Figure 3-11: Frequency histogram plots of the RPM amplitude (AMP) values associated with the 3D volumes sorted by both the RPM amplitude sorting and the NCC methods.

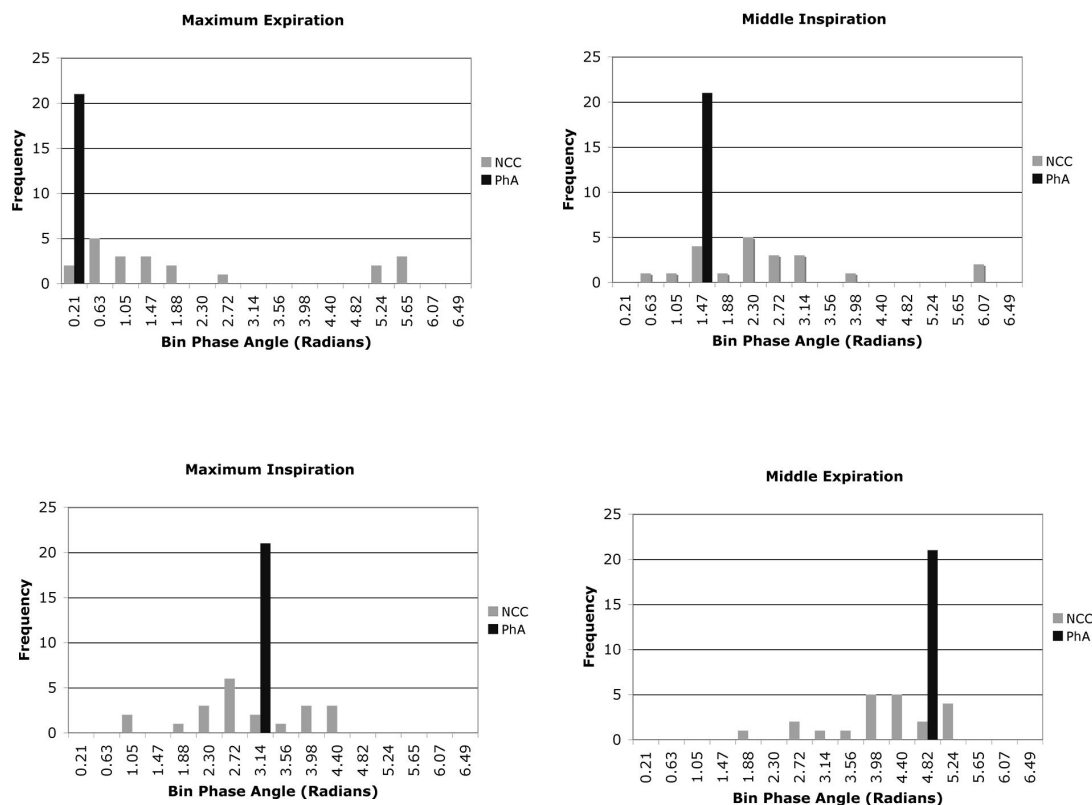


Figure 3-12: Frequency histogram plots of the RPM phase angle (PhA) values associated with the 3D volumes sorted by both the RPM phase angle sorting and the NCC methods.

3.4 Discussion

Phase angle 4D-CT sorting relies upon the calculation of a phase angle value from a respiratory amplitude curve. Phase angle calculation software, like the software used in this study, constrains each breathing period to a phase angle between the values of 0 and 2π radians, regardless of variations in the amplitude of the curve. Sudden amplitude variations lead to aperiodic shifts in the phase angle curve, as seen in figure 3-8. Amplitude variations violate the assumption that the patient's breathing is regular and

cause inconsistencies in the phase angle curve and in the final 4D-CT dataset. In the presence of these amplitude variations the automated NCC method is able to produce artifact reduced 4D-CT images. A comparison between the two methods readily demonstrates the limitation of phase angle sorting. Thus, phase angle sorting should be performed only for patients without major variations in their breathing cycle amplitudes.

Amplitude variations, which cause artifacts in 4D-CT volumes, can be dealt with using of the amplitude curve to sort 4D datasets. The amplitude sorting method presented here removes amplitude variations from the final 4D-CT dataset by exclusion of incomplete volumes. This allows for breathing cycle variations, in the form of amplitude variations, to be filtered from the sorted volumes. However, this technique imposes the assumption that a single marker's motion reflects the motion of the entire deformable chest cavity and internal lesions. Work quoted by *Chi et al.*³⁵, *Ozhasoglu et al.*⁴ and *Wu et al.*³⁶ suggests that correlation between a single external marker and entire chest cavity is not assured.

The findings in this work suggest a similar trend, that the motion of a single external marker is not 100% correlated to the rest of the chest. A volume determination method based upon image similarity (NCC method) demonstrated a lower degree of image artifacts both qualitatively and quantitatively than two external marker methods. The histogram analysis showed that the NCC determined volumes were made up of images having a wide range of external marker values. This simple analysis was able to show a lack of correlation between the external marker and the entire chest. Further investigation would have to be performed to look at the full tumour motion-external marker correlation.

For the NCC method each time series of images was shifted to begin at maximum expiration. To determine the maximum expiration an image derived chest height (CH) index was used. The CH index was used instead of the RPM device to allow the algorithm to function completely independent of the RPM device. We chose to shift the images to maximum expiration because within the cycle it is the most stable portion of the breathing cycle. To use the CH index for anything other than determining maximum expiration would require testing the relationship between the CH index and the rest of the chest.

The NCC method required approximately 30 minutes of computing time to complete. Computational time this high is impractical for clinical applications. The algorithm was running using a high level language (IDL) without fully optimizing the code. Implementation and optimization in a low level language could dramatically improve computing time. As well, parallelization and implementation using GPU processing of the algorithm to sort each breathing phase independently of each other would reduce the total processing time by a factor of 16. These improvements would make the algorithm practical for centres without 4D-CT sorting capability.

Past studies that have reported on external marker tumour correlation have chosen the location of the external marker to provide the largest range of motion; usually on the abdomen. However, mounting evidence suggests that there is not a universal location that provides the best marker-tumour correlation. The location of the external marker should be optimized to provide maximum correlation with the tumour motion if the respiratory signal is to be used in gated radiotherapy. The automated image based 4D-CT

protocol developed here could provide a useful unbiased tool to determine the location of maximum tumour-marker correlation.

In a number of studies, 4D-CT scans have been validated through the use of moving phantom data.^{19, 22, 24, 26, 34} All of these phantoms are rigid in nature and do not provide the important visco-elastic characteristics of the lungs that lead to breathing hysteresis and a non-linear relationship between the motion of an external marker and the motion of other chest positions. To assess 4D-CT datasets properly either a non-rigid phantom or an animal model must be developed. *Lu et al.*³³ has mentioned the use of a non-ionizing implanted AC electromagnetic transponder (4D Localization System, Calypso Medical, Seattle, WA) that would provide comprehensive 4D information of an implanted marker that could properly validate the 4D-CT sorting process. However, such a system is limited by cost and availability. In future work, we plan to develop a pig animal model to validate the NCC image selection algorithm we use for our volume determination. An animal model allows testing of the algorithm on a visco-elastic lung tissue system.

The *Volume Determination* step determines the reference scan position that produces the most coherent 4D-CT dataset. This step is required to accommodate for non-reproducibility in the breathing cycle. Depending on the degree of variation that is seen in the breathing cycle, a specific breathing state may only occur once. Determining which reference scan position (and breathing cycle) represents data that occurred during every scanned breathing cycle is important to eliminate artifacts. However, a limitation in our method is the use of only the 12 most inferior scan positions as a survey of reference images. The purpose of the survey is to eliminate artifacts caused by irregular

breathing, however, by only searching 1/2 to 1/3 of the breathing cycles collected irregular breathing artifacts may still hinder the final volumes.

The choice to use only the 12 most inferior scan positions was dictated by the NCC algorithm's specific sensitivity to anterior-posterior motion when aligning axial images according to respiratory phase. The respiratory motion observed in the more superior images is predominately contained within the lung tissue and is in the superior-inferior direction. While this motion is enough to register images at the end of the image matching "daisy chain", the lack of motion hinders sorting when it is used as a reference image and propagated through an entire volume. In future work, we plan to increase the sensitivity of the NCC algorithm to detect superior-inferior motion in the lung tissue in order to use all the images as reference images.

The effective dose to a patient from a 4D-CT study using our scanning protocol was approximately 18 mSv, but will vary slightly depending on the volume being scanned and the breath rate of the patient. Scanning with an overlapping image adds approximately 33% to the effective dose (12 mSv vs. 18 mSv). We were able to use a low current (80 mA) due to the high contrast in the lung. As well, decreased scan times, computational times, and dose would be afforded by the use of scanners with larger axial field of view coverage (e.g. 16 or greater slices).

This algorithm requires serial ciné scanned CT images. It has limited applicability to helical scanning. The algorithm requires overlapping images from adjacent scan positions to perform the volume determination. If this was to be performed using helical acquisition the data would have to be collected as a series of volumes scans

during which the table would shuttle backward after each sections scanned, in order to provide the overlapping segments.

It is important to note that the efficacy of gated radiotherapy depends upon reproducibility of the 4D-CT scans and the ability to track the anatomy during therapy. Regardless of the quality of the 4D-CT images, non-reproducibility of 4D-CT scans can arise from the methods or the inherent non-reproducibility of breathing motion. Currently, the reproducibility of various 4D-CT algorithms has not been assessed and it will be a future priority if 4D-CT is to be used to confidently guide respiratory-gated radiotherapy. The automatic NCC algorithm does not require user intervention and is therefore algorithmically more reproducible by design. As a result, our NCC 4D-CT scans would highlight non-repeatable breathing patterns in patients and facilitate the development of methods to minimize variability.

3.5 References

1. Brandner, E.D., et al., *Localizing moving targets and organs using motion-managed CTs*. Medical dosimetry : official journal of the American Association of Medical Dosimetrists, 2006. **31**: p. 134-40.
2. Ekberg, L., et al., *What margins should be added to the clinical target volume in radiotherapy treatment planning for lung cancer?* Radiotherapy and oncology : journal of the European Society for Therapeutic Radiology and Oncology, 1998. **48**: p. 71-7.
3. Mageras, G.S., et al., *Measurement of lung tumor motion using respiration-correlated CT*. International journal of radiation oncology, biology, physics, 2004. **60**: p. 933-41.
4. Ozhasoglu, C. and M.J. Murphy, *Issues in respiratory motion compensation during external-beam radiotherapy*. Int J Radiat Oncol Biol Phys, 2002. **52**(5): p. 1389-99.
5. Shimizu, S., et al., *Impact of respiratory movement on the computed tomographic images of small lung tumors in three-dimensional (3D) radiotherapy*. International journal of radiation oncology, biology, physics, 2000. **46**: p. 1127-33.
6. Kubo, H.D. and B.C. Hill, *Respiration gated radiotherapy treatment: a technical study*. Physics in medicine and biology, 1996. **41**: p. 83-91.
7. Butler, L.E., et al., *Dosimetric benefits of respiratory gating: a preliminary study*. Journal of applied clinical medical physics / American College of Medical Physics, 2004. **5**: p. 16-24.
8. Engelsman, M., et al., *How much margin reduction is possible through gating or breath hold?* Physics in Medicine and Biology, 2005. **50**: p. 477-490.
9. Seppenwoolde, Y., et al., *Precise and real-time measurement of 3D tumor motion in lung due to breathing and heartbeat, measured during radiotherapy*. International journal of radiation oncology, biology, physics, 2002. **53**: p. 822-34.
10. Underberg, R.W.M., et al., *Benefit of respiration-gated stereotactic radiotherapy for stage I lung cancer: an analysis of 4DCT datasets*. International journal of radiation oncology, biology, physics, 2005. **62**: p. 554-60.
11. Shirato, H., et al., *Four-dimensional treatment planning and fluoroscopic real-time tumor tracking radiotherapy for moving tumor*. International journal of radiation oncology, biology, physics, 2000. **48**: p. 435-42.

12. Bradley, J.D., et al., *Comparison of helical, maximum intensity projection (MIP), and averaged intensity (AI) 4D CT imaging for stereotactic body radiation therapy (SBRT) planning in lung cancer*. Radiotherapy and oncology : journal of the European Society for Therapeutic Radiology and Oncology, 2006. **81**: p. 264-8.
13. Keall, P.J., et al., *The management of respiratory motion in radiation oncology report of AAPM Task Group 76*. Med Phys, 2006. **33**(10): p. 3874-900.
14. Ford, E.C., et al., *Evaluation of respiratory movement during gated radiotherapy using film and electronic portal imaging*. International journal of radiation oncology, biology, physics, 2002. **52**: p. 522-31.
15. Minohara, S., et al., *Respiratory gated irradiation system for heavy-ion radiotherapy*. International journal of radiation oncology, biology, physics, 2000. **47**: p. 1097-1103.
16. Rietzel, E., et al., *Four-dimensional image-based treatment planning: Target volume segmentation and dose calculation in the presence of respiratory motion*. Int J Radiat Oncol Biol Phys, 2005. **61**(5): p. 1535-50.
17. Underberg, R.W.M., et al., *Use of maximum intensity projections (MIP) for target volume generation in 4DCT scans for lung cancer*. International journal of radiation oncology, biology, physics, 2005. **63**: p. 253-60.
18. Fitzpatrick, M.J., et al., *Displacement-based binning of time-dependent computed tomography image data sets*. Medical Physics, 2006. **33**: p. 235.
19. Keall, P.J., et al., *Acquiring 4D thoracic CT scans using a multislice helical method*. Physics in Medicine and Biology, 2004. **49**: p. 2053-2067.
20. Low, D., et al., *A method for the reconstruction of four-dimensional synchronized CT scans acquired during free breathing*. Medical Physics, 2003. **30**: p. 1254.
21. McClelland, J., et al., *A continuous 4D motion model from multiple respiratory cycles for use in lung radiotherapy*. Medical Physics, 2006. **33**: p. 3348.
22. Pan, T., et al., *4D-CT imaging of a volume influenced by respiratory motion on multi-slice CT*. Medical Physics, 2004. **31**: p. 333.
23. Vedam, S.S., et al., *Acquiring a four-dimensional computed tomography dataset using an external respiratory signal*. Phys Med Biol, 2003. **48**(1): p. 45-62.
24. Wink, N., C. Panknin, and T.D. Solberg, *Phase versus amplitude sorting of 4D-CT data*. J Appl Clin Med Phys, 2006. **7**(1): p. 77-85.

25. Ehrhardt, J., et al., *An optical flow based method for improved reconstruction of 4D CT data sets acquired during free breathing*. Medical Physics, 2007. **34**: p. 711.
26. Rietzel, E. and G.T.Y. Chen, *Improving retrospective sorting of 4D computed tomography data*. Medical Physics, 2006. **33**: p. 377.
27. Kini, V.R., et al., *Patient training in respiratory-gated radiotherapy*. Med Dosim, 2003. **28**(1): p. 7-11.
28. Neicu, T., et al., *Synchronized moving aperture radiation therapy (SMART): improvement of breathing pattern reproducibility using respiratory coaching*. Physics in medicine and biology, 2006. **51**: p. 617-36.
29. Zeng, R., et al., *Iterative sorting for four-dimensional CT images based on internal anatomy motion*. Medical Physics, 2008. **35**: p. 917.
30. Zhang, Q., et al., *A patient-specific respiratory model of anatomical motion for radiation treatment planning*. Medical Physics, 2007. **34**: p. 4772.
31. Kleshneva, T., J. Muzik, and M. Alber, *An algorithm for automatic determination of the respiratory phases in four-dimensional computed tomography*. Physics in medicine and biology, 2006. **51**: p. N269-76.
32. Lu, W., et al., *A semi-automatic method for peak and valley detection in free-breathing respiratory waveforms*. Medical Physics, 2006. **33**: p. 3634.
33. Lu, W., et al., *A comparison between amplitude sorting and phase-angle sorting using external respiratory measurement for 4D CT*. Medical Physics, 2006. **33**: p. 2964.
34. Abdelnour, a.F., et al., *Phase and amplitude binning for 4D-CT imaging*. Physics in medicine and biology, 2007. **52**: p. 3515-29.
35. Chi, P.-C.M., et al., *Relation of external surface to internal tumor motion studied with cine CT*. Medical Physics, 2006. **33**: p. 3116.
36. Wu, H., et al., *Gating based on internal/external signals with dynamic correlation updates*. Physics in medicine and biology, 2008. **53**: p. 7137-50.
37. Hope, A. *Applications of Manifold Learning Techniques in 4D-CT Reconstruction*. in ICCR 2007. 2007. Toronto, Ontario, Canada.
38. Eck, K. and J. Bredno, *Absolute alignment of breathing states using image similarity derivatives*. Imaging 2005: Visualization, Image, 2005.

Chapter 4

Applying an animal model to quantify the uncertainties of an image based 4D-CT algorithm

4.1 Introduction

A tumor in a patient's thoracic cavity exhibits periodic motion as a result of respiration. The motion of the tumour adds uncertainty to the radiotherapy treatment planning of the patient.¹⁻³ Enlargement of the radiation treatment margins or gating of the radiation beam are used to ensure that the entire prescribed dose is delivered primarily to the moving tumour. Both optimization of the treatment margins and planning of the respiratory gated radiotherapy require accurate dynamic volume imaging of the thorax and tumour as they move during respiration.^{4, 5}

Four dimensional computed tomography (4D-CT) has been developed to provide volume images of the entire chest at multiple time points throughout respiration.⁶⁻⁸ The most common of the many 4D-CT techniques that have been developed relies on data from an external respiratory surrogate (external marker,⁷⁻⁹ spirometry and bellows,^{6, 10} strain gauge,¹¹ etc.) to sort asynchronously acquired CT images into respiratory phase bins. Potential errors arising from uncorrelated motion between the respiratory surrogate and the entire internal anatomy¹²⁻¹⁴ have led to the development of 4D-CT methods that do not require the use of external respiratory surrogate data: image based 4D-CT sorting methods (NCC¹⁵, multi-internal surrogates¹⁶ and manifold learning¹⁷).

Currently, 4D-CT image sorting methods have been qualitatively assessed in a number of phantom studies. The phantoms most commonly used are rigid lung phantoms that have a programmable motor driving a solid insert in the cranial-caudal direction.^{9, 18,}

¹⁹ The primary limitations of these phantoms are the lack of deformable lung-like material and chest wall, thus rendering them unusable to investigate the correlation between an external marker and both the nonrigid motion and density variations of the 'lung'. However, there have also been developments in lung-like deformable phantoms.^{20,}

²¹ These phantoms have sacs filled with a deformable foam with density similar to lung tissue. A programmable piston that is capable of following the motion of a recorded patient breathing curve drives the deformation of the sacs. While this is an improvement over the rigid phantoms, these phantoms are still limited by the use of simulated lung tissue, a geometry that is not representative of a patient and the lack of a chest-lung interface to provide resistance during respiration. *Biederer et al.*²² have developed an *ex-vivo* pig lung phantom that is contained within a chest phantom to provide a more realistic pleural space. This design more accurately represents the mechanical properties of a living lung. However, there are doubts that dead lung tissue, which has been excised for 8 hours prior to scanning, would have the same viscoelastic properties and density variations as living lung tissue

In this chapter we develop a method to quantitatively assess the uncertainties of an image based 4D-CT sorting method using live ventilated pigs. Irregularities in the breathing amplitude of the pigs were induced to provide amplitude variations commonly seen in radiotherapy patients. The image based 4D-CT method that this study was designed to test was previously published by our group.¹⁵ Using a nonlinear registration

algorithm we measured the displacement uncertainties, relative to a reference volume, caused by the inherent assumptions of the 4D-CT algorithm. The methods are presented specifically for the image based 4D-CT algorithm, but the ideas could be extended to 4D-CT algorithms reliant on external markers.

4.2 Methods

4.2.1 4D-CT Algorithm and Associated Errors

The goal of a 4D-CT algorithm is to produce a time series of 3D volumes that covers an area (e.g. the thorax) that is larger than the axial field of the view of the CT scanner. The 4D-CT algorithm we have previously published¹⁵ produces these volumes automatically from multiple ciné scans of subvolumes acquired sequentially to cover the entire volume as shown in figure 4-1 for three adjacent ciné scans. A spatial link between adjacent ciné scan subvolumes is created by using an overlapping image between the two abutted ciné scans. To generate a 3D volume at a specific respiratory phase of the 4D-CT dataset a subvolume at that particular phase from a ciné scan is first selected. The density of the lungs changes during respiration, leading to a periodic variation of lung CT values, that can be exploited by a pixel-based algorithm. An intensity based image similarity metric, the normalized cross correlation (NCC), can be used to match an image from the starting subvolume to an image from the adjacent ciné scan at the overlapping image position; this matching selects an entire subvolume from the adjacent ciné scan, assuming that the selected image and the associated subvolume are at the same respiratory phase. This selected subvolume is concatenated with the

starting subvolume and used to match a subvolume from the next adjacent ciné scan in a 'daisy chain' fashion. This procedure continues in both inferior and superior directions 'stitching' subvolumes together, resulting in a full 3D volume at the same respiratory phase of the starting subvolume. 3D volumes at other respiratory phases can be similarly generated by repeating this process.

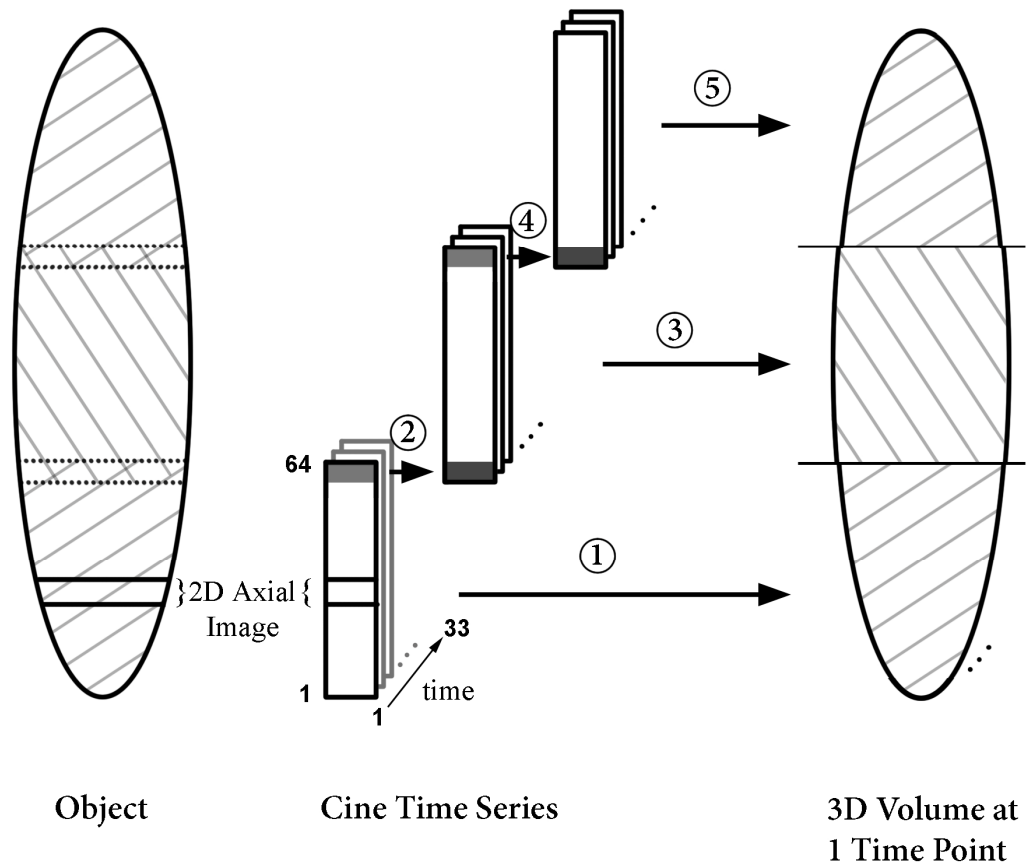


Figure 4-1: A diagram describing the 4D-CT scanning protocol which uses multiple cine scans of subvolumes that overlap in one image location to cover the whole extent of the object. The 4D-CT sorting algorithm applied to the acquired 4D-CT data to assemble the whole volume at different respiratory phases consists of the following steps: (1) A subvolume at a particular respiratory phase is selected from the starting ciné scan and transferred to the to be assembled 3D Volume at that respiratory phase as the first

subvolume. (2) A subvolume at the same respiratory phase is selected from the next adjacent cine scan by maximizing the NCC between an image from the starting subvolume and images from the adjacent cine scan of the overlapping image (3) The matched volume is added to the 3D volume. (4) Step 2 is repeated for the next adjacent cine scan using the selected subvolume in step 2 as the reference subvolume. (5) The matched volume is added to the 3D volume. (6) steps 2-5 are repeated until all cine scans inferior and superior to the starting cine scan are matched with the reference subvolume selected in step 1. The process is repeated for each subvolume at different respiratory phases from the starting cine scan.

The 4D-CT algorithm shown in figure 4-1 relies on two main assumptions to produce accurate synchronized 3D volumes. These two assumptions and the possible uncertainties are:

i) It is assumed that the NCC coefficient between two images from an overlapping image location is highly sensitive to the respiratory induced spatial and temporal displacements and lung density changes between the two images. This assumption is used to match the respiratory phase of a reference image to an image from a separate time series of images, located at an overlapping image location. The image from the second time series that maximizes the NCC coefficient with the reference image is selected as the match. In practice, two matched images will not be exactly the same and anatomical features within them will be displaced with respect to each other; this displacement (σ_{total}) is the summation in quadrature of a random uncertainty (σ_0) and a NCC uncertainty (σ_{NCC})²³ given by:

$$\sigma_{total}^2 = \sigma_0^2 + \sigma_{NCC}^2 \quad (4.1)$$

The random uncertainty is a result of the limitations of CT image acquisition (pixel noise, finite image acquisition interval, misalignment of the respiratory phase bins and image acquisition intervals, motion artifacts, etc) and of the method used to measure the displacement (in this paper a nonlinear registration algorithm is used). The random uncertainty gives rise to the minimum measurable displacement between the reference and matched image as determined by the nonlinear registration algorithm. The NCC uncertainty is the additional displacement above the random uncertainty resulting from inaccuracies of the NCC algorithm's ability to choose the image that is the best anatomical match to the reference image.

In order to model the NCC uncertainties we must perform consecutive matches at the same image location using multiple ciné scans acquired at the same anatomical location (see 'scanning protocol' below). Two consecutively image matches require 3 time series of images at the same overlapping image location: an image from the first time series (reference) is matched to an image from the second time series; then the image from the second time series is subsequently matched to an image from the third time series. The displacement between the final matched image and the original reference image is measured. The total displacement results from the NCC uncertainties adding in quadrature:

$$\sigma_{total}^2 = \sigma_0^2 + 2\sigma_{NCC}^2 \quad (4.2)$$

If the NCC matching is performed n times at the same overlapping image location, the NCC error from each matching adds in quadrature and a general equation can be developed:

$$\sigma_{total}(n) = \sqrt{\sigma_0^2 + n\sigma_{NCC}^2} \quad (4.3)$$

where $\sigma_{total}(n)$ is the total spatial displacement uncertainty between the reference image and the image obtained after performing n NCC matches.

ii) It is assumed that all images within each ciné scan subvolume move synchronously in phase with each other. Therefore, any two subvolumes from separate ciné scans can be matched in respiratory phase using any pair of overlapping images between them. One subvolume will act as a reference and any image pair between the reference subvolume and the subvolume being matched that occurs at an overlapping image position can be used to perform the match, therefore this assumption is referred to as the reference image invariance assumption. The image based 4D-CT algorithm uses the extreme case where there is only a single pair of overlapping images between two separate ciné scans.¹⁵ In order to test this assumption for an arbitrary location of the overlapping image pair between two subvolumes (reference and comparison), we used an experimental design where we ciné scanned the same section of the thorax multiple times (see 'scanning protocol' below). The difference in displacement between subvolumes matched using different pairs of overlapping slices is calculated for individual images:

$$\Delta\sigma_B(A, B) = \sigma_B(A) - \sigma_B(B) \quad (4.4)$$

where $\sigma_B(A)$ is the spatial displacement of image B of the matched comparison subvolume with respect to the reference subvolume image B when the overlapping image A in the reference subvolume was used to match the comparison subvolume;

$\sigma_B(B)$ is similarly defined as the spatial displacement of image B of the matched comparison subvolume with respect to the reference subvolume image B when the overlapping image B in the reference subvolume was used to match the comparison subvolume;

$\Delta\sigma_B(A,B)$ is the difference in spatial displacement of image B of the matched comparison volumes with respect to the reference subvolume image B as a result of using either overlapping image A or image B to match the comparison subvolume.

In practice, the NCC 4D-CT algorithm will use either the most inferior or the most superior overlapping images of the reference and comparison subvolumes to match the entire comparison subvolume. Therefore, within this study we will limit the choices of image A from the reference volume used for matching to be the most inferior and superior image. The displacements will be measured at all other image locations (image B).

4.2.2 Scanning Protocol

Six female Landrace cross pigs (30-50 kg) were scanned using a GE Healthcare Discovery CT750 HD Scanner (Waukesha, WI). The pigs were mechanically ventilated using a Harvard Apparatus ventilator (Holliston, MA) with a respiratory period of 3 seconds. A single 4.0 cm section of the pig's chest, chosen to include the diaphragm, was ciné (continuously) scanned 6 times, each ciné scan lasting for 3.6 seconds, with the couch stationary. The ventilated breathing cycle was disrupted by crimping the ventilator

gas return tube approximately once every 3 seconds to produce inconsistent breathing amplitudes. The CT scanner was set to scan at 120 kVp and 200 mA with a gantry rotation time of 0.4 seconds. Each ciné scan was retrospectively reconstructed into 33 volumes with a time spacing of 0.1 seconds. Each volume consisted of 64 contiguous images covering an axial distance of 4.0 cm with an isotropic voxel size of 0.625 mm³. The data from these 6 ciné scans were labeled the lower section data.

Three of the pigs had two additional series of ciné scans performed on them to acquire data from different locations of the animal's chest. After the lower section scan data were acquired the scan table was translated 3.75 cm superiorly twice and at each location another 6 ciné scans were acquired. These two additional sections were labeled the middle and the upper section and were all retrospectively reconstructed in the same manner as the data from the lower section scans.

4.2.3 Nonlinear Registration Algorithm

The nonlinear registration algorithm that we used in this paper had previously been used to measure displacements due to respiratory motion.²⁴ In this manuscript the warping algorithm registers volumes that were 512 x 512 x 64 pixels in dimensions and returned a vector displacement field that was one half the dimensions of the input images (256 x 256 x 32). The magnitude of each displacement vector was calculated to produce a 3D array of magnitude of displacements ($|r| = \sqrt{|\vec{x}|^2 + |\vec{y}|^2 + |\vec{z}|^2}$). For the analysis the images located at the boundary of the (sub)volume are excluded because nonlinear registration algorithms are subject to greater errors when matching pixels at the limits of

volumes of interest. Therefore, the most superior and most inferior images of each subvolume are taken to be the 10th and 54th image, respectively.

4.2.4 Uncertainty Analysis Experiments

4.2.4.1 Uncertainties Due to NCC Matching

The uncertainties that result from using the NCC method to spatially match images were determined using equation 4.3. The total spatial displacements were determined as a function of number of NCC matches, using volumes from the 6 ciné scans acquired at each of the three scan sections (six animals for the lower section and three animals for the middle and upper sections). For each scan section, the first of the 6 ciné scans was set as the reference scan. The reference scan was subsampled at a 0.3 s time interval to reduce the number of reference volumes from 33 to 12. The other 5 ciné scans were set as the comparison scans (numbered and ordered from 1 to 5) through which volumes were matched successively (using NCC); first the volumes from the reference scan and then to the matched comparison scan, at the overlapping image positions (figure 4-2). Image matching was repeated by varying: either the reference image from the 10th to 54th image (every other image) of reference volumes, the reference volume used for matching from one of the 12 possible reference volumes or the ordering of ciné comparison scans used for the matching from one of the 120 possible permutations (${}_5P_5$).

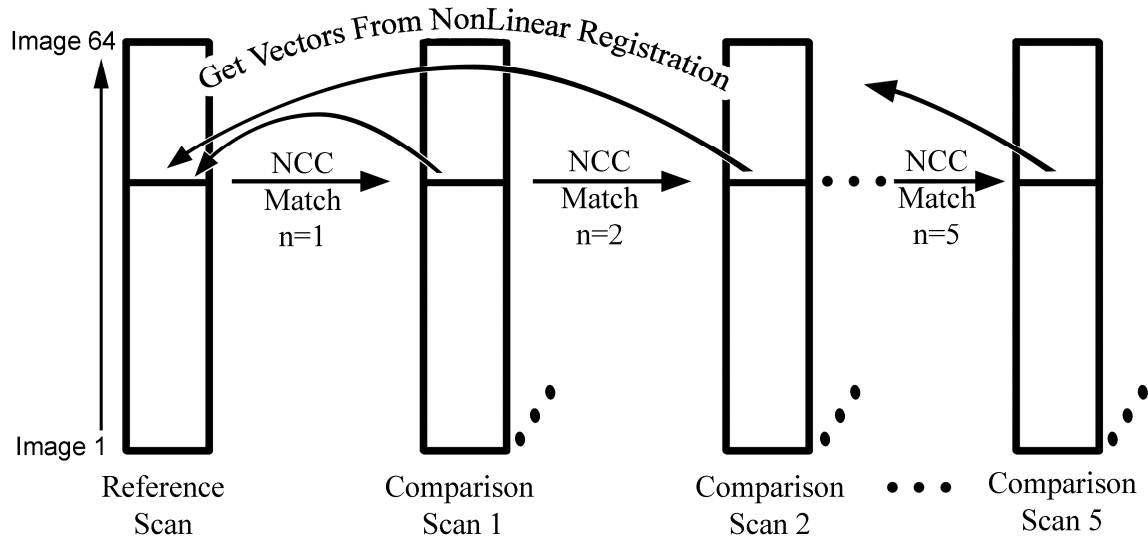


Figure 4-2: Illustration of method to assess the uncertainty due to NCC matching. The method is shown for one reference image location and one comparison scan matching order. After selecting a single reference volume the NCC is calculated between the image from the reference volume and the cine time series of images at the overlapping image from Comparison Scan 1. The image (and volume) that maximizes the NCC is selected as the match. The selected image from Comparison Scan 1 is then used to match an image (volume) from Comparison Scan 2, using the same NCC matching procedure. This is repeated for all 5 Comparison Scans. The matched volumes are nonlinearly registered to the Reference volume to obtain the spatial displacement between the matched and reference volumes. Only displacement values for the image location used to perform the matching were used for the uncertainty analysis.

The displacements of the matched images with respect to the reference images were calculated using nonlinear registration. In order to minimize nonlinear registration artifacts the entire final matched volume was nonlinearly registered to the entire reference volume. The magnitude of each nonlinear displacement vector field was calculated to

produce a displacement map. However, only the registration results for the images used during each NCC matching were used for the NCC uncertainty analysis. Three circular regions of interest were drawn on each reference image (regions in the left lung, chest wall and over the entire thorax as shown in figure 4-3). These regions were overlaid on each deformation map and the average values within each of them were calculated. The results were then grouped according to the number of NCC matches performed to obtain the final match (n equal 1 to 5). The total NCC uncertainty, $\sigma_{total}(n)$, corresponding to each n matches for each animal was obtained by averaging over all 22 images in a reference volume, 12 reference volumes and 120 permutation orders of matching for each animal. The results were averaged over all animals. Equation 4-3 was fit to the measured data, $\sigma_{total}(n)$, using SigmaPlot (San Jose, CA). The parameters for σ_0 and σ_{NCC} were obtained from the nonlinear curve fits and reported with their standard errors.

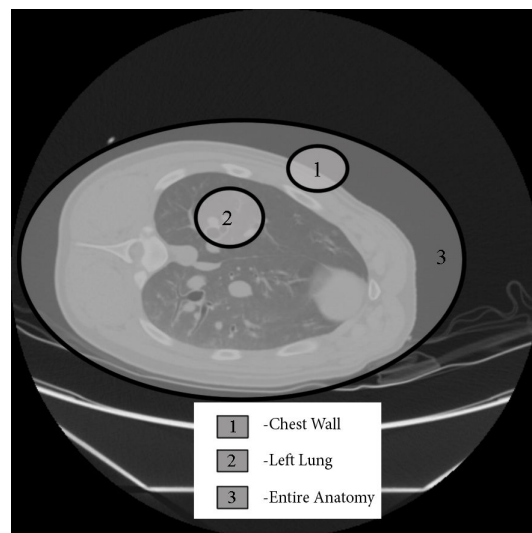


Figure 4-3: Location and approximate size of the regions of interest drawn. Region 3 includes the areas within regions 1 and 2.

4.2.4.2 Reference Image Invariance Assumption

The assumption that two subvolumes of the same anatomy from separate ciné scans can be matched in respiratory phase using any pair of overlapping images was tested by calculating $\Delta\sigma_B(A,B)$ (defined by equation 4.4) and testing for its significant difference from zero. The data from the 6 ciné scans acquired at each of the three scan sections (six animals for the lower section and three animals for the middle and upper sections) were matched using NCC. A single reference scan (the first scan) was used and each of the 5 comparison scans was matched to the reference scan independently for every overlapping image position (10^{th} through 54^{th} , incremented by 2). As in the evaluation of NCC error, the displacements of the matched volumes with respect to the reference volumes were determined from the nonlinear registration between the reference and matched volumes and maps of the magnitude of the displacement vectors were calculated (figure 4-4). Three regions of interest were drawn on the reference images (as shown in figure 4-3) and transferred to the magnitude maps where the average values from within the ROIs were recorded.

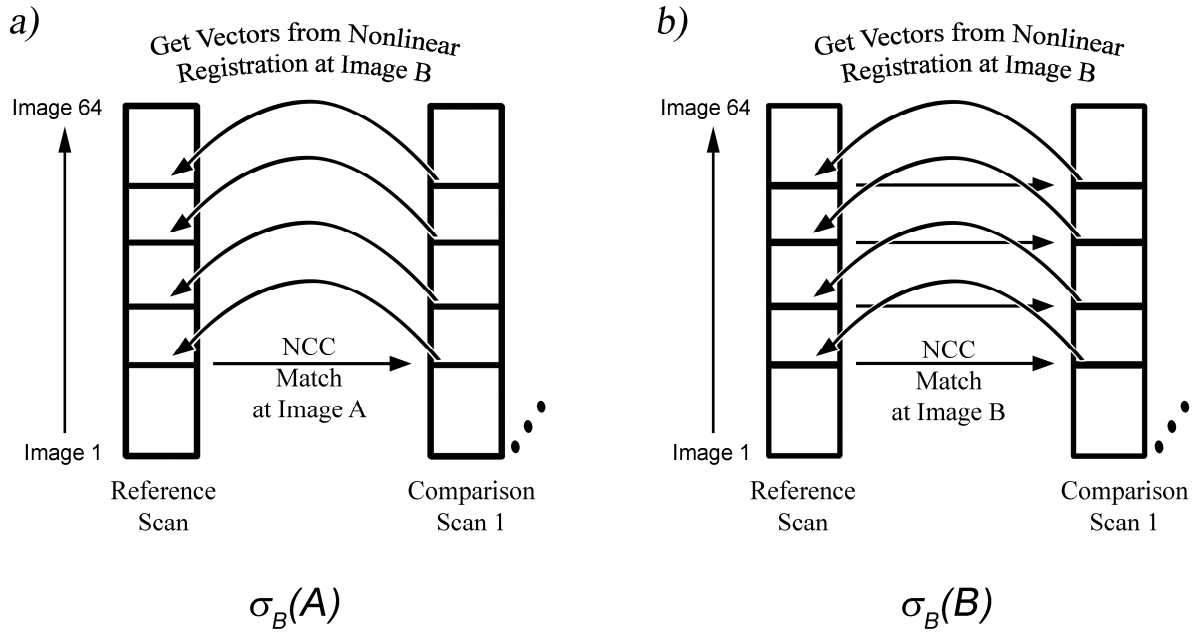


Figure 4-4: Illustration of the method to test the reference image invariance assumption. Diagrams are for obtaining the quantities on the right hand side of equation 4.4, shown for a single image A and multiple image B s. (a) A single reference volume is selected from the reference scan. A single image, image location A , is used to match an image (and volume) from Comparison Scan 1 by maximizing the NCC at the overlapping image location. The nonlinear registration is calculated between the matched comparison volume and the reference volume. The displacement between the two volumes is determined for overlapping image locations 10 to 54 (image B) to obtain values of $\sigma_B(A)$. (b) A single reference volumes is selected from the reference scan. For each image locations 10 to 54 within the reference scan, image locations B , separate matches are obtained from Comparison Scan 1 by maximizing the NCC at the corresponding overlapping image location. The displacement between each matched comparison volume and the reference volume is calculated using nonlinear registration. The displacement at the image used to performed the matching (image B) is recorded for each nonlinear registration to obtain values of $\sigma_B(B)$.

For each scanned section of each animal, $\sigma_B(A)$ and $\sigma_B(B)$ were determined for each of the 12 reference volumes and each of the comparison ciné scans and the results averaged together. This resulted in three groups of data, $\sigma_B(A=10)$, $\sigma_B(A=54)$, $\sigma_B(B)$ that were averaged over all animals for each ROI. $\Delta\sigma_B(A,B)$ for both image A positions (the inferior and superior, $A=10$ or 54 respectively) was calculated and the results were plotted as a function of image B . Two different Student's t-tests were performed on the quantity $\Delta\sigma_B(A,B)$ to determine if the value was significantly different from zero. The first t-test was performed after averaging the quantity $\Delta\sigma_B(A,B)$ over all image B s and animals to obtain values for each of the 3 sections and 3 ROIs. Additionally, $\Delta\sigma_B(A,B)$ was tested for two special cases: ($A=10, B=54$) and ($A=54, B=10$). These special cases simulate the situation used for the image based NCC 4D-CT sorting method we previously described.¹⁵

4.3 Results

4.3.1 Uncertainty due to NCC Matching

A graph of the results from the lower section displaying the magnitude of displacement of the matched comparison images relative to the reference images ($\sigma_{total}(n)$), for the three regions of interest (ROIs), as a function of number of NCC matches is shown in figure 4-5. The average displacement within the left lung ROI was above those of the chest wall and the entire thorax ROIs and increased from 0.9 mm, after 1 NCC match, to 1.5 mm, after 5 NCC matches. Table 4-1 shows the averaged fitting parameters obtained from fitting equation 4.3 to the measured displacements from the

lower, middle and upper sections respectively. The lower section left lung ROI had the highest value of σ_{NCC} with a value of 0.54 ± 0.10 mm/match. While the left lung σ_{NCC} value trended to decrease in the caudal to cranial direction (middle and upper sections 0.32 ± 0.06 mm/match and 0.32 ± 0.16 mm/match), the chest wall σ_{NCC} values trended to increase from 0.29 ± 0.10 mm/match in the lower section to 0.45 ± 0.15 mm/match in the upper section. The σ_{θ} value ranged from 0.77 ± 0.06 mm to 0.93 ± 0.06 mm and was consistently larger than σ_{NCC} in all scan sections and ROIs.

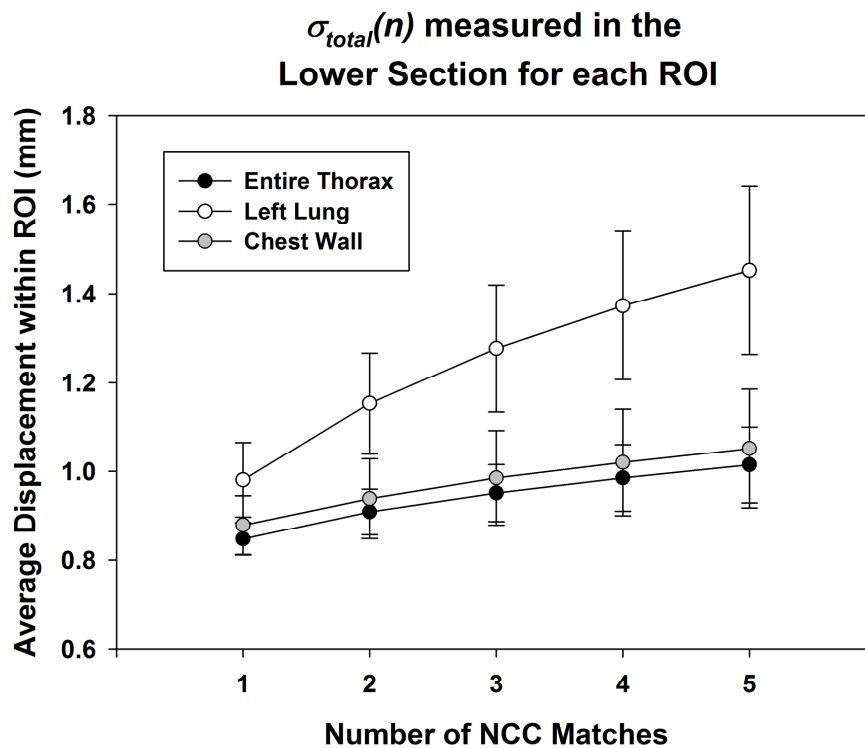


Figure 4-5: The average displacements relative to the reference volume as a function of the number of NCC matches performed. The data shown are for the lower sections of the pigs for all three regions of interest shown in figure 4-3. The errors bars are standard error.

Table 4-1: Summary of the fitting results of the NCC uncertainty equation (equation 4.3) for all ROIs in the lower, middle and upper sections. Values are mean \pm standard error.

NCC Displacement Uncertainty Equation Fitting Results						
	Entire Thorax		Left Lung		Chest Wall	
	Mean	SE	Mean	SE	Mean	SE
	(mm)		(mm)		(mm)	
Lower						
σ_0	0.81	\pm 0.07	0.84	\pm 0.18	0.84	\pm 0.12
σ_{NCC}	0.28	\pm 0.07	0.54	\pm 0.10	0.29	\pm 0.10
Middle						
σ_0	0.79	\pm 0.05	0.83	\pm 0.07	0.93	\pm 0.06
σ_{NCC}	0.17	\pm 0.08	0.32	\pm 0.06	0.29	\pm 0.06
Upper						
σ_0	0.77	\pm 0.06	0.92	\pm 0.18	0.84	\pm 0.22
σ_{NCC}	0.20	\pm 0.07	0.32	\pm 0.16	0.45	\pm 0.15

4.3.2 Reference Image Invariance Assumption

Figure 4-6 shows the graphs of $\sigma_B(A)$ and $\sigma_B(B)$ as defined in subsection 4.2.1 (ii) for the left lung ROI of the lower scanned section as the position of image B , corresponding to the overlapping slice location at which the displacements between the reference and comparison scan were measured, varied between the 10 and 54 in increments of 2. The graph for $\sigma_B(A)$ is shown for the case where the 10th image ($A=10$) in the reference volume was used for matching. The two curves overlap when $B=10$ and then diverge and maintain a small difference at other B values. Figure 4-7 plots $\Delta\sigma_B(A,B)$ versus B for $A = 10$ and 54 from the same section and ROI. The curves did not significantly differ from zero or from each other. The same trends were observed for the data from other ROIs and other scanned sections. Table 4-2 shows the values of

$\Delta\sigma_B(10,B)$ and $\Delta\sigma_B(54,B)$ averaged over all image B for each scan section and ROI. No value was significantly different from zero according to Student's t-test. Table 4-2 also shows the values of $\Delta\sigma_B(A,B)$ for $(A=10, B=54)$ and $(A=54, B=10)$ averaged over all reference volumes and animals for each section and ROI. Three of these values were significantly difference from zero (lower section entire thorax ROI $(A=10, B=54)$ and $(A=54, B=10)$; upper section chest wall ROI $(A=10, B=54)$).

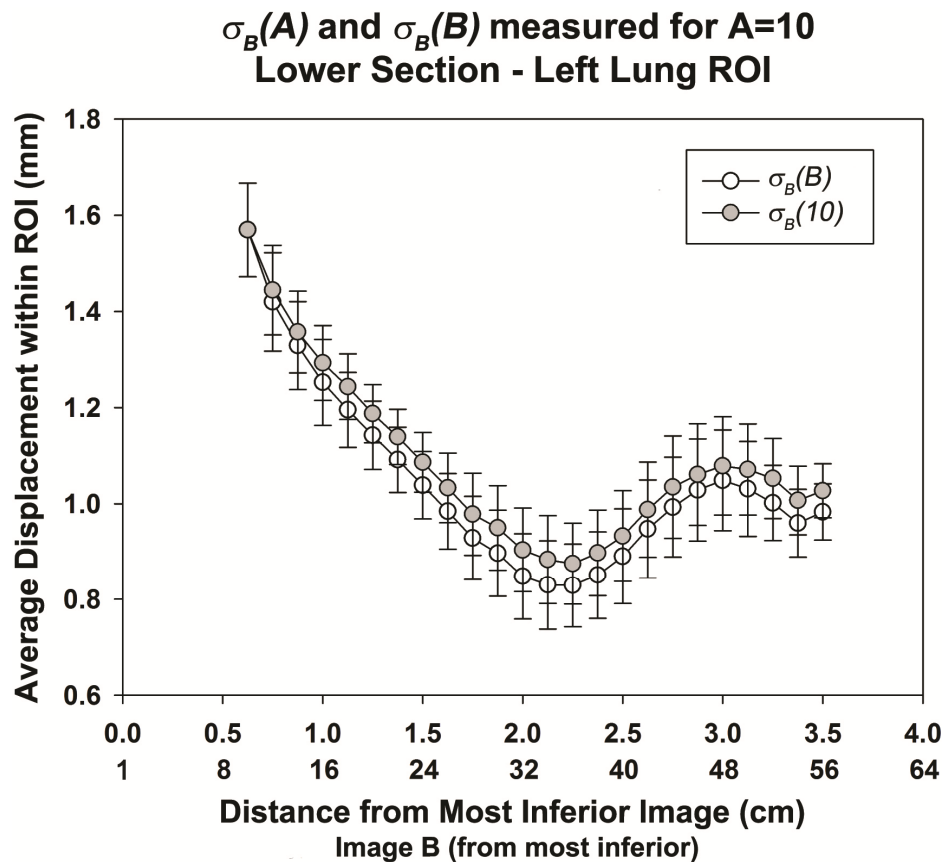


Figure 4-6: $\sigma_B(A=10)$ and $\sigma_B(B)$ for the left lung ROI in the lower scanned section of the pigs for image B equals 10 to 54. The graphs overlap at $B=10$, i.e. $B=A$, diverge slightly and maintain a small offset from each other as B increases from 10.

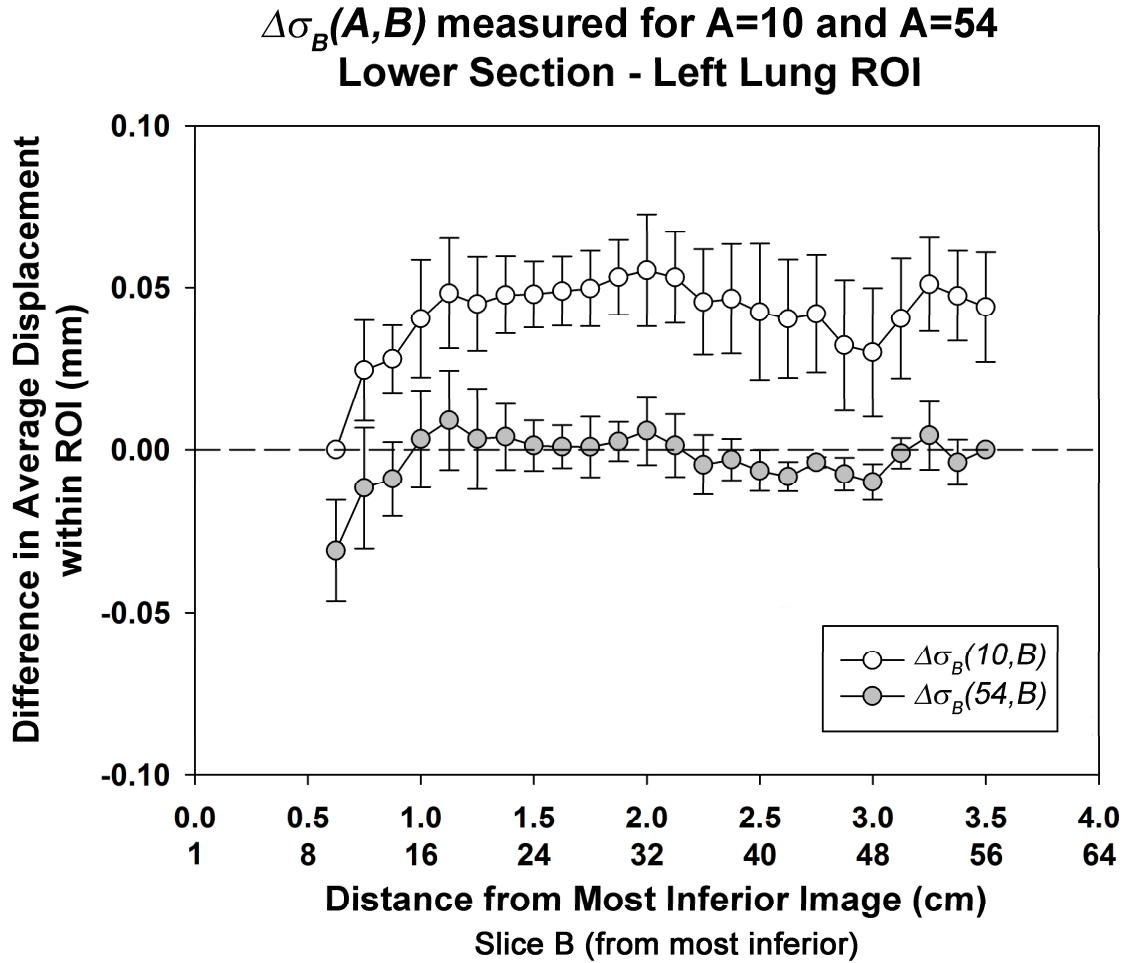


Figure 4-7: Plotted are the differences of $\sigma_B(A=10)$ and $\sigma_B(B)$ (i.e. $\Delta\sigma_B(10,B)$) and with image $A=54$ ($\Delta\sigma_B(54,B)$). Error bars are standard error.

Table 4-2: Summary of the results from the match image invariance experiment. Data are shown for $\Delta\sigma_B(A,B)$ averaged over all image B locations and for the case of $B=10$ and 54. Values are mean \pm standard error.

Results of the Reference Image Invariance Assumption Experiment (equation 4)								
Region of Interest								
Section	NCC Reference Image (A)	Disp. Measure Image (B)	Entire Thorax (mm)		Chest Wall (mm)		Left Lung (mm)	
			Mean	SE	Mean	SE	Mean	SE
Lower (df = 5)	Image 10	Average	0.015	+/- 0.012	0.004	+/- 0.017	0.044	+/- 0.029
		Slice 54	0.009*	+/- 0.003	-0.013	+/- 0.012	-0.031	+/- 0.015
	Image 54	Average	0.006	+/- 0.007	-0.013	+/- 0.033	-0.003	+/- 0.013
		Slice 10	0.017*	+/- 0.007	0.010	+/- 0.008	0.044	+/- 0.017
Middle (df = 2)	Image 10	Average	0.000	+/- 0.004	0.008	+/- 0.014	-0.003	+/- 0.025
		Slice 54	0.007	+/- 0.003	0.007	+/- 0.007	0.037	+/- 0.010
	Image 54	Average	0.003	+/- 0.003	0.005	+/- 0.009	0.017	+/- 0.009
		Slice 10	0.003	+/- 0.003	0.014	+/- 0.013	0.006	+/- 0.006
Upper (df = 2)	Image 10	Average	0.003	+/- 0.006	0.026	+/- 0.025	-0.006	+/- 0.009
		Slice 54	0.008	+/- 0.004	0.021*	+/- 0.003	-0.003	+/- 0.005
	Image 54	Average	0.005	+/- 0.004	0.033	+/- 0.027	0.021	+/- 0.024
		Slice 10	0.002	+/- 0.004	0.015	+/- 0.013	0.051	+/- 0.020

p < 0.05 versus zero

4.4 Discussion

The treatment planning and delivery of radiation therapy relies on accurate CT volume images of the tumour and the anatomy surrounding the tumour. Lung tumours are challenging to image because the volume of interest is often larger than the axial field of the view of the CT scanner. Therefore, full volume images must be stitched together from asynchronous data acquired over multiple breathing cycles. The process of combining images from separate breathing cycles inevitably causes uncertainties within the final images due to misalignment of independently acquired images. In this work we

developed a method to assess the spatial displacement uncertainties of an automated image based 4D-CT algorithm. The experiments were performed on live animals in order to provide *in-vivo* lung mechanics similar to a patient.

In addition to the two assumptions outlined and tested in this work, there is another implicit assumption made by all 4D-CT algorithms. This assumption is that the only movement during image acquisition is a direct result of respiration. In other words, there is no movement of the gross patient anatomy during the scan. This is considered a good assumption for the 4D-CT data acquisition due to the relatively short time required for image acquisition (~ 1 minute).

The assumption that the NCC coefficient calculated between two images is correlated with the respiratory induced spatial displacement between the images was modeled and tested. It was determined that the displacement between the reference and the matched image consists of two separate components, a random component as a result of limitations of the image acquisition and the nonlinear registration algorithm (σ_0) and a non-random component that resulted from mismatching the images (in this study the NCC uncertainty, σ_{NCC}). The NCC matching uncertainty was found to vary depending on the region of interest and section where the images were acquired. In general, from the inferior scan section to the superior scan section the NCC matching uncertainty trended to decrease the left lung ROI, but trended to increase in the chest wall ROI. The changes in these values are most likely due to the variations in amount of movement within these ROIs at different scan sections. The lung tends to have larger displacements in the inferior sections (lower), while the chest wall tends to have larger displacements in

the superior sections (upper). The values of the NCC matching uncertainty were relatively consistent across all scan sections within the entire anatomy ROI.

The 4D-CT algorithm relies on the use of successive NCC matches to produce continuous 3D volumes. We found in this paper that the NCC matching uncertainty will propagate through successive NCC matches and add in quadrature. This finding raises concern that the uncertainty due to NCC matching could become large if many subvolumes are required to cover the chest of a patient; a typical patient could require four to six 4.0 cm subvolumes. The number of successive NCC matchings required could be reduced by beginning the 4D data matching procedure in the middle of the volume and performing the matching in both the inferior and superior direction. This has the potential to reduce the number of successive NCC matches required by one half, thus reducing the total NCC uncertainty.

It was found that there was a random uncertainty governing the minimum measurable displacement between two images (σ_0). This uncertainty arises from the two most anatomically similar images not having exactly the same image intensity values for all image pixels. The nonlinear registration algorithm interprets a variation in pixel values as an anatomical misalignment between the two images and will produce the best estimate of the displacement required to realign the images. In reality, there are multiple reasons for variation in pixel intensities between the two images. The pixels will have a variation due to the intrinsic noise of the image, which may be on the order of 10 HU. Additionally, the finite pixel size and finite acquisition window (0.4 seconds and 0.625mm^3) will cause a blurring of stationary and moving structures respectively, which leads to variation in pixel intensity values. Finally, there may be an actual anatomical

misalignment between the anatomy imaged. This misalignment may be due images acquired at the same respiratory phase having small local variations in the location of anatomical structures due to breathing irregularities. The misalignment may also be due to an offset between the image acquisition window and the respiratory phase window of two images. All of these factors combine into the minimum measurable displacement by the nonlinear registration algorithm between the two most anatomically similar images and is represented by the random uncertainty parameter in the NCC uncertainty formula.

The assumption that all the images of an entire ciné scan subvolume move synchronously in phase was validated through the reference image invariance experiments. This assumption was validated for the three sections covering the entire thorax of the pig. In the special case where the overlapping reference image position was set at the most inferior or superior of the subvolume there were three instances where $\Delta\sigma_B(A,B)$ was significantly different from zero. However, when these displacements are compared to the values of minimum measurable uncertainty (σ_0) obtained from NCC matching experiments they were extremely small (0.77 - 0.93 mm for σ_0 compared to 0.02 mm for $\Delta\sigma_B(A,B)$). One limitation of the test is the available axial field of view (AFOV) to measure the displacements; the tests were limited to 3.0 cm of the 4.0 cm scan due to the inability of the nonlinear registration algorithm to perform at the extreme boundaries of a volume. While there were very few values significantly different from zero from the 3.0 cm AFOV experiments, it would be advantageous to be able to perform this test using a scanner with a larger AFOV to provide assurance that larger sections could be used with our 4D-CT algorithm.

The uncertainty analysis of our image based 4D-CT sorting algorithm was based upon the reference image invariance assumption that allows two subvolumes with as few as a single overlapping image location, to be matched in respiratory phase. If two images, one from each of two subvolumes to be matched, located at an overlapping image position are matched using NCC the displacement uncertainty between the two images (i.e. NCC displacement uncertainty; see section 4.2.1(i)) will also be equal to displacement uncertainty between the two matched subvolumes because the matched images and their associated subvolumes must maintain the same respiratory phase as required by the reference image invariance assumption. This argument could be extended to propagate the NCC displacement uncertainty over any number of subvolume matchings to generate a whole volume as long as the NCC matching uncertainty (σ_{NCC}) and the minimum displacement uncertainty (σ_{θ}) are known for each subvolume and the reference image invariance assumption is satisfied over the area covered by the subvolumes. For matching multiple subvolumes to build up a volume that is several times larger than the AFOV of the CT scanner, the NCC displacement uncertainties of each matching, which can be different for each subvolume, add in quadrature according to equation 4.3. Using the σ_{NCC} and σ_{θ} data shown in table 4-1 the displacement uncertainties of the 4D-CT volumes constructed from the lower, middle and upper sections can be calculated. For a volume that begins with the most inferior lower section, the most superior upper section will require the most NCC matching to select (2 matches: lower to middle, middle to upper) and the largest uncertainty in the whole assembled volume will occur in the upper section. The uncertainty values calculated for each ROI

in the upper section of the constructed whole volume of the pig's thorax were: 0.82 mm for the entire thorax, 1.03 mm for the left lung and 1.00 mm for the chest wall.

Pigs were used for these experiments because the velocity of respiratory motion and size of the structures within a pig are similar to those of a human patient. The average breathing rate and total lung tumour displacement of a human are approximately 12 bpm and 1.2 - 1.8 cm.²⁵ In our experiments, the pig's breathing rate was set to 20 breaths per minute, with a 1.0 - 1.2 cm displacement of the lower lung tissue. Therefore over the course of a breathing cycle, the velocity of the lung tumour/lung tissue in our pig experiments were equivalent to that in human patients (4.0 mm/sec). As well, the size of the pig's lung and range of displacements during breathing are similar to humans, allowing the use of a clinical CT scanner.

The uncertainty quantification technique presented in this study could be used to assess the uncertainties of other 4D-CT algorithms. Currently, methods using external markers as surrogates for respiratory motion are used in the most common 4D-CT methods. The uncertainties of these 4D-CT scans have yet to be quantified using an *in-vivo* model. In order to test an external marker method using the techniques developed in this chapter the anatomy of the animal would have to be scanned multiple times (at the same location) and then sorted using the data from the external marker. One volume would be selected as the reference volume and all nonlinear registration are calculated with respect to this volume. For each respiratory phase bin the average displacement with respect to the reference volumes can be calculated to assess the average uncertainties resulting from the assumption that a single external marker can be used to consistently predict the motion of the anatomy.

4.5 References

1. Ekberg, L., et al., *What margins should be added to the clinical target volume in radiotherapy treatment planning for lung cancer?* Radiother Oncol, 1998. **48**(1): p. 71-7.
2. Kubo, H.D. and B.C. Hill, *Respiration gated radiotherapy treatment: a technical study.* Phys Med Biol, 1996. **41**(1): p. 83-91.
3. Ozhasoglu, C. and M.J. Murphy, *Issues in respiratory motion compensation during external-beam radiotherapy.* Int J Radiat Oncol Biol Phys, 2002. **52**(5): p. 1389-99.
4. Hugo, G.D., D. Yan, and J. Liang, *Population and patient-specific target margins for 4D adaptive radiotherapy to account for intra- and inter-fraction variation in lung tumour position.* Phys Med Biol, 2007. **52**(1): p. 257-74.
5. Rietzel, E., et al., *Four-dimensional image-based treatment planning: Target volume segmentation and dose calculation in the presence of respiratory motion.* Int J Radiat Oncol Biol Phys, 2005. **61**(5): p. 1535-50.
6. Low, D.A., et al., *A method for the reconstruction of four-dimensional synchronized CT scans acquired during free breathing.* Med Phys, 2003. **30**(6): p. 1254-63.
7. Mageras, G.S., et al., *Measurement of lung tumor motion using respiration-correlated CT.* Int J Radiat Oncol Biol Phys, 2004. **60**(3): p. 933-41.
8. Pan, T., et al., *4D-CT imaging of a volume influenced by respiratory motion on multi-slice CT.* Med Phys, 2004. **31**(2): p. 333-40.
9. Vedam, S.S., et al., *Acquiring a four-dimensional computed tomography dataset using an external respiratory signal.* Phys Med Biol, 2003. **48**(1): p. 45-62.
10. Werner, R., et al., *Technical note: development of a tidal volume surrogate that replaces spirometry for physiological breathing monitoring in 4D CT.* Med Phys, 2010. **37**(2): p. 615-9.
11. Wink, N., C. Panknin, and T.D. Solberg, *Phase versus amplitude sorting of 4D-CT data.* J Appl Clin Med Phys, 2006. **7**(1): p. 77-85.
12. Gaede, S., et al., *The use of CT density changes at internal tissue interfaces to correlate internal organ motion with an external surrogate.* Phys Med Biol, 2009. **54**(2): p. 259-73.
13. Hunjan, S., et al., *Lack of correlation between external fiducial positions and internal tumor positions during breath-hold CT.* Int J Radiat Oncol Biol Phys, 2010. **76**(5): p. 1586-91.

14. Kanoulas, E., et al., *Derivation of the tumor position from external respiratory surrogates with periodical updating of the internal/external correlation*. Phys Med Biol, 2007. **52**(17): p. 5443-56.
15. Carnes, G., et al., *A fully automated non-external marker 4D-CT sorting algorithm using a serial cine scanning protocol*. Phys Med Biol, 2009. **54**(7): p. 2049-66.
16. Li, R., et al., *4D CT sorting based on patient internal anatomy*. Phys Med Biol, 2009. **54**(15): p. 4821-33.
17. Hope, A. *Applications of Manifold Learning Techniques in 4D-CT Reconstruction*. in ICCR 2007. 2007. Toronto, Ontario, Canada.
18. Fitzpatrick, M.J., et al., *A novel platform simulating irregular motion to enhance assessment of respiration-correlated radiation therapy procedures*. J Appl Clin Med Phys, 2005. **6**(1): p. 13-21.
19. Keall, P.J., et al., *Acquiring 4D thoracic CT scans using a multislice helical method*. Phys Med Biol, 2004. **49**(10): p. 2053-67.
20. Chang, J., T.S. Suh, and D.S. Lee, *Development of a deformable lung phantom for the evaluation of deformable registration*. J Appl Clin Med Phys, 2010. **11**(1): p. 3081.
21. Serban, M., et al., *A deformable phantom for 4D radiotherapy verification: design and image registration evaluation*. Med Phys, 2008. **35**(3): p. 1094-102.
22. Biederer, J., et al., *Respiratory-gated helical computed tomography of lung: reproducibility of small volumes in an ex vivo model*. Int J Radiat Oncol Biol Phys, 2007. **69**(5): p. 1642-9.
23. Bevington, P.R. and D.K. Robinson, *Data reduction and error analysis for the physical sciences*. 3rd ed. 2003, Boston: McGraw-Hill. xi, 320 p.
24. Pierce, G., Wang, K., Gaede, S., Battista, J., Lee, T-Y., *The effect of an inconsistent breathing amplitude on the relationship between an external marker and internal lung deformation in a porcine model*. Med Phys, 2010. **37**(11): p. 10.
25. Keall, P.J., et al., *The management of respiratory motion in radiation oncology report of AAPM Task Group 76*. Med Phys, 2006. **33**(10): p. 3874-900.

Chapter 5

Conclusion

5.1 Summary

The introduction of this thesis provided an overview of lung cancer and the different modalities available to treat this deadly disease. The issues regarding the effects of lung tumour motion on the imaging and radiation treatment of lung cancer were elucidated and the objectives of this thesis were outlined. The objectives of the thesis, to quantify the correlation between an external marker and the internal anatomy during respiration and then develop and validate a new 4D-CT method based purely on information contained within images of the internal anatomy were addressed in three chapters that followed the introduction.

In this final chapter, the major findings from the research will be summarized, followed by a discussion regarding the experimental techniques and clinical relevance of the results. The largest section of this chapter will encompass a discussion of areas for future investigation. The work presented in this thesis addresses fundamental scientific questions and assumptions that are sometimes overlooked when a method is so quickly implemented into a clinical setting, as was the case for 4D-CT. 4D-CT imaging and treatment is still relatively new and for it to reach its full potential there are key research and clinical topics to be addressed. This final thesis chapter will end with an overall summary of the major conclusions obtained from this work.

5.2 The relationship between external marker and internal anatomic lung displacement in a porcine model

The first experiment, presented in Chapter 2, investigated the relationship between the motion of a 1-dimensional external marker and the 3-dimensional internal anatomical motion of a pig's thorax under the influence of a variable breathing amplitude. Animal models are important when studying the effects of respiratory variations because they allow the effects to be studied over multiple breathing cycles, something that could not be done in human subjects due to the concern of delivering high radiation doses to patients from the CT imaging required. It was found that the average anatomical displacement (with respect to a reference volume) within a cylindrical region of interest drawn to include the lung tissue was significantly higher for images sorted using inconsistent breathing cycles than for images sorted using consistent breathing cycles (1.40 mm +/- 0.4 mm versus 1.29 mm +/- 0.3 mm, $p < 0.05$). Additionally, an inconsistent breathing amplitude was shown to change the slope of the regression line fit to the motion of the internal lung anatomy and the external marker motion in 10 of the 12 studies performed. From this work we concluded that an inconsistent breathing amplitude can invalidate the relationship between an external monitoring system and the internal anatomy.

5.3 The development of an automated image based 4D-CT sorting algorithm

In Chapter 2, it was shown that the correlation between an external respiratory surrogate marker and the internal anatomy was weakened by the inconsistency of the

amplitude of the respiratory cycle. In light of this finding and the occurrence of 4D-CT artifacts when using external marker sorting methods the choice was made to develop a new entirely image based 4D-CT algorithm. The method that was developed removed the use of any external respiratory surrogate to assign respiratory phase values to each acquired image. The image based algorithm produced contiguous time-matched 3D volumes using a normalized cross correlation (NCC) image matching procedure. The algorithm produced 3D volumes from asynchronously acquired time series of subvolumes that spanned the entire thorax. A subvolume was chosen from one time series and other subvolumes from the adjacent time series were matched to the first subvolume using the NCC image matching procedure. This process was continued in a 'daisy chain' like fashion to match subvolumes from every time series. Other ancillary algorithms were also developed to ensure that the final volumes spanned an entire breathing cycle and to minimize the number of imaging artifacts. To test the algorithm, 4D-CT scanning was performed on 5 patients with lung cancer. The 4D-CT volumes were constructed using three separate 4D-CT sorting methods based on: external marker phase, external marker amplitude and the new NCC method. In all 5 patients there were noticeably fewer imaging artifacts in the NCC 4D-CT volumes compared to the two commonly used external marker methods. Additionally, figure of merit values calculated at the interface between adjoining scan positions were significantly improved for the NCC 4D-CT volumes compared to the external marker methods.

In addition to the image based 4D-CT algorithm presented in this chapter there have been two other image based 4D-CT algorithms published. Both of these methods derive a relative breathing phase value for each image using only the information

contained within the image. *Li et al.*¹ published a method that uses four separate breathing metrics to derive a respiratory phase value for each image. The optimum combination of the four breathing metrics (and thus the respiratory phase value) is obtained by minimizing the difference in phase value between images acquired at the same time and within the same scan position. Images from separate scan positions that had the same respiratory phase were combined to form 3D volumes. While the combination of multiple metrics has the potential to be robust, the algorithm relies on the linear relationship between the respiratory phase values derived from independent scan positions; an assumption that requires validation, specifically in subjects that exhibit irregular breathing.

Additionally, *Hope et al.*² also developed an algorithm that assigns breathing phase values to individually acquired image using only the information contained within the image. In contrast to *Li et al.*, this algorithm produces a phase value relative to the images acquired at the independently acquired adjacent scan positions. The phase values from distant scan positions are included in the calculation of the relative phase values for each image by 'daisy chaining' the values through all the scan positions from the entire scanned volume. This method seems to do an excellent job of including the information from the entire final volume of interest for which 3D volumes will be reconstructed, however, there is not direct link between adjacent scan positions which may lead to phase shifts when the relative phase information is 'daisy chained'.

The image based algorithm that was developed in this thesis does not produce a respiratory state value but instead matches the anatomical features of volumes using a single simple image matching procedure. The algorithms is able to ensure continuity

between image matching by performing the image matching at an overlapping image position.

5.4 Applying an animal model to quantify the uncertainties of an image based 4D-CT algorithm

A fully automatic image based 4D-CT algorithm was developed in Chapter 3. In this chapter we developed a method to quantify the spatial displacement uncertainty of 4D-CT volumes generated with an image based 4D-CT sorting algorithm using an *in-vivo* animal model. We showed that NCC can be used for matching the respiratory phase of images and the uncertainty of the generated 4D-CT volumes consists of a random component independent of the sorting algorithm and a component from the NCC matching method employed in the sorting algorithm. In addition, the reference image invariance assumption that allows two subvolumes with as few as a single overlapping image location, to be matched in respiratory phase was validated. For matching multiple subvolumes to build up a volume that is several times larger than the AFOV of the CT scanner, the NCC displacement uncertainties of each matching, which can be different for each subvolume, add in quadrature, according to equation 4.3 of Chapter 4. The displacement uncertainties in the pig's lung were calculated to be approximately 1.0 mm in all regions of interest for the 4D-CT volumes constructed from three separate subvolumes. The assessment of the accuracy of spatio-temporal information of acquired 4D-CT volumes is essential for the delivery of radiation to the targeted volume with confidence.

5.5 Clinical Relevance

5.5.1 Relevance of a Porcine Model for Testing Lung Motions

The animal studies performed in this thesis were used to assess the accuracy of both an external marker tracking device and a 4D-CT imaging protocol. The pig lung was chosen for these experiments instead of inanimate mechanical phantoms because of its similarity to the human lung in both functionality and size.^{3,4} An *in-vivo* animal lung model is advantageous over a non-living phantom because the *in-vivo* model includes the visco-elastic properties of the lung that are likely to produce irregularities in the correlation between the external and internal motion. Pig models have been used to test lung motion and functionality in studies where using human subjects is not feasible because of radiation risk.⁵ The use of an animal model in our studies provided the freedom to perform our experiment over multiple consecutive breathing cycles, a luxury not available when using human subjects due to radiation dose concerns. With the growing use of respiratory gated radiotherapy to deliver higher "focused" radiation doses to patients, in an effort to control or cure cancer, it is important to understand the basic science behind the correlation of respiratory surrogate markers and internal anatomy. Animal models provide the best models for examining the highly complex lung motion and translating this knowledge to patients.

5.5.2 Clinical Relevance of Image Based 4D-CT method

Patients with lung cancer receive at least one 4D-CT scan as part of their normal treatment programs. These scans are performed using an external marker as respiratory surrogate to measure the respiratory phase at which the images were collected. As such, these methods are prone to imaging errors as a result of miscorrelation between the external marker respiratory surrogate and the patient's anatomy and are dependent on the positioning of the external marker. The image based 4D-CT algorithm presented in chapter 3 could be used in the treatment process of patients with lung cancer to replace the external marker 4D-CT algorithm to avoid artifacts in geometry and density. The artifact reduction provides a more accurate visualization of the tumour volume. Additionally, the new image based 4D-CT method is not dependent on the placement of an external marker and would provide day to day reproducibility of the 4D images, which is important if repeated 4D-CT scans are to be acquired for treatment planning and monitoring during a course of gated radiotherapy. Another important factor to consider is the cost of external marker respiratory surrogate systems. In cancer treatment centres that do not treat with respiratory gating, the investment of an external respiratory surrogate system is a large expense in order to obtain information about the tumour motion. The image based 4D-CT algorithm has been published in the public domain and thus could be available at a significantly reduced cost compared to an external marker system.

5.5.3 Limitations of the Image Based 4D-CT Algorithm

An image sorting algorithm has been developed to produce spatially coherent volume images from asynchronously acquired CT data. The 4D-CT algorithm produces these volumes by concatenating images from multiple scan locations that are acquired at

the same respiratory phase. Irregular breathing leads to variations of the maximum inspiration amplitude, maximum expiration amplitude and breathing cycle period resulting in a discrepancies in the extent of respiration induced motion among separate breathing cycles. To produce a spatially coherent 4D-CT dataset (i.e. combining images that all contain the same extent of respiratory motion) the images acquired during the irregular breathing portions of each cycle will be discarded. In our developed 4D-CT algorithm an upper and lower bound of respiratory amplitude are set by the breathing cycle that has the *least* amount of respiratory motion, images acquired outside of these bounds are not used in the generation of the final 4D-CT dataset. This trade-off, the image quality of the 4D-CT images even with irregular breathing amplitude versus loss of information about the true extent of the respiratory induced motion, is a limitation of our developed 4D-CT algorithm. It would be advantageous to use the images that are discarded during the 4D-CT sorting process to obtain valuable information about the variation of the extent of the breathing motion during irregular breathing. The knowledge of the tendency of a patient to breath irregularly during 4D-CT image acquisition could be incorporated into the treatment planning procedure through additional PTV margins to ensure that the tumour is consistently within the field of view of the radiation beam.

5.6 Future Considerations

Most current clinical CT scanners have a limited axial field of view in the range of 4.0 cm to 8.0 cm necessitating the use of 4D-CT algorithms to produced full volume images over the entire breathing cycle. However, recent technological developments have produced cone-beam CT scanners capable of imaging up to 16.0 cm (320 slices)

simultaneously in a single gantry rotation.⁶ Eventually these cone beam scanners will completely supplant the requirement for 4D-CT algorithms to produce volume images over the entire breathing cycle. However, there are some key limitations to cone-beam CT imaging because of which, 4D-CT algorithms will still be used for the foreseeable future.

Some cone beam CT scanners are mounted onto the gantries of radiation therapy linear accelerators and are used to geometrically align the treatment beam to the correct target. The volume images from these radiotherapy cone beam CT scanners have been shown to reduce patient set-up uncertainties during radiation treatment,⁷ but are currently not used to perform dose calculations. Due to the high flux of scattered photons reaching the CT detector⁸ and the long imaging acquisition times (~ 1 minute)⁹ the image quality of radiotherapy cone beam CT scanners is significantly lacking compared to conventional fan-beam CT scanners. The poor quality of these images has been shown to introduced an error of up to 3% when calculating doses in the lung, a clinical significant error.¹⁰ Until the image quality of radiotherapy cone beam CT is improved, conventional CT (and thus 4D-CT) will be required for acquiring accurate electron density data for dose calculations used in treatment planning.

Diagnostic cone beam CT scanners with much faster gantry rotation times (0.35 sec) have been developed. While these scanners have the ability to reduce the motion artifacts present in images of the thorax, the linear attenuation coefficients measured by these scanners have been shown to vary over the axial length of an object.⁶ The effect of these variations on treatment planning dose calculations has yet to be determined, but it is

clear that scatter will highly influence the image quality of cone beam CT images that use wider than a 8.0 cm axial field of view.

CT scanner technology is ever improving and eventually full volume images of an entire patient's chest during respiration will be acquired accurately without any post processing. However, this technology is not readily available and will be highly expensive when it does become available. With the current push towards higher doses and more conformity in radiation treatment planning of lung cancer, to improve local control and hence patient survival, 4D-CT algorithms used in conjunction with conventional fan-beam CT scanners will have a place in radiotherapy applications for the upcoming years.

5.7 Future Work

5.7.1 4D-CT Algorithm for Treatment Planning

The image based 4D-CT method was shown to minimize artifacts in the produced volume images better than the external marker method. A natural continuation of this work is to assess the clinical significance of the reduction of artifacts in the volume images generated by the image based 4D-CT method. This can be achieved by comparing radiation treatment plans calculated using volume images produced by the external marker (Varian Real-time Position Management device a.k.a. RPM) and the image based 4D-CT method. The comparison will include the effects of erroneous geometry and density artifacts and whether the patient's treatment would have been changed if volume images from the image based 4D-CT method are used instead of the

external marker 4D-CT method. One possible comparison will be to compare treatment plans based on volumes that are created by averaging volumes from both methods over the whole respiratory cycle. The use of average volumes is common practice when delivering non-gated radiotherapy. An example is shown in figure 5-1. Figure 5-1a shows a sagittal image from the average external marker (RPM) 4D-CT volume. The tumour has been outlined in green (GTV), margins in red have been added (PTV) and a six field intensity modulated radiation therapy (IMRT) plan to delivery 60 Gy to the PTV has been generated. The IMRT plan is acceptable as it delivers at least 95% of the dose to 95% of the PTV (57 Gy, yellow isodose line). Figure 5-1b show the dose-volume histograms (DVHs) for the GTV (green), PTV (red) and the lung minus the GTV (black). The GTV is then outlined on the average image based 4D-CT volume and a PTV is created by applying margins to the GTV. The planned beams generated on the average RPM 4D-CT volume are transposed to the average image based 4D-CT volume and the dose to the volume was recomputed. Figure 5-1c compares the results of the two plans; the external marker (RPM) PTV (red) and the image based (NCC) PTV (blue) do not overlap at some points. The constraint that 95% of the image based (NCC) PTV received at least 95% of the dose (57 Gy, yellow isodose line) is obviously not met by observing the overlap of this isodose line (yellow) and the NCC PTV (blue). The DVHs of both plans are shown in figure 5-1d where it is clear that the NCC PTV (blue) and the RPM PTV (red) do not completely overlap. Therefore, the tumour could have been underdosed if the treatment plan generated using the external marker 4D-CT that contained artifacts were delivered.

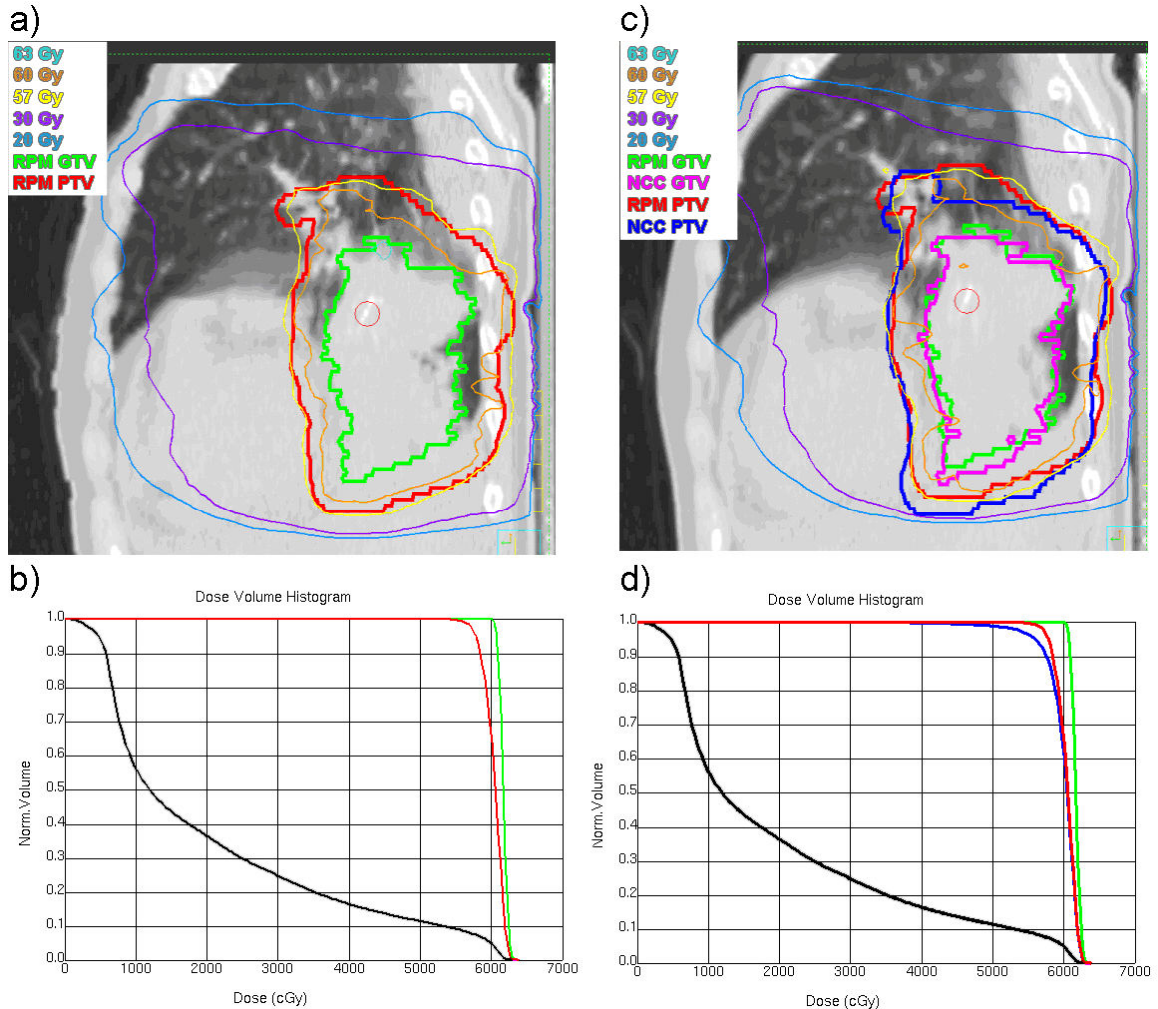


Figure 5-1: Comparison of treatment plans based on an averaged RPM 4D-CT volume and NCC 4D-CT volume. (a) Sagittal image of the averaged RPM 4D-CT volume with the tumour contoured in green (RPM GTV), margins in red added to the tumour GTV (RPM PTV) and the isodose lines from a 6-field IMRT plan. (b) the dose volume histograms (DVHs) of different volumes within the patient's lung. The red and green lines are the DVHs for the GTV and PTV respectively while the black line is the DVH for the entire lung minus the GTV. (c) Sagittal image of the averaged NCC 4D-CT volume. The 6-field IMRT treatment plan was recalculated with the averaged NCC 4D-CT volume and the isodose lines are plotted. The red (RPM PTV) and green (RPC GTV) lines are copied from (a) while the tumour in this image is outlined in purple (NCC GTV) and the margins added to the tumour are shown in blue (NCC PTV). (d) the DVHs of different volumes: NCC PTV (blue), RPM PTV (red), RPM GTV (green) and entire lung minus NCC GTV (black) computed from the recalculated 6-field IMRT treatment plan based on the averaged NCC 4D-CT volume.

This one example illustrates how the removal of artifacts from 4D-CT volumes can affect treatment plans. It is possible using the suggested study to show that it is important to reduce the artifacts in 4D-CT volumes that are used to calculate the dose distribution (and DVH) in a patient, even when delivering non-gated treatment in order to prevent underdosing of the tumor. In addition to using the average 4D-CT volume over the entire respiratory cycle, single individual phases of each 4D-CT could be tested in order to perform the experiment for gated radiotherapy.

5.7.2 Dose Reduction in 4D-CT

4D-CT is currently a high radiation dose imaging procedure, with doses (20 - 25 mSv)¹¹ approximately 2 to 5 times the dose of a regular chest CT examination.¹² Iterative image reconstruction shows promise to reduce the dose required while maintaining image quality.¹³ However, if adaptive gated radiotherapy is to be performed then multiple 4D-CT scans will have to be acquired over the course of the patient's treatment, which will still deliver a significant cumulated dose to non-targeted tissues. We see the potential for a further reduction of dose by combining our image based 4D-CT technique with two previously published dose-reduction methods for the heart¹⁴ and lungs.¹⁵ Our proposed method requires the acquisition of a full dose breath hold CT volume at middle inspiration and a low dose 4D-CT volumes dataset spanning an entire breath cycle. The regular dose breath hold volume is warped to each of the low dose 4D-CT volumes to create a regular dose 4D-CT volumes dataset from the breath-holding volume, with a potential dose saving of up to 80%. Figure 5-2 shows the promising results of implementing this dose reduction strategy on a single pig. In this study, a set of

regular dose 4D-CT images (RD 4D-CT) and a regular dose breath hold scan were acquired. Low dose images, at 1% of the regular dose (LD1 4D-CT) were obtained by adding noise to the regular dose 4D-CT images. The breath hold scan was warped to each of the LD1 4D-CT phases to produce a set of warped LD1 4D-CT ($\text{warp}(\text{BH})_{\text{LD1}}$ 4D-CT). This experiment allows the comparison between the RD 4D-CT volumes and the $\text{warp}(\text{BH})_{\text{LD1}}$. In this example, the results show good agreement between the original RD 4D-CT and the $\text{warp}(\text{BH})_{\text{LD1}}$, with a potential dose saving of 80%.

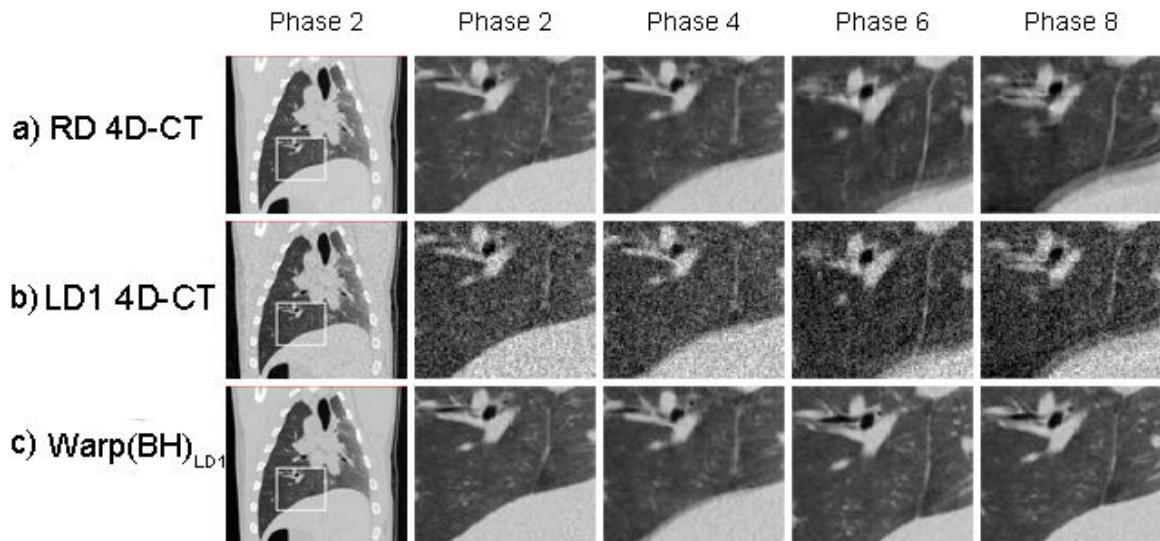


Figure 5-2: Shown are the coronal image of the a) RD 4D-CT, b) LD1 4D-CT and c) $\text{warp}(\text{BH})_{\text{LD1}}$ 4D-CT. The area outlined in the first column is expanded in the 2nd through 5th column to show the area over phases 2, 4, 6 and 8 of the breathing cycle. The $\text{warp}(\text{BH})_{\text{LD1}}$ 4D-CT is able to accurately reproduce the RD 4D-CT over the different breathing phases in spite of the extremely poor image quality of the LD1 4D-CT. Additionally, blurring artifacts present in the RD 4D-CT images are noticeably reduced.

5.7.3 Vendor-Supplied 4D-CT Comparison

There are various 4D-CT sorting algorithms provided by CT scanner vendors. There are currently no quantitative standards by which to judge the quality of the

resulting 4D-CT volumes produced from the different algorithms. The automated 4D-CT method described in this paper has the potential to become a reference method to which other 4D-CT methods can be compared. Through a series of comparisons a set of standards for image quality and 4D scanning parameters could be developed. This comparison would have to be done using a phantom (preferably a dynamic phantom with non-linear lung motion), to allow for control of the study parameters. From this study a consistent methodology could be developed to ensure that 4D-CT scans result in the best volume images at the lowest possible radiation dose.

5.7.4 Programmable Ventilator for Pig Model

The method of producing inconsistent breathing amplitudes in the pig model requires manually crimping the ventilator return gas tube at regular intervals. While this method was successful in creating an inconsistent breathing amplitude, the results obtained could vary from animal to animal depending on the operator. For future studies it would be useful to have a consistent method to induce inconsistent breathing amplitudes as it happens in patients' breathing patterns. This can be achieved using a ventilator with a programmable flow rate that is controlled by a patient's breathing pattern recorded with a spirometer.

5.7.5 Improved Image Matching Algorithm

The 4D-CT matching algorithm developed in this thesis performed well on a patient by patient basis. However, there are still aspects of the algorithm that could be

improved. The matching procedure currently uses all the pixels contained within an axial image to calculate the cross correlation value. However, as shown in Chapter 4, images that are *not* the most anatomically similar in the lung may be chosen because extraneous pixels, for example, those in the heart are included in the NCC calculation. Masking the image to exclude heart pixels or applying different weightings to different sections of the image could lead to improved image matching. Additionally, to further improve the speed of the image matching procedure it would be advantageous to implement the NCC calculation on a graphical processing unit (GPU). GPUs are specifically designed for a larger number of parallelized floating point calculations and would greatly improve the execution speed of the image matching algorithm.

5.8 Conclusions

The most significant findings of this thesis are summarized below.

- 1) The relationship between the motion of an external respiratory marker and the lung tissue of a pig is dependent on the consistency of the amplitude of breathing of the animal.
- 2) A 4D-CT sorting algorithm was developed that does not require an external surrogate marker. This algorithm improves image quality of the sorted volumes through the reduction of imaging artifacts in comparison to external marker based amplitude and phase sorting methods.
- 3) A method to quantify the displacement uncertainties of the image based 4D-CT sorting algorithm using an *in-vivo* pig model was developed. The uncertainties as a result of using normalized cross correlation to anatomically match images were shown to add in quadrature. It was shown that two sections (subvolumes) of the lung can be matched in respiratory phase by matching two images, one from each of the two subvolumes to be matched, at an overlapping image location.

The work in this thesis improves the image quality of 4D-CT volumes used for lung cancer diagnosis and radiotherapy planning. The direct benefit of this work will be to lung cancer patients who will be treated aggressively with radiation therapy to control their tumor. In addition to improving the image quality of 4D-CT volumes we have also quantified the spatial uncertainty associated with these images. This allows us to

establish the limitations of using 4D-CT volumes for radiation treatment planning and possibly this knowledge will result in the most optimal radiation treatment to the patient by minimizing the risk of missing the target (tumor) volume and/or over irradiation of the surrounding healthy tissues. It is the hope of this author that investigations of this nature will continue into the fundamental science and limitations of not just new 4D-CT sorting algorithms but the associated scanning protocols on new generation of CT scanners which have larger axial AFOV up to 16 cm and faster gantry rotation time down to 0.2 s such that continual improvements will positively influence the standard of care for lung cancer patients.

5.9 References

1. Li, R., et al., *4D CT sorting based on patient internal anatomy*. Physics in medicine and biology, 2009. **54**: p. 4821-33.
2. Hope, A. *Applications of Manifold Learning Techniques in 4D-CT Reconstruction*. in *ICCR 2007*. 2007. Toronto, Ontario, Canada.
3. Murata, K., et al., *Intralobular Distribution of Oleic Acid-Induced Pulmonary Edema in the Pig Evaluation by High-Resolution CT*. Investigative Radiology, 1989. **24**: p. 647.
4. Todo, G. and P.G. Herman, *High-resolution computed tomography of the pig lung*. Investigative Radiology, 1986. **21**: p. 689.
5. Mori, S., M. Endo, and H. Asakura, *Improvement in banding artefacts in four-dimensional computed tomography for radiotherapy planning*. Physics in medicine and biology, 2006. **51**: p. 5231-44.
6. Coolens, C., et al., *Implementation and characterization of a 320-slice volumetric CT scanner for simulation in radiation oncology*. Medical Physics, 2009. **36**: p. 5120.
7. Bissonnette, J.-P., et al., *Cone-beam computed tomographic image guidance for lung cancer radiation therapy*. International journal of radiation oncology, biology, physics, 2009. **73**: p. 927-34.
8. Siewerdsen, J.H. and D.a. Jaffray, *Cone-beam computed tomography with a flat-panel imager: Magnitude and effects of x-ray scatter*. Medical Physics, 2001. **28**: p. 220.
9. Jaffray, D.a., et al., *Flat-panel cone-beam computed tomography for image-guided radiation therapy*. International journal of radiation oncology, biology, physics, 2002. **53**: p. 1337-49.
10. Yang, Y., et al., *Evaluation of on-board kV cone beam CT (CBCT)-based dose calculation*. Physics in medicine and biology, 2007. **52**: p. 685-705.
11. Mori, S., et al., *Effective doses in four-dimensional computed tomography for lung radiotherapy planning*. Medical dosimetry : official journal of the American Association of Medical Dosimetrists, 2009. **34**: p. 87-90.
12. Shrimpton, P., M. Hillier, and M. Lewis, *Doses from computed tomography (CT) examinations in the UK—2003 review*. Chilton, NRPB- W, 2005.
13. Singh, S., et al., *Adaptive Statistical Iterative Reconstruction Technique for Radiation Dose Reduction in Chest CT: A Pilot Study*. Radiology, 2011.

14. Wierzbicki, M., et al., *Dose reduction for cardiac CT using a registration-based approach*. Medical Physics, 2007. **34**: p. 1884.
15. Li, T., et al., *Radiation dose reduction in four-dimensional computed tomography*. Medical Physics, 2005. **32**: p. 3650.

Appendix A

Uncertainty Analysis of NCC Formula for CT images

The normalized cross correlation (NCC) formula determines a correlation coefficient between two CT images. The image pixel values are assumed to be errorless and therefore the NCC coefficient also errorless. This is not the case, as there is statistical noise associated with each CT pixel. The uncertainty of the NCC formula is modeled using normal error propagation techniques and error values from a time series of images are calculated using the standard deviation of a region of interest, taken over a section of air in the CT image, and used as the uncertainty of the CT images.

Define the normalized cross correlation coefficient to be:

$$C = \frac{\sum_i M_i N_i}{\left(\sum_i M_i^2 \sum_j N_j^2 \right)^{1/2}}$$

where M and N are the two images to be matched indexed by the variable i .

Consider the top and bottom separately

TOP

$$T = \sum_i M_i N_i \tag{A.1}$$

$$\sigma_T = \sqrt{\sum \sigma_{M_i N_i}^2} \tag{A.2}$$

$$\sum \sigma_{M_i N_i}^2 = \sum N_i^2 \sigma_{M_i}^2 + \sum M_i^2 \sigma_{N_i}^2 \quad (\text{A.3})$$

sub (A.2) into (A.3) to obtain the error term for the Top

$$\sigma_T = \sqrt{\sum N_i^2 \sigma_{M_i}^2 + \sum M_i^2 \sigma_{N_i}^2} \quad (\text{A.4})$$

BOTTOM

$$B = \left(\sum M_i^2 \sum N_j^2 \right)^{1/2} \quad (\text{A.5})$$

For the individual terms

$$\sigma_{M_i^2} = 2M_i \sigma_{M_i}; \sigma_{N_i^2} = 2N_i \sigma_{N_i} \quad (\text{A.6})$$

With the sum

$$\sigma_{\sum M_i^2} = \left(\sum (2M_i \sigma_{M_i})^2 \right)^{1/2}; \sigma_{\sum N_i^2} = \left(\sum (2N_i \sigma_{N_i})^2 \right)^{1/2} \quad (\text{A.7})$$

The uncertainty of the product in (A.5)

$$\sigma_{\sum M_i^2 \sum N_i^2} = \left(\sum N_i^2 \sigma_{\sum M_i^2}^2 + \sum M_i^2 \sigma_{\sum N_i^2}^2 \right)^{1/2} \quad (\text{A.8})$$

sub (A.7) into (A.8)

$$\sigma_{\sum M_i^2 \sum N_i^2} = \left(\sum N_i^2 \sum (2M_i \sigma_{M_i})^2 + \sum M_i^2 \sum (2N_i \sigma_{N_i})^2 \right)^{1/2} \quad (\text{A.9})$$

Use the exponent uncertainty rule for (A.5)

$$\sigma_B = \frac{\frac{1}{2} \sigma_{\sum M_i^2 \sum N_i^2}}{\left(\sum M_i^2 \sum N_j^2 \right)^{1/2}} \quad (\text{A.10})$$

sub (A.9) into (A.10) to obtain the uncertainty for the Bottom

$$\sigma_B = \frac{\frac{1}{2} \left(\sum N_i^2 \sum (2M_i \sigma_{M_i})^2 + \sum M_i^2 \sum (2N_i \sigma_{N_i})^2 \right)^{\frac{1}{2}}}{\left(\sum M_i^2 \sum N_j^2 \right)^{\frac{1}{2}}} \quad (\text{A.11})$$

Now that we have the error terms for the Top and Bottom, consider the NCC function

$$NCC = \frac{T}{B} \quad (\text{A.12})$$

Uncertainty of NCC using quotient rule

$$\sigma_c = \frac{T}{B} \sqrt{\left(\frac{\sigma_T}{T} \right)^2 + \left(\frac{\sigma_B}{B} \right)^2} \quad (\text{A.13})$$

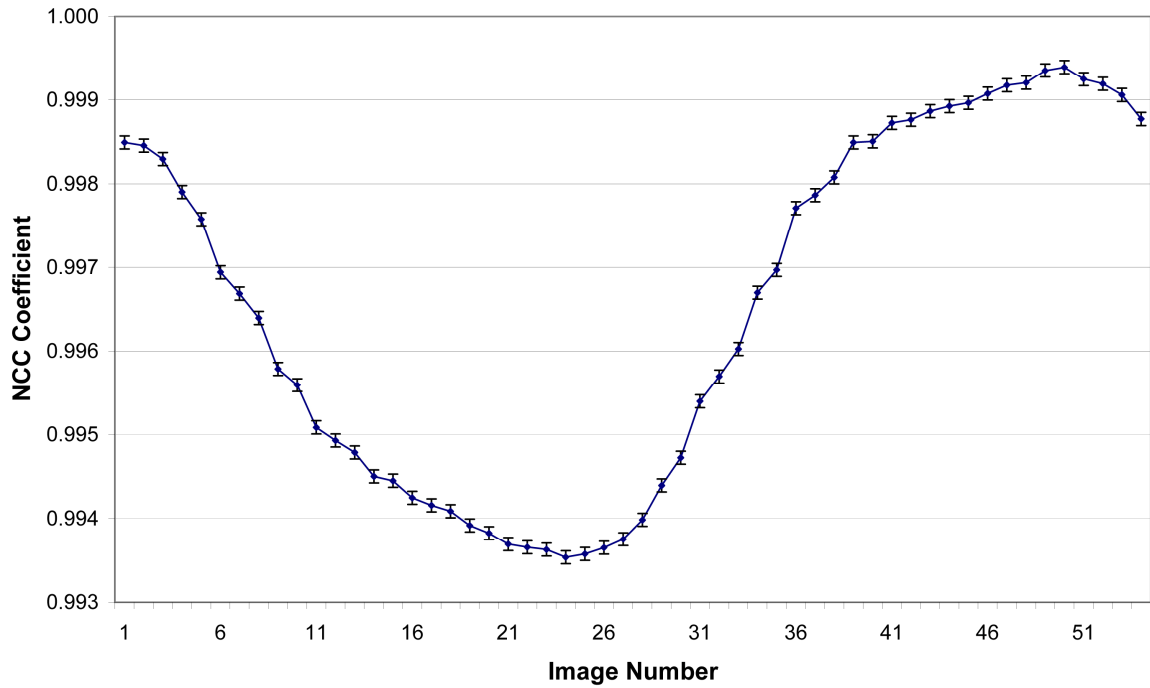
or

$$\sigma_c = \left(\frac{\sigma_T^2}{B^2} + \frac{\sigma_B^2 T^2}{B^4} \right)^{\frac{1}{2}} \quad (\text{A.14})$$

And values can be calculated using (A.1), (A.4), (A.5) and (A.11) and substituted into (A.14).

To examine this formula, a NCC matching between a single image and an entire time series of images is performed. The NCC coefficient between the single image and each image from the time series and the terms for the Top and Bottom are calculated. For each image, the error term is calculated from the standard deviation of a region of interest placed within the open air section of the image. A graph of the NCC curve with the σ_c values plotted as the error is shown below.

NCC Coefficient with Uncertainty



The error bars are approximately 1/3rd the distance between consecutive points. The uncertainty in the NCC calculation may lead to the mis-choice of an image that is most similar to the image being matched by 1 image position. The displacement uncertainty resulting from this mis-choice was explored in chapter 4 of this thesis and was found to be small. The salient feature of the graph are summarized in the table below. Cons Diff is the difference between consecutive NCC values.

Max of NCC Curve	0.999	σ_M	15.3 HU
Min of NCC Curve	0.993	σ_N	14.4 HU
$Mean_{NCC}$	0.996	$Mean_{\sigma_{NCC}}$	7.78E-05
$Max - Min$	0.006		
$Mean_{ABS(Cons Diff)}$	0.0002		
$\frac{\sigma_{NCC}}{Mean_{NCC}} \times 100$	0.008 %		
$\frac{\sigma_{NCC}}{Max - Min} \times 100$	1.328 %		
$\frac{\sigma_{NCC}}{Abs(Cons Diff)} \times 100$	36.213 %		

Appendix B

Transfer of Copywrite from *Physics in Medicine and Biology*



To: <permissions@iop.org>
 Cc:
 Bcc:
 Subject: Permission to use copywriten material
 From: Greg Pierce < > - Thursday 31/03/2011 22:18

Dear PMB,

I am currently writing my Ph.D. thesis and want to include a paper I published in Physics in Medicine and Biology as a chapter. I believe that I require permission from PMB in order to include the material. Could you point me in the direction in order to obtain the proper consent. The reference for the paper is below.

Many Thanks,
 Greg Pierce (ne Carnes)

✓ Carnes G, Gaede S, Yu E, Van Dyk J, Battista J, Lee TY. A fully automated non-external marker 4D-CT sorting algorithm using a serial cine scanning protocol. *Physics in Medicine and Biology* (2009); vol. 54 (7) pp. 2049-2066

PERMISSION TO REPRODUCE AS REQUESTED IS GIVEN PROVIDED THAT:

- ~~(a) the consent of the author(s) is obtained~~
- (b) the source of the material including author, title of article, title of journal, volume number, issue number (if relevant), page range (or first page if this is the only information available), date and publisher is acknowledged.
- (c) for material being published electronically, a link back to the original article should be provided (via DOI).

IOP Publishing Ltd
 Dirac House
 Temple Back
 BRISTOL
 BS1 6BE

Appendix C

Transfer of Copyright from *Medical Physics*

**American Association of Physicists in Medicine**

One Physics Ellipse
College Park, MD 20740-3846
(301) 209-3350
Fax (301) 209-0862
<http://www.aapm.org>

Office of the Executive Director

Angela R. Keyser
Phone: 301-209-3385 Fax: 301-209-0862
E-mail: akeyser@aapm.org

VIA EMAIL

April 5, 2011

Mr. Greg Pierce
Robarts Research Institute
Imaging
PO Box 5015
London, Ontario N6A 5K8
CANADA

Dear Mr. Pierce:

The American Association of Physicists in Medicine hereby grants permission to Greg Pierce to use the article indicated below as a chapter in his Ph.D thesis:

Greg Pierce, Kevin Wang, Stewart Gaede, Jerry Battista, and Ting-Yim Lee, "The effect of an inconsistent breathing amplitude on the relationship between an external marker and internal lung deformation in a porcine model." *Med. Phys.* 37(11) 5951-5960 (2010).

Sincerely,

Angela R. Keyser

Appendix D Animal Ethics Approval



01.01.11

***This is the 1st Renewal of this protocol**
*A Full Protocol submission will be required in **2014**

Dear Dr. **Lee**

Your Animal Use Protocol form entitled:

CT and PET Imaging of Normal Myocardium Cardiac Ischemia in Pigs

has had its yearly renewal approved by the Animal Use Subcommittee.

This approval is valid from **01.01.11 to 01.01.12**

The protocol number for this project remains as **2009-092**

1. This number must be indicated when ordering animals for this project.
2. Animals for other projects may not be ordered under this number.
3. If no number appears please contact this office when grant approval is received.
If the application for funding is not successful and you wish to proceed with the project, request that an internal scientific peer review be performed by the Animal Use Subcommittee office.
4. Purchases of animals other than through this system must be cleared through the ACVS office. Health certificates will be required.

REQUIREMENTS/COMMENTS

Please ensure that individual(s) performing procedures on live animals, as described in this protocol, are familiar with the contents of this document.

The holder of this *Animal Use Protocol* is responsible to ensure that all associated safety components (biosafety, radiation safety, general laboratory safety) comply with institutional safety standards and have received all necessary approvals. Please consult directly with your institutional safety officers.

c.c. J. Hadway, D. Forder

The University of Western Ontario
Animal Use Subcommittee / University Council on Animal Care
Health Sciences Centre, ● London, Ontario ● CANADA – N6A 5C1
PH: 519-661-2111 ext. 86770 ● FL 519-661-2028 ● www.uwo.ca / animal

Appendix E Human Ethics Approval



Office of Research Ethics

The University of Western Ontario
Room 00045 Dental Sciences Building, London, ON, Canada N6A 5C1
Telephone: (519) 661-3036 Fax: (519) 850-2466 Email: ethics@uwo.c
Website: www.uwo.ca/research/ethics

Use of Human Subjects - Ethics Approval Notice

Principal Investigator: Dr. T.Y. Lee
Review Number: 09960
Revision Number:
Protocol Title: Improving Lung Cancer Radiation Treatment with Four Dimensional Computed Tomography

Department and Institution: Diagnostic Radiology, Robarts Research Institute

Sponsor:

Approval Date: 17-Oct-03

End Date: 31-Aug-04

Documents Reviewed and Approved: UWO Protocol, Letter of Information & Consent Form

Documents Received for Information:

This is to notify you that the University of Western Ontario Research Ethics Board for Health Sciences Research Involving Human Subjects (HSREB) which is organized and operates according to the Tri-Council Policy Statement and the Health Canada/ICH Good Clinical Practice Practices: Consolidated Guidelines; and the applicable laws and regulations of Ontario has received and granted full board approval to the above named research study on the date noted above. The membership of this REB also complies with the membership requirements for REB's as defined in Division 5 of the Food and Drug Regulations.

This approval shall remain valid until end date noted above assuming timely and acceptable responses to the HSREB's periodic requests for surveillance and monitoring information. If you require an updated approval notice prior to that time you must request it using the UWO Updated Approval Request Form.

During the course of the research, no deviations from, or changes to, the protocol or consent form may be initiated without prior written approval from the HSREB except when necessary to eliminate immediate hazards to the subject or when the change(s) involve only logistical or administrative aspects of the study (e.g. change of monitor, telephone number). Expedited review of minor change(s) in ongoing studies will be considered. Subjects must receive a copy of the signed information/consent documentation.

Investigators must promptly also report to the HSREB:

- a) changes increasing the risk to the participant(s) and/or affecting significantly the conduct of the study;
- b) all adverse and unexpected experiences or events that are both serious and unexpected
- c) new information that may adversely affect the safety of the subjects or the conduct of the study

If these changes/adverse events require a change to the information/consent documentation, and/or recruitment advertisement, the newly revised information/consent documentation, and/or advertisement, must be submitted to this office for approval.

Members of the HSREB who are named as investigators in research studies, or declare a conflict of interest, do not participate in discussion related to, nor vote on, such studies when they are presented to the HSREB.

Chair of HSREB: Dr. Paul Harding

Janice Sutherland, M.A., Ethics Officer HSREB
E-mail: jsutherland@uwo.ca

Faxed Y N

Date: Oct 17/03

dh

This is an official document. Please retain the original in your files.



Office of Research Ethics

The University of Western Ontario
 Room 00045 Dental Sciences Building, London, ON, Canada N6A 5C1
 Telephone: (519) 661-3036 Fax: (519) 850-2466 Email: ethics@uwo.c
 Website: www.uwo.ca/research/ethics

Use of Human Subjects - Ethics Approval Notice

Principal Investigator: Dr. T.Y. Lee

Review Number: 09960

Revision Number: 1

Protocol Title: Improving Lung Cancer Radiation Treatment with Four Dimensional Computed Tomography

Department and Institution: Diagnostic Radiology, Robarts Research Institute

Sponsor:

Approval Date: 21-Sep-04

End Date: 31-Mar-05

Documents Reviewed and Approved: Revised Study End Date

Documents Received for Information:

This is to notify you that the University of Western Ontario Research Ethics Board for Health Sciences Research Involving Human Subjects (HSREB) which is organized and operates according to the Tri-Council Policy Statement and the Health Canada/CH Good Clinical Practice Practices: Consolidated Guidelines; and the applicable laws and regulations of Ontario has received and granted full board approval to the above named research study on the date noted above. The membership of this REB also complies with the membership requirements for REB's as defined in Division 5 of the Food and Drug Regulations.

This approval shall remain valid until end date noted above assuming timely and acceptable responses to the HSREB's periodic requests for surveillance and monitoring information. If you require an updated approval notice prior to that time you must request it using the UWO Updated Approval Request Form.

During the course of the research, no deviations from, or changes to, the protocol or consent form may be initiated without prior written approval from the HSREB except when necessary to eliminate immediate hazards to the subject or when the change(s) involve only logistical or administrative aspects of the study (e.g. change of monitor, telephone number). Expedited review of minor change(s) in ongoing studies will be considered. Subjects must receive a copy of the signed information/consent documentation.

Investigators must promptly also report to the HSREB:

- changes increasing the risk to the participant(s) and/or affecting significantly the conduct of the study;
- all adverse and unexpected experiences or events that are both serious and unexpected
- new information that may adversely affect the safety of the subjects or the conduct of the study

If these changes/adverse events require a change to the information/consent documentation, and/or recruitment advertisement, the newly revised information/consent documentation, and/or advertisement, must be submitted to this office for approval.

Members of the HSREB who are named as investigators in research studies, or declare a conflict of interest, do not participate in discussion related to, nor vote on, such studies when they are presented to the HSREB.

Chair of HSREB: Dr. Paul Harding

Janice Sutherland, M.A., Ethics Officer HSREB
 E-mail: jsutherl@uwo.ca

Faxed: IN
 Date: 21 Sep 04
 SK.

This is an official document. Please retain the original in your files.

Curriculum Vitae

Name: Greg Pierce (né Carnes)

Post-secondary Education and Degrees: Queen's University at Kingston
Kingston, Ontario, Canada
1997-2001 B.Sc. (Engineering)

The University of Western Ontario
London, Ontario, Canada
2004-2011 Ph.D.

Honours and Awards: Western Graduate Research Scholarship
University of Western Ontario
2005-2009

2nd Place, Oral Presentation
Western Research Forum
University of Western Ontario
2008

1st Place, Poster
Oncology Research Day
London Regional Cancer Program

Special University Scholarship
University of Western Ontario
2004

Academic All Canadian
Queen's University
1999-2001

Dean's Scholar
Queen's University
1998-2001

James H. Rattray Memorial Scholarship
Faculty of Engineering, Queen's University
2000

Robert Hall Memorial Award
Faculty of Engineering, Queen's University
1999

Dean's Award
Queen's University
1998

Queen's Entrance Scholarship
Queen's University
1997

Publications:

Naini, A, **Pierce G**, Lee TY, Patel R, Samani A. 'CT image construction of a totally deflated lung using deformable model extrapolation,' *Medical Physics* (2011); vol. 38 (2) pp. 872-883

Pierce G, Wang K, Gaede S, Battista J, Lee TY. 'The effect of an inconsistent breathing amplitude on the relationship between an external marker and internal lung deformation in a porcine model,' *Medical Physics* (2010); vol. 37 (11) pp. 5951-5960

Carnes G, Gaede S, Yu E, Van Dyk J, Battista J, Lee TY. A fully automated non-external marker 4D-CT sorting algorithm using a serial cine scanning protocol,' *Physics in medicine and biology* (2009); vol. 54 (7) pp. 2049-2066

Gaede S, **Carnes G**, Yu E, Van Dyk J, Battista J, Lee TY. 'The use of CT density changes at internal tissue interfaces to correlate internal organ motion with an external surrogate,' *Physics in Medicine and Biology* (2009); vol. 54 (2) pp. 259-73

Cook RA, **Carnes G**, Lee TY, Wells RG. 'Respiration-averaged CT for attenuation correction in canine cardiac PET/CT,' *Journal of Nuclear Medicine* (2007); vol. 48 (5) pp. 811-818

Wan S, Joshi CP, **Carnes G**, Schreiner LJ. 'Evaluation of an automated seed loader for seed calibration in prostate brachytherapy,' *Journal of applied clinical medical physics / American College of Medical Physics* (2006); vol. 7 (1) pp. 115-125